ARL-TR-94-23

Copy No. 23

Higher Order Spectral Investigations of Nonlinear Transverse Vibrations of Circular Rings

Technical Report under
ARL:UT Independent Research and Development Program and
Grant N00014-90-J-1366

Douglas J. Fox

Applied Research Laboratories
The University of Texas at Austin
P. O. Box 8029 Austin, TX 78713-8029

19 December 1994

Technical Report

Approved for public release;
distribution is unlimited.

Prepared for:
Applied Research Laboratories
Independent Research and Development Program

and

Office of Naval Research
Department of the Navy
Arlington, VA 22217-5000

DISCLAIMER NOTICE

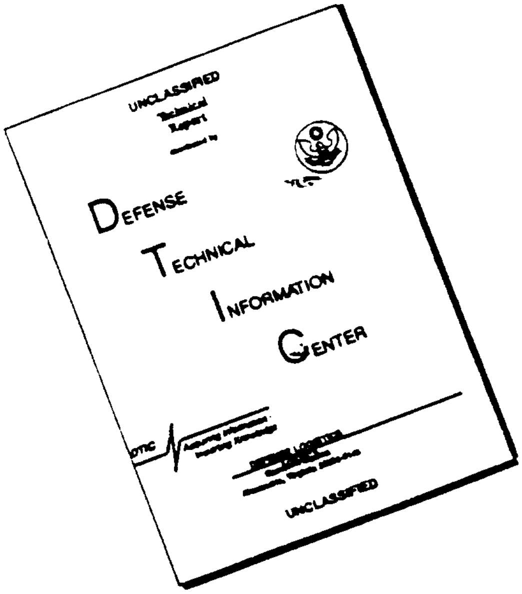

UNCLASSIFIED

Technical Report

DEFENSE

TECHNICAL

INFORMATION

CENTER

DTIC

UNCLASSIFIED

UNCLASSIFIED

REPORT DOCUMENTATION PAGE

Form Approved
OMB No. 0704-0188

Public reporting burden for this collection of information is estimated to average 1 hour per response, including the time for reviewing instructions, searching existing data sources, gathering and maintaining the data needed, and completing and reviewing the collection of information. Send comments regarding this burden estimate or any other aspect of this collection of information, including suggestions for reducing this burden, to Washington Headquarters Services, Directorate for Information Operations and Reports, 1215 Jefferson Davis Highway, Suite 1204, Arlington, VA 22202-4302, and to the Office of Management and Budget, Paperwork Reduction Project (0704-0188), Washington, DC 20503.

1. AGENCY USE ONLY (Leave blank)

2. REPORT DATE
19 Dec 94

3. REPORT TYPE AND DATES COVERED
technical

4. TITLE AND SUBTITLE
Higher Order Spectral Investigations of Nonlinear Transverse Vibrations of Circular Rings, Technical Report under Applied Research Laboratories Independent Research and Development Program and Grant N00014-90-J-1366.

5. FUNDING NUMBERS
ARL:UT IR&D Program
N00014-90-J-1366

6. AUTHOR(S)
Fox, Douglas J.

7. PERFORMING ORGANIZATION NAMES(S) AND ADDRESS(ES)
Applied Research Laboratories
The University of Texas at Austin
P.O. Box 8029
Austin, Texas 78713-8029

8. PERFORMING ORGANIZATION REPORT NUMBER
ARL-TR-94-23

9. SPONSORING/MONITORING AGENCY NAME(S) AND ADDRESS(ES)
Applied Research Laboratories
The University of Texas at Austin
P.O. Box 8029
Austin, Texas 78713-8029

Office of Naval Research
Department of the Navy
Arlington, VA 22217-5000

10. SPONSORING/MONITORING AGENCY REPORT NUMBER

11. SUPPLEMENTARY NOTES

12a. DISTRIBUTION/AVAILABILITY STATEMENT
Approved for public release; distribution is unlimited.

12b. DISTRIBUTION CODE

13. ABSTRACT (Maximum 200 words)
(see reverse side)

14. SUBJECT TERMS
(see reverse side)

15. NUMBER OF PAGES
127

16. PRICE CODE

17. SECURITY CLASSIFICATION OF REPORT	**18. SECURITY CLASSIFICATION OF THIS PAGE**	**19. SECURITY CLASSIFICATION OF ABSTRACT**	**20. LIMITATION OF ABSTRACT**
UNCLASSIFIED	UNCLASSIFIED	UNCLASSIFIED	SAR

NSN 7540-01-280-5500

DTIC QUALITY INSPECTED 1

UNCLASSIFIED

Standard Form 298 (Rev. 2-89)
Prescribed by ANSI Std. 239-18
298-102

13. The transverse (radial) vibrations of geometrically thin circular rings are experimentally and analytically investigated in order to further understand the order and degree of nonlinearities present. Two important mechanisms have been identified that contribute to the quadratic elements of the nonlinear equations of motion. The first results from the first order nonlinear strain-displacement relations interacting with the effect of circumferential periodicity present in a complete ring which gives rise to a double frequency breathing mode. The second mechanism is due to the geometric imperfections present in any manufactured structure which can give rise to a double frequency flexural mode response. These and other nonlinear mechanisms that generate multiple wavenumber responses and interactions among these wavenumbers have been identified. The Galerkin's procedure was used to analytically determine the differential equations of motion. An experimental study has also been conducted on three rings of various thickness to radius ratios. The experimental results question the existence of the nonlinear breathing mode response but confirm, at least qualitatively, the geometric imperfection flexural mode response. The investigation of these nonlinear structural vibrations is enhanced by the use of higher order spectral signal processing, such as bicoherency, which preserves phase information and allows the investigation of frequency interactions and can indicate the presence of nonlinear system effects.

14. bicoherence
bispectrum
breathing mode response
circular rings
circular ring vibrations
Donnell-Mushtari shallow shell equations
Galerkin's method
geometric imperfections
Hamilton's principle
higher order spectra
inextensional assumption
inextensional vibrations
nonlinear vibrations
polyspectra
quadratic response
Sander's shell equations

TABLE OF CONTENTS

TABLE OF CONTENTS (CONCLUDED)

LIST OF FIGURES

LIST OF FIGURES (CONCLUDED)

LIST OF TABLES

This page intentionally left blank.

LIST OF SYMBOLS

Section 1

*	complex conjugate operation
j	$\sqrt{-1}$
x(t), y(t)	finite length valued series
x(n), y(n)	discrete, uniformly sampled values series
X(f), Y(f)	Fourier transform of x(t), y(t)
$X(f_i)$, $Y(f_i)$	discrete Fourier transform of x(n), y(n)
T	length of series
N	number of points in series
f, f_i	frequency (Hz)
ω, ω_i	circular frequency (rad/s)
f_s	sampling frequency
f_N	Nyquist frequency ($= f_s / 2$)
E[ ]	expected value function
$S_x\ (f_i)$	power spectrum of signal x(t) at frequency f_i
$B_{xx}\ (f_i, f_j)$	bispectrum of signal x(t) at frequency combination f_i, f_j, f_i+f_j
$b_{xx}^2(f_1,f_2)$	bicoherence of signal x(t) at frequency combination f_1, f_2, f_1+f_2

Section 2

x, y, z	axial, circumferential, radial geometric coordinates
u', v', w'	axial, circumferential, radial general displacements
u, v, w	axial, circumferential, radial mid-plane displacements
$\dot{w}$, $\ddot{w}$	time derivatives $\left(\dot{w}=\frac{\partial w}{\partial t}\right)$, $\left(\ddot{w}=\frac{\partial^2 w}{\partial t^2}\right)$
$\bar{w}$	geometric imperfection static radial displacement
t	time
n, m	circumferential wavenumbers

N_x, N_y, N_{xy}	force stress resultants
M_x, M_y, M_{xy}	moment stress resultants
R	shell, ring nominal (to mid-plane) radius
h	shell, ring thickness
$q(y,t)$	applied radial load per unit area
E	Young's modulus
ν	Poisson's ratio
ρ	mass volume density
σ_{yy}	element stress
ε_{yy}	element strain

$$\left.\begin{aligned} \alpha_1 &= \frac{\partial v}{\partial y} + \frac{w}{R} \\ \alpha_2 &= R\frac{\partial^2 w}{\partial y^2} + \frac{\partial v}{\partial y} \\ \alpha_3 &= \frac{1}{2}\left(\frac{\partial w}{\partial y}\right)^2 + \frac{\partial w}{\partial y}\frac{\partial \bar{w}}{\partial y} \end{aligned}\right\} \text{strain energy parameters}$$

$z' = \frac{z}{R}$	nondimensional thickness integration parameter
$k = \frac{h^2}{12R^2}$	thickness parameter
V, T, W_{nc}	strain energy, kinetic energy, and nonconservative forces applied to Hamilton's principle
$\delta V, \delta T, \delta W_{nc}$	variational expressions of V, T, and W_{nc}
$A_n(t), B_n(t)$	dynamic amplitude functions for displacement response
δ_n	amplitude of the nth component of the geometric imperfection
ϕ_n	spatial phase angle of the nth component of the imperfection
ω	driving frequency
$\omega_0 = \sqrt{\frac{E}{\rho R^2}}$	natural frequency of breathing mode

$\delta^k(y_o)$	Dirac delta function: input driving force at single point, y_o
$\tilde{A}_m$	$\frac{A_m}{h}$, nondimensional amplitude
$\tilde{\delta}_m$	$\frac{\delta_m}{h}$, nondimensional imperfection amplitude
τ	ω_o t, nondimensional time

This page intentionally left blank.

PREFACE

This material was originally published in May 1993 as a thesis, in partial fulfillment of the requirements for the degree of Master of Science in Engineering, The University of Texas at Austin.

This page intentionally left blank.

SECTION 1
INTRODUCTION TO RINGS AND HIGHER ORDER SPECTRA

1.1 THE CHOICE TO STUDY CIRCULAR RINGS

In order to fully understand the purpose of this thesis, a brief history of the interest and motivation of this study of circular ring vibrations is useful. This research was generated as part of the Structural Acoustics Program of the Signal Physics Group at Applied Research Laboratories, The University of Texas at Austin. This interest in structural vibrations is primarily motivated from the need to understand the radiated noise fields of marine structures. The motivating factors for the investigation of circular rings are threefold.

First, circular rings are significant structural members of marine platforms serving as stiffeners for the cylindrical shell hull. It is well known that the discontinuities in the cylindrical shells created by the ring stiffeners act as local radiation sources to the sound field (Ref. 1, pp. 349-369). Ring stiffeners attenuate the wave energy of the cylindrical shell by transferring it to vibration energy in the stiffeners. This can be a very efficient radiation source, especially at coincidence or trace-matching velocities of the vibration waves (Ref. 1, pp. 406-414). Thus, it is important to understand the vibration characteristics of the ring stiffeners.

Second, the study of circular rings can aid in the investigation of cylindrical shells in that many interesting and significant vibration features of cylindrical shells are present in circular rings. Evensen, for example, used shallow shell equations to investigate circular ring vibrations (Ref. 2). The present work on rings, indeed, has a historical basis in the thesis by O'Donnell on active control of internal sound radiation of cylindrical shells (Ref. 3). Many features that will be investigated in this paper for circular rings should also be present in the vibrations of cylindrical shells.

Third, transverse vibrations of circular rings can be fully described using a single circumferential coordinate. Thus, the complicating effects of axial and circumferential wave interactions present in shells is eliminated, yet, as stated previously, many of the interesting features of shell vibration are retained. Also, part of this work includes the investigation of geometric imperfection effects. These imperfections can be easily and accurately measured since they are approximately one dimensional. The single spatial coordinate also simplifies the experimental investigation, and thus the experimentally obtained response signatures can be more readily identified.

The investigation of the *nonlinear* vibrations of circular rings is also motivated by the interest in marine structure sound radiation. As the active control of linear mechanisms in marine structures progresses, additional second order sources of radiated noise which are generated in a nonlinear manner may become more significant. These nonlinear sources can be significant for three reasons: (1) their relative contribution to the total radiated noise field may be larger simply because the linear sources are reduced; (2) the active control of linear mechanisms can, in fact, increase the presence of nonlinear sources; and (3) recent advances in higher order spectral signal processing have improved the ability to identify the nonlinear sources.

Thus, the importance of the investigation of nonlinear vibrations of circular rings is established. Much progress has been made in the literature on the investigation of nonlinear ring vibrations. The following section will describe some of this previous work and the unique contribution that this thesis makes to this subject.

1.2 PREVIOUS WORK ON NONLINEAR VIBRATIONS OF CIRCULAR RINGS

An excellent introduction to the nonlinear vibration of circular cylindrical shells, which is related to the study of circular rings, was written by David Evensen and includes the progress of the field until 1972 (Ref. 4). This article briefly describes the early work of Reissner, who used the shallow shell equation approach (Ref. 4, p. 134, and Ref. 5). Reissner's work, however, could not be applied to a complete shell because of the type of assumed solution he used (Ref. 4, p. 136). This problem will be discussed in more detail during the development of the ring equations of motion for this paper.

Chu [Ref. 6] furthered the work on shells by allowing for the application of Reissner's work to the complete shell. His analysis, however, predicted a hardening type of nonlinear behavior for the natural frequencies of vibration (Ref. 4, p. 137, and Ref. 6). This did not correctly predict the type of stiffening as Evensen experimentally observed a nonlinear softening behavior. This discrepancy between the experimental and analytic results led Evensen to the discovery that Chu's (and indeed Reissner's) approximate solution would not satisfy the continuity condition in the circumferential displacement of a complete shell (Ref. 4, p. 138).

Wanting to further understand the nonlinear vibration problem of cylindrical shells, especially in light of the question of continuity as applied to the type of assumed mode solution admitted, Evensen turned his attention to the circular ring. This work was performed by Evensen at the California Institute of Technology in the mid 1960's (Ref. 2), and is probably the most influential work on the nonlinear transverse vibrations of circular rings. Since his work was motivated by his investigations of cylindrical shells, the equations of motion used as the basis of his analysis are shallow shell equations of motion reduced to describe the ring. This approach, which was introduced by Reissner, is extremely useful and will be used to some extent in this report. Many of the interesting features of nonlinear ring vibrations can be described using these equations as even a cursory reading of Evensen's work will reveal.

Evensen, however, did not investigate the influence of geometric imperfections on the nonlinear ring vibrations. This problem was addressed analytically by Liu and Arbocz who investigated the geometrically imperfect cylindrical shell along with the effects of circumferential and longitudinal stiffeners in a series of reports (Refs. 7-10). They did not, however, include an experimental analysis. The absence of experimental evidence of the influence of geometric imperfections on the nonlinear vibrations of shells of revolution was a motivating factor in the generation of this study.

There exists much literature on the subject of circular ring vibrations based on linear theory. Many of these papers are directed towards the prediction of the ring natural frequencies of vibration (Refs. 11-19). The last three references pertain to the problems of radially loaded vibrating rings. These papers address such issues as the comparison of extensional and inextensional forms of vibration and the effects of rotational inertia and tangential shear on the ring vibrational frequencies. Some of their discussions are pertinent to the present work and will be referred to when appropriate in the text.

The analysis of nonlinear vibrations of circular rings has been addressed by a number of authors as well (Refs. 2, 4, 20-24). References 20 and 21 are papers by Evensen that contain parts of his Doctoral Thesis (Ref. 2). Kovrigin and Potapov (Ref. 22) addressed the idea of degenerate mode cases where the bending motion becomes unstable and tangential traveling flexural waves are generated. Maganty and Bickford (Ref. 23) addressed large amplitude vibrations and include an analysis of the coupling between the radial and axial out-of-plane flexural motions. Mack and Yew (Ref. 24) use a formulation for the nonlinear equations of motion which follows the

Goodier and McIvor (Ref. 25). (As pointed out by Mack and Yew, Goodier and McIvor actually address the ring problem despite the title of their paper.) Mack and Yew present to second order the solution of the equations of motion using a perturbation technique. Of interest in their paper is the identification of critical thicknesses for which the solution form breaks down. Aspects of these papers that contribute to the particular problems that the present work addresses will be noted.

1.3 AN INTRODUCTION TO HIGHER ORDER SPECTRA

Spectral signal processing has become an indispensable tool for the modern structural experimentalist almost since the development of fast Fourier transform (FFT) techniques. Most spectral analysis, however, has been limited to the use of the power spectrum. Increasingly, though, higher order spectral analysis has developed into an extremely useful tool for the identification and analysis of non-Gaussian and nonlinear signals. Higher order spectral processing has demonstrated the ability to (1) recover phase information from non-Gaussian response signals, (2) determine whether aliasing has resulted from undersampling, (3) detect transient signals, (4) characterize the nature of the nonlinearity in systems, and (5) recover signal information that is masked by Gaussian noise. This section will serve as a brief introduction to higher order spectra (HOS), particularly the bispectrum and bicoherence,† and include a brief bibliography on HOS applied to mechanical systems.

The bicoherence (usually referred to as the bispectrum by authors) has had a number of applications in the past 30 years. In their review (Ref. 26, p. 871), Nikias and Raghuveer list a few of these: oceanography, geophysics, biomedicine, speech processing, plasma physics, and fluid mechanics. Papers have also been published on the application of HOS to mechanical vibration systems. Included in this are systems involving chaotic motion (Ref. 27), laser Doppler vibration measurement (Ref. 28), nonlinear mode interactions in a parametrically excited beam (Ref. 29), aeroelastic phenomenon (Refs. 30-32), nonlinear resonators, human body vibration, and loudspeakers (Ref. 33), drill bit incipient fault detection (Ref. 34), and the previously mentioned work on cylindrical

---

† The terminology for HOS has not been standardized. The most useful proposal is for the -spectrums to refer to the unnormalized cumulant spectrums. The normalized cumulant spectrums are then labeled -coherences. Thus, the bispectrum is unnormalized while the bicoherence is normalized. Many authors use bispectrum and bicoherence interchangeably; however, this text will use bicoherence strictly for the normalized cumulant spectrum.

shells (Ref. 3). These demonstrate the applicability of HOS to the analysis of nonlinear and parametric mechanical systems.

Mathematically, HOS can be introduced in terms of the Fourier transform of nth order cumulants. However, this author finds it simpler to define HOS within the frequency domain. Excellent introductions to HOS, especially the bispectrum, can be found in Refs. 3, 26, and 35-36.

To understand HOS, it is helpful to review the development and properties of the power spectrum. Given a finite length valued series x(t), the complex finite Fourier transform is defined as

$$X(f) = \int_0^T x(t)\, e^{-j2\pi ft}\, dt \quad , \tag{1.3.1}$$

where $j = \sqrt{-1}$, f is the frequency, and T is the length of the series. In experimental signal processing, x(t) is usually a discrete, uniformly sampled signal written as $x(n) = x\left(\frac{i\,T}{N}\right) = x\left(\frac{i}{f_s}\right)$, where N is the number of sampled points in the series and f_s is the sampling frequency. Thus the Fourier transform will be a discrete Fourier transform:

$$X\,(f_i) = \frac{1}{N} \sum_{n=0}^{N-1} x(n)\, e^{-j2\pi in/N} \quad , \quad (i = 0, 1, \ldots, N-1) \quad , \tag{1.3.2}$$

which is practically calculated using an FFT algorithm.

The power spectrum is approximated as

$$S_x\,(f_i) \approx E\left[X(f_i)\, X^*(f_i)\right] \quad , \tag{1.3.3}$$

where E[ ] is the expected value function taken over a collection of records and the asterisk (*) is the complex conjugate operation. In practice, the expected value represents an ensemble average of sections of data called blocks. Note that the power spectrum is a magnitude function and that all phase information is suppressed. If x(n) is a real function, then S_x (f) is a real, even function. Thus typically the function is folded about the zero frequency and displayed using only the positive frequencies.

The bispectrum is approximated as

$$B_{xx}(f_i, f_j) \approx E\left[X(f_i)\, X(f_j)\, X^*(f_i+f_j)\right] \quad . \tag{1.3.4}$$

If the valued series x(n) is real, the principal domain of the bispectrum can be determined from the symmetry properties

$$B_{xx}(f_1, f_2) = B_{xx}(f_2, f_1) \tag{1.3.5a}$$

$$B_{xx}(f_1, f_2) = B_{xx}^*(-f_1, -f_2) \tag{1.3.5b}$$

$$B_{xx}(f_1, f_2) = B_{xx}^*(-f_2, -f_1) \tag{1.3.5c}$$

$$B_{xx}(f_1, -f_2) = B_{xx}^*(f_1 - f_2, f_2) \quad . \tag{1.3.5d}$$

With proper sampling technique, additional practical limitations exist on the region over which the bispectrum must be estimated. It is required that $f_1 \leq f_N$, $f_2 \leq f_N$, and $f_1 + f_2 \leq f_N$ where f_N is the Nyquist frequency equal to one-half the sampling frequency, f_s (i.e., $f_N = \frac{1}{2} f_s$). Figure 1.3.1 indicates the principal region (also called the support set) for the bispectrum. Note that there is an additional (non-shaded) triangular region included in this figure. This triangular region, which is limited by two additional symmetries not included in Eqs. 1.3.5, is sometimes labeled the outer triangle or forbidden triangle. The discretely sampled bispectrum can be expected to have non-zero values in this region only if (1) the continuous time process is not band limited or the sample rate is insufficient such that aliasing occurs or (2) the time series is nonstationary (Ref. 36, p. 9, and Ref. 37). The software used in this paper calculates and plots the outer triangle even though neither of the above situations should occur if indeed the signals are stationary and the low-pass (anti-aliasing) filters are properly implemented.

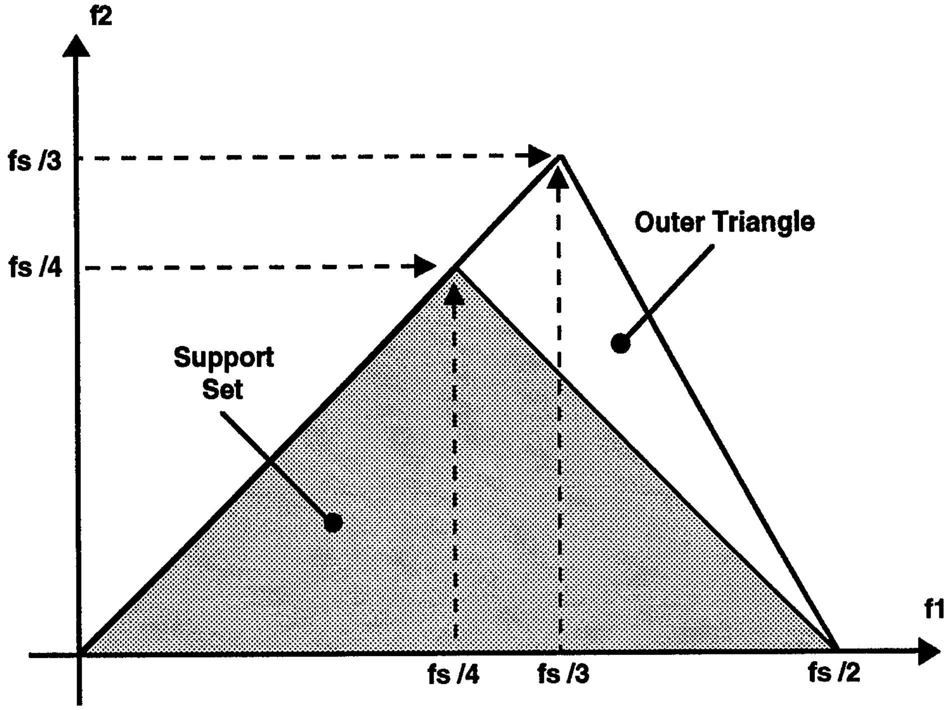

Figure 1.3.1
Principal Domain and Outer Triangle of Bispectrum

AS-94-1143

As stated previously, the bispectrum can be used to analyze nonlinear systems. Figure 1.3.2 indicates part of the basis for this claim. In this figure, the input to the various systems, X_k, is a deterministic signal composed of M discrete oscillating components of frequency ω_m, amplitude a_m, and phase ϕ_m. If this signal passes through a linear system, the result will be an output signal, Y_k, composed of the same frequencies ω_m but modified in amplitude to b_m and phase shifted to θ_m. These frequency components are present (though maybe not detectable due to noise masking) in the power spectrum, which indicates the presence of energy at the ω_m frequency. If the same input signal passes through a quadratic system, the coupled frequencies $\omega_m \pm \omega_n$ will be present in the output signal Y_2 with a phase of $\theta_m \pm \theta_n$. Since in almost all cases a quadratic system will exist in conjunction with a linear co-system, the output of the coupled linear-quadratic system will contain the frequency components ω_m, ω_n, and $\omega_m \pm \omega_n$, which will be phase related by θ_m, θ_n, and $\theta_m \pm \theta_n$ and thus will exhibit a non-zero bispectrum. A similar result will be present using the trispectrum and a coupled linear-cubic system and so on through the higher orders. Note that the coupled quadratic-linear system will be null for the trispectrum and indeed for all higher spectrum. Similarly, the coupled cubic-linear

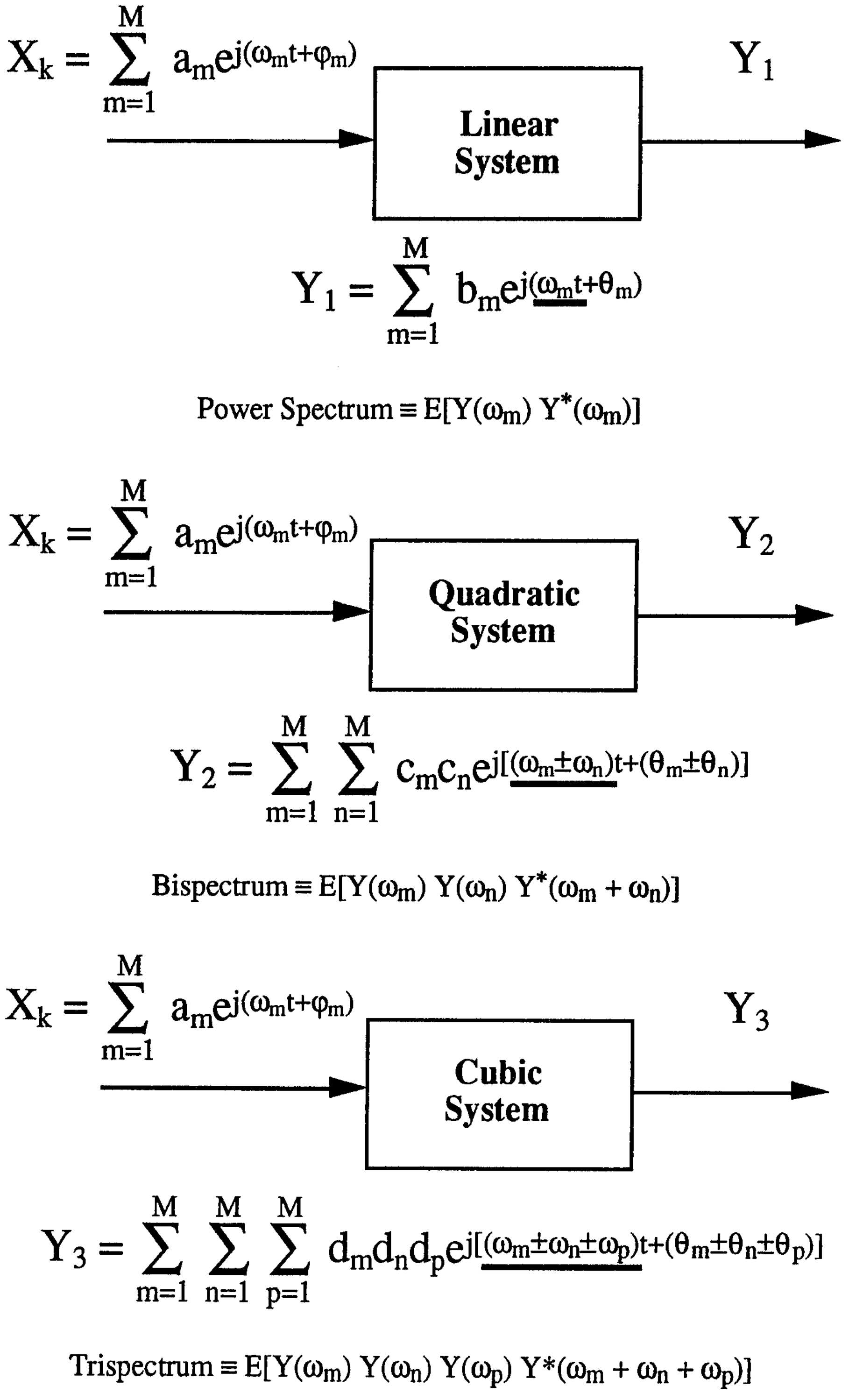

$$X_k = \sum_{m=1}^{M} a_m e^{j(\omega_m t+\varphi_m)}$$

$$Y_1 = \sum_{m=1}^{M} b_m e^{j(\underline{\omega_m t}+\theta_m)}$$

Power Spectrum $\equiv E[Y(\omega_m)\, Y^*(\omega_m)]$

$$X_k = \sum_{m=1}^{M} a_m e^{j(\omega_m t+\varphi_m)}$$

$$Y_2 = \sum_{m=1}^{M} \sum_{n=1}^{M} c_m c_n e^{j[\underline{(\omega_m\pm\omega_n)}t+(\theta_m\pm\theta_n)]}$$

Bispectrum $\equiv E[Y(\omega_m)\, Y(\omega_n)\, Y^*(\omega_m + \omega_n)]$

$$X_k = \sum_{m=1}^{M} a_m e^{j(\omega_m t+\varphi_m)}$$

$$Y_3 = \sum_{m=1}^{M} \sum_{n=1}^{M} \sum_{p=1}^{M} d_m d_n d_p e^{j[\underline{(\omega_m\pm\omega_n\pm\omega_p)}t+(\theta_m\pm\theta_n\pm\theta_p)]}$$

Trispectrum $\equiv E[Y(\omega_m)\, Y(\omega_n)\, Y(\omega_p)\, Y^*(\omega_m + \omega_n + \omega_p)]$

Fig 1.3.2: System Identification through Higher Order Spectra Analysis

AS-94-1144

system will display a null bispectrum and null higher spectrums 4th order or above. Thus, a non-zero bispectrum can indicate the presence of a quadratic nonlinearity in a system; the trispectrum can indicate the presence of a cubic nonlinearity in a system, and so on.

The bispectrum can be normalized to produce a bicoherence for which asymptotic statistics can be easily calculated. Normalizing removes the effects of amplitude dependence so that the nonlinear nature of systems can be identified, theoretically, regardless of the amplitude of the signal inputted to the system. There exist two common ways to normalize the bispectrum (Ref. 3, pp. 25-26, and Ref. 38). The Kim and Powers normalization defines the bicoherence as

$$b_{xx}^2(f_1,f_2) = \frac{|B_{xx}(f_1,f_2)|^2}{E\big[|X(f_1)\,X(f_2)|^2\big]\,E\big[|X(f_1+f_2)|^2\big]} \quad , \tag{1.3.6}$$

while the Haubrich normalization defines the bicoherence as

$$b_{xx}^2(f_1,f_2) = \frac{|B_{xx}(f_1,f_2)|^2}{E\big[|X(f_1)|^2\big]\,E\big[|X(f_2)|^2\big]\,E\big[|X(f_1+f_2)|^2\big]} \quad . \tag{1.3.7}$$

Notice that the normalizing denominator of the Haubrich bicoherence (Eq. 1.3.7) is the product of the power spectrums at the frequencies f_1, f_2, and f_1+f_2.

For narrow band signals, the choice of the normalization does not significantly affect the bicoherence estimates as demonstrated by Elgar and Guza (Ref. 38). Both the Kim and Powers and the Haubrich normalizations produce consistent estimates bounded by $0 \leq b_{xx}^2(f_1,f_2) \leq 1$ as long as the number of records averaged is greater than 16 for the Haubrich bicoherence. On the basis of asymptotic theory and numerical simulations, the significance levels for zero bicoherence versus the statistical degrees of freedom (dof_s) were determined to be independent of the type of normalization used (Ref. 38, p. 1668). The degrees of freedom is equal to twice the number of records averaged. In this work, the Haubrich bicoherence will be used.

In using HOS, it has been previously stated that one of their advantages is that they are able to detect nonlinear interactions masked by Gaussian noise. This valuable asset of HOS is due to the property that ideally all HOS are zero for Gaussian noise. For finite length (i.e., practical) signals this nulling of Gaussian noise is true only in the asymptotic limit. The significance levels for zero Bicoherence for linear, random phase processes (which produce ideally zero HOS) have been calculated by Elgar and Guza as a function of degree of freedom (Table 1.3.1). Thus, a 95 percent significance level for zero Bicoherence is given by the expression $\sqrt{6.0/\mathrm{dof_s}}$ (Ref. 38, p. 1668). As an example, a signal separated into 50 records would have a 95 percent certainty of the presence of a significant Bicoherence for all points with $b_{xx}^2(f_1,f_2) > 0.24$, recalling that $b_{xx}^2(f_1,f_2) \le 1$.

Table 1.3.1
Theoretical Significance Levels for Zero Bicoherence

Zero Bicoherence Percent	Theoretical Significant Levels
99 %	$\sqrt{9.2/\mathrm{dof_s}}$
95 %	$\sqrt{6.0/\mathrm{dof_s}}$
90 %	$\sqrt{4.6/\mathrm{dof_s}}$
80 %	$\sqrt{3.2/\mathrm{dof_s}}$

To summarize, significant levels of Bicoherence for a signal will be achieved if:

i) Signal components exist at the frequencies f_1, f_2, and f_1+f_2,

ii) A phase coherence exists between the frequencies f_1, f_2, and f_1+f_2, and

iii) The Gaussian noise level exists below a certain signal-to-noise ratio such that the zero Bicoherence levels of Table 1.3.1 are surpassed.

Thus, the lack of a phase coherence (or locking) between existing frequency components of a signal or too low a signal-to-noise ratio for the number of records available to average will result in a practical null Bicoherence. It should be noted that since this is a statistical process, the existence of a significant level of $b_{xx}^2(f_1,f_2)$ does not necessarily mean that a nonlinear or parametric system is present since it is statistically possible for spurious peaks to appear. Thus, as with all analysis tools, the Bicoherence cannot be used without some knowledge of the tool or the system being analyzed.

The following sections are dedicated to the analysis of nonlinear ring vibrations, both analytically and experimentally. Some background for this work has been presented in this section. Specifically, the motivation for the study of rings from a naval architecture point of view and from previous work on rings and shells has been presented. Additionally, the HOS tools that will be helpful in understanding the nonlinearities of the transverse vibrations have been introduced. Section 2 is devoted to the analysis of ring vibrations. Section 3 describes experimental research performed on the subject. Section 4 presents some discussions and conclusions concerning this paper's contributions to nonlinear ring vibrations as well as areas where future study would be helpful.

This page intentionally left blank.

SECTION 2

ANALYSIS OF NONLINEAR RING VIBRATIONS

This section will be devoted to the analysis of the nonlinear equations of motion for the transverse vibration of circular rings. Following Evensen (Ref. 2), the equations of motion will be developed in subsection 2.1 using the shallow shell equations reduced to describe thin ring vibrations. In subsection 2.2, the nonlinear equations of motion will be developed using an energy approach (Hamilton's principle) for a twofold purpose: (1) the assumptions used in deriving the equations are clearly seen, and (2) a comparison with the shallow shell equation approach can be made.

Once the partial differential equations of motion have been developed, the remaining part of this chapter will be used to analyze their nonlinear features. Subsection 2.3 will be devoted to the reduction of the partial differential equations of motion to ordinary differential equations of motion using a method of weighted residuals (Galerkin's procedure). Subsection 2.4 will analyze the results from the Galerkin's procedure and discuss some of the important effects, such as the evidence of a nonlinearly generated breathing mode and the effects of geometric imperfections.

2.1 NONLINEAR SHELL EQUATIONS AND THE CIRCULAR RING

One approach for the derivation of the equations of motion for circular rings is the reduction of the shallow shell equations developed for the circular cylindrical shell. This approach is the same as that used by Evensen in most of his work (Ref. 2). One form of the nonlinear cylindrical shell equations, called the Donnell-Mushtari equations, can be written as (Ref. 39)

$$\frac{\partial N_x}{\partial x} + \frac{\partial N_{xy}}{\partial y} = \rho h \ddot{u} \qquad (2.1.1a)$$

$$\frac{\partial N_{xy}}{\partial x} + \frac{\partial N_y}{\partial y} = \rho h \ddot{v} \qquad (2.1.1b)$$

$$\frac{\partial^2 M_x}{\partial x^2} + 2\frac{\partial^2 M_{xy}}{\partial x \partial y} + \frac{\partial^2 M_y}{\partial y^2} + \frac{\partial}{\partial x}\left(N_x \frac{\partial w}{\partial x} + N_{xy}\frac{\partial w}{\partial y}\right)$$

$$+ \frac{\partial}{\partial y}\left(N_y \frac{\partial w}{\partial y} + N_{xy}\frac{\partial w}{\partial x}\right) - \frac{N_y}{R} + q(x,y,t) = \rho h \ddot{w} \quad , \qquad (2.1.1c)$$

where u,v, and w are the axial, tangential, and radial displacements, respectively; x, y, and z are the independent axial, tangential, and radial spatial components, respectively; t is the dimensional time; the double dots above the displacements represent the second derivatives with respect to time; R is the nominal radius of the shell; $M_{\text{subscripts}}$ are the various components of the moment resultants; $N_{\text{subscripts}}$ are the various components of the force resultants; and q(x,y,t) is the forcing pressure function, which is assumed to act only in the radial direction. See Fig. 2.1.1 for a description of the coordinate system. The assumptions that transverse shear stresses are neglected in the force equilibrium Eqs. 2.1.1a and 2.1.1b (Ref. 39, p. 23) and that only the first order terms of the Taylor's series approximations of the moment and stress resultants are implied. Other assumptions may be added depending upon the development of the expressions for the stress and moment resultants.

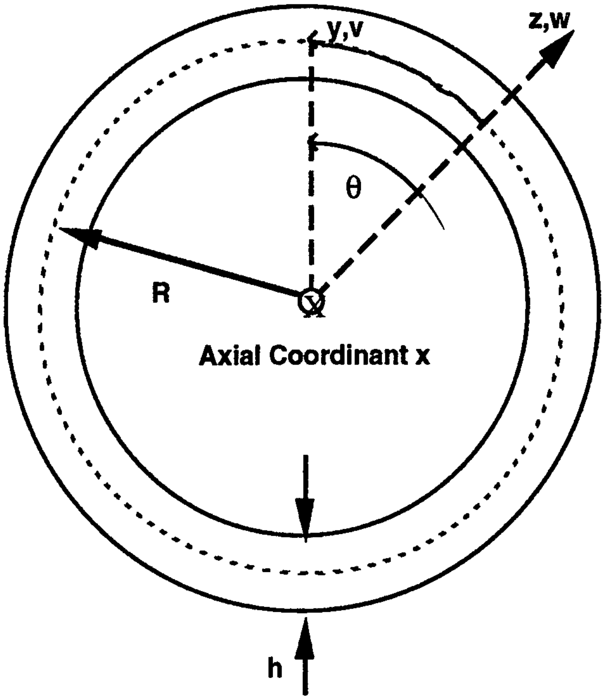

Figure 2.1.1
Ring Coordinate System

The following assumptions are made to specialize Eqs. 2.1.1a–c to the case of the circular ring (Ref. 2):

- The force-resultants N_x and N_{xy} are assumed to be zero throughout the ring. This is justified since the axial boundary conditions require N_x and N_{xy} to vanish at the axial limits of the ring and there is assumed to be no rapid variations in the x-direction for transverse vibrations.

- The displacements u, v, w; the moment resultants M_x, M_{xy}, M_y; and the force resultants N_x, N_{xy}, N_y are taken to be functions of the circumferential coordinate y and time, t, only. Thus, all derivatives with respect to x are considered equal to zero.

- The transverse load is also assumed to be a function of y and t only. Thus, $q(x,y,t) = q(y,t)$.

With these assumptions, the shallow shell equations reduce to the following for a circular ring:

$$\rho h\ddot{u} = 0 \tag{2.1.2a}$$

$$\frac{\partial N_y}{\partial y} = \rho h\ddot{v} \tag{2.1.2b}$$

$$\frac{\partial^2 M_y}{\partial y^2} + \frac{\partial}{\partial y}\left(N_y \frac{\partial w}{\partial y}\right) - \frac{N_y}{R} + q(y,t) = \rho h\ddot{w} \quad . \tag{2.1.2c}$$

The first of these equations indicates that, as expected due to the assumptions used, the axial inertia and membrane loads are zero for purely transverse vibrations, and motion in the axial direction can be neglected. This first equation will be, henceforth, dropped from consideration.

The force and moment resultants, N_y and M_y, are defined by the integrals

$$N_y = \int_{-h/2}^{h/2} \sigma_{yy}\left(1 + \frac{z}{R}\right)dz \approx \int_{-h/2}^{h/2} \sigma_{yy}\, dz \tag{2.1.3a}$$

$$M_y = \int_{-h/2}^{h/2} \sigma_{yy}\left(1+\frac{z}{R}\right)z\,dz \approx \int_{-h/2}^{h/2} \sigma_{yy}\; z\,dz \quad . \tag{2.1.3b}$$

As similar to the derivation of the strain-displacement relations in Appendix A, the ring is considered thin, i.e., $\frac{z}{R} << 1$. This leads to the approximations of Eqs. 2.1.3a-b.

The nonlinearities investigated in this paper are geometrical in nature and are not material. Thus, Hooke's Law is used to relate stresses to strains:

$$\sigma_{yy} = \frac{E}{1-\upsilon^2}\left[\varepsilon_{yy} + \upsilon\,\varepsilon_{xx}\right] \approx E\,\varepsilon_{yy} \quad , \tag{2.1.4}$$

where the plane stress assumptions have been applied, $\upsilon^2 << 1$ and the displacement and stress gradients in the axial direction are negligible.

The nonlinear strain-displacement relations for ε_{yy} derived for cylindrical coordinates are referenced in Novozhilov (Ref. 40, p. 192). In Appendix A, ε_{yy} is examined in some detail with initially strain-free geometric imperfections included. The result of Appendix A is a similar order strain-displacement relation as that of Liu and Arbocz (Ref. 10, p. 10) since it retains all the essential features of the nonlinearities addressed by Evensen and the effects of geometric imperfections. The strain-displacement relation is repeated from Appendix A (Eq. A.10):

$$\varepsilon_{yy} = \frac{\partial v}{\partial y} + \frac{w}{R} - z\left(\frac{\partial^2 w}{\partial y^2} - \frac{1}{R}\frac{\partial v}{\partial y}\right) + \frac{1}{2}\left(\frac{\partial w}{\partial y}\right)^2 + \frac{\partial w}{\partial y}\frac{\partial \bar{w}}{\partial y} \; . \tag{2.1.5}$$

A note about the geometric imperfections is appropriate here. In writing the imperfection shape as $\bar{w}$, the imperfection shape is assumed to be adequately expressed in terms of its midplane imperfection shape (see Fig. 2.1.2). Thus there are implicit assumptions that there are no variations in the imperfection shape through the thickness (z-direction) and across the axial width (x-direction) of the ring. For thin rings, this would seem to be a reasonable assumption.

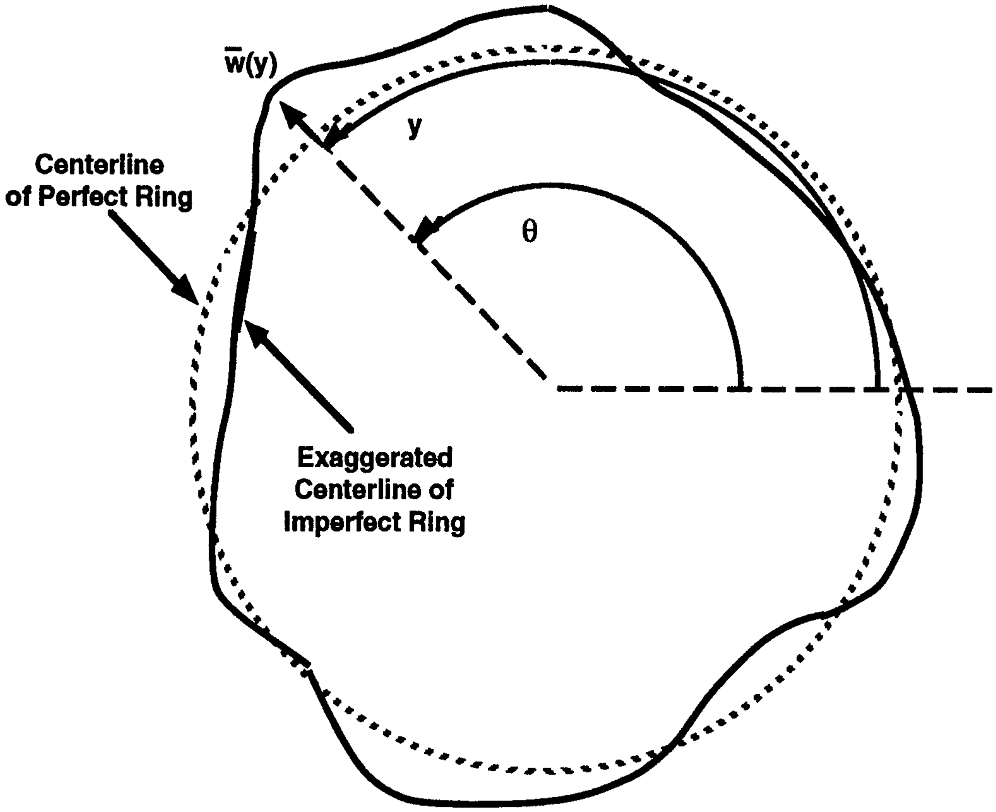

Figure 2.1.2
Geometric Imperfection Coordinate System

AS-94-1146

By integrating Eqs. 2.1.3a–b using Hooke's Law (Eq. 2.1.4) and the strain displacement relations (Eq. 2.1.5), the stress resultants in terms of displacements are obtained:

$$N_y = Eh\left[\frac{\partial v}{\partial y} + \frac{w}{R} + \frac{1}{2}\left(\frac{\partial w}{\partial y}\right)^2 + \frac{\partial w}{\partial y}\frac{\partial \bar{w}}{\partial y}\right] \tag{2.1.6a}$$

$$M_y = -\frac{Eh^3}{12}\left[\frac{\partial^2 w}{\partial y^2} - \frac{1}{R}\frac{\partial v}{\partial y}\right] \quad . \tag{2.1.6b}$$

Note that the leading coefficient is lacking the $(1-\upsilon^2)$ factor that is present in the full shell equations. This is due to the assumption of no axial stress σ_{xx} for the ring that is not appropriate for the shell.

These relations can be substituted into the shallow shell equations (Eq. 2.1.2) to obtain the equations of motion completely in terms of the displacements v and w:

$$Eh\frac{\partial}{\partial y}\left[\frac{\partial v}{\partial y}+\frac{w}{R}+\frac{1}{2}\left(\frac{\partial w}{\partial y}\right)^2+\frac{\partial w}{\partial y}\frac{\partial \bar{w}}{\partial y}\right]=\rho h\ddot{v} \tag{2.1.7a}$$

$$\begin{aligned}&\frac{Eh^3}{12}\left[\frac{\partial^4 w}{\partial y^4}-\underline{\frac{1}{R}\frac{\partial^3 v}{\partial y^3}}\right]-Eh\frac{\partial}{\partial y}\left\{\left[\frac{\partial v}{\partial y}+\frac{w}{R}+\frac{1}{2}\left(\frac{\partial w}{\partial y}\right)^2+\frac{\partial w}{\partial y}\frac{\partial \bar{w}}{\partial y}\right]\frac{\partial w}{\partial y}\right\}\\&+\frac{Eh}{R}\left[\frac{\partial v}{\partial y}+\frac{w}{R}+\frac{1}{2}\left(\frac{\partial w}{\partial y}\right)^2+\frac{\partial w}{\partial y}\frac{\partial \bar{w}}{\partial y}\right]+\rho h\ddot{w}=q(y,t)\quad .\end{aligned} \tag{2.1.7b}$$

These equations, though not exactly the Donnell-Mushtari equations due to the underlined term in Eq. 2.1.7b, may not be accurate for low circumferential wavenumbers (see comparison tables in Ref. 39, pp. 41-42). If the approximation that $\frac{z}{R} << 1$ is not applied to the definitions of the strain-displacement relation (Eq. 2.1.5), it is possible to improve the accuracy of the equations of motion. This operation is known as the Sanders' correction of the Donnell-Mushtari equations (Ref. 41, p. 72, and Ref. 39, p. 34). Markus goes so far as to "term the Sanders' equations as *the best first-order equations describing the deformations of cylindrical shells* " [italics his] (Ref. 41, p. 96). These equations are stated below but with the inclusion of the nonlinear and geometric imperfection terms as in Eqs. 2.1.7.

$$Eh\frac{\partial}{\partial y}\left[\frac{\partial v}{\partial y}+\frac{w}{R}+\frac{1}{2}\left(\frac{\partial w}{\partial y}\right)^2+\frac{\partial w}{\partial y}\frac{\partial \bar{w}}{\partial y}+\underline{\frac{h^2}{12R^2}\left(\frac{\partial v}{\partial y}-R\frac{\partial^2 w}{\partial y^2}\right)}\right]=\rho h\ddot{v} \tag{2.1.8a}$$

$$\begin{aligned}&\frac{Eh^3}{12}\left(\frac{\partial^4 w}{\partial y^4}-\frac{1}{R}\frac{\partial^3 v}{\partial y^3}\right)-Eh\frac{\partial}{\partial y}\left\{\left[\frac{\partial v}{\partial y}+\frac{w}{R}+\frac{1}{2}\left(\frac{\partial w}{\partial y}\right)^2+\frac{\partial w}{\partial y}\frac{\partial \bar{w}}{\partial y}+\right.\right.\\&\left.\left.\underline{\frac{h^2}{12R^2}\left(\frac{\partial v}{\partial y}-R\frac{\partial^2 w}{\partial y^2}\right)}\right]\frac{\partial w}{\partial y}\right\}+\frac{Eh}{R}\left[\frac{\partial v}{\partial y}+\frac{w}{R}+\frac{1}{2}\left(\frac{\partial w}{\partial y}\right)^2+\right.\\&\left.\frac{\partial w}{\partial y}\frac{\partial \bar{w}}{\partial y}+\underline{\frac{h^2}{12R^2}\left(\frac{\partial v}{\partial y}-R\frac{\partial^2 w}{\partial y^2}\right)}\right]+\rho h\ddot{w}=q(y,t)\quad .\end{aligned} \tag{2.1.8b}$$

The underlined terms are the additions to the Donnell-Mushtari equations due to the Sanders' improvement. Also, the Sanders' improvement and the Donnell-Mushtari equations are generally stated without the nonlinear and geometric imperfection terms.

The boundary conditions on w and v are obtained from the requirement of continuity through the ring for the free ring vibration problem. These are periodic in nature:

$$w(0,t) = w(2\pi R,t) \qquad \frac{\partial w}{\partial y}(0,t) = \frac{\partial w}{\partial y}(2\pi R,t) \tag{2.1.9a-b}$$

$$\frac{\partial^2 w}{\partial y^2}(0,t) = \frac{\partial^2 w}{\partial y^2}(2\pi R,t) \qquad \frac{\partial^3 w}{\partial y^3}(0,t) = \frac{\partial^3 w}{\partial y^3}(2\pi R,t) \tag{2.1.9c-d}$$

and

$$v(0,t) = v(2\pi R,t) \qquad \frac{\partial v}{\partial y}(0,t) = \frac{\partial v}{\partial y}(2\pi R,t) \quad . \tag{2.1.10a-b}$$

With the nonlinear equations of motion (Eqs. 2.1.8) and the boundary conditions (Eqs. 2.1.9–10), the boundary value problem for the transverse vibrations of complete thin circular rings is defined. The equations of motion have been derived in this section using the shallow shell approach. This is similar to the approach of Evensen except that we have selected the Sanders' modification to the Donnell-Mushtari shallow equations rather than the Morley improvement. Sanders' approach involves keeping terms that are neglected in the Donnell-Mushtari equations. Specifically the integrals of the force and stress resultants are not simplified by the thin ring assumptions. Morley's approach uses order of magnitude arguments to simplify the complicated Flügge's equations (Ref. 42). In the present analysis, nonlinear terms have been retained and geometric imperfections have been included as suggested by Liu and Arbocz.

2.2 NONLINEAR RING EQUATIONS DERIVED FROM AN ENERGY APPROACH

This subsection will be devoted to the derivation of the nonlinear differential equations of motion for the thin circular ring using the energy approach method. The energy approach more clearly indicates the various assumptions used in derivation of the equations. Appendix A of Evensen's dissertation (Ref. 2, pp. 133-142) is followed except that geometric imperfections are included and the strain-displacement relation is that used in the shallow shell equation approach of subsection 2.1 (Eq. 2.1.5). First the expressions for strain energy, kinetic energy, and virtual work are derived. Then the calculus of variations is used to obtain the necessary variations of these expressions for the application of Hamilton's principle.

2.2.1 *Hamilton's Principle*

Hamilton's principle may be stated as (Ref. 43, p. 198–202)

$$\int_{t_1}^{t_2} \left[\delta(T - V) + \delta W_{nc}\right] dt \quad , \tag{2.2.1}$$

where T is the kinetic energy of the system, V is the strain energy of the system, and W_{nc} is the work of the nonconservative forces (including applied forces and damping), and t_1 and t_2 are the times at which the configuration of the system is specified. The variational calculus is used to determine the variations of T, V, and W_{nc} (denoted by δ) with respect to the spatial coordinates. The first step in the energy approach then is to determine the expressions for the strain energy, kinetic energy, and nonconservative work.

2.2.2 *Strain Energy*

The differential strain energy can be written in Cartesian tensor notation as

$$dV = \frac{1}{2} \sigma_{ij} \varepsilon_{ij} \quad , \tag{2.2.2}$$

where the dummy subscripts i and j represent summations over the three coordinate dimensions. For the radial vibrations of thin rings, the following assumptions can be made. First, the stress is assumed to be planar; thus for a thin shell away from points of concentrated load,

$$\sigma_{zz} \approx 0 \qquad \text{and} \qquad \sigma_{xz} = \sigma_{yz} \approx 0 \quad . \tag{2.2.3a–b}$$

For the ring,

$$\sigma_{xx} \approx 0 \qquad \text{and} \qquad \sigma_{xy} \approx 0 \quad , \tag{2.2.4a–b}$$

which implies no axial force and no axial shearing forces. Thus the differential strain energy reduces to a single term:

$$dV = \frac{1}{2}\sigma_{yy}\varepsilon_{yy} \quad . \tag{2.2.5}$$

Again, as stated previously, this paper does not deal with material nonlinearities, so Hooke's Law may be used to relate stresses to strains (see Eq. 2.1.4) and the differential strain energy becomes

$$dV = \frac{E}{2}\varepsilon_{yy}^2 \quad . \tag{2.2.6}$$

The strain-displacement relation with geometric imperfections will be used as derived in Appendix A (Eq. A.10 and Eq. 2.1.5):

$$\varepsilon_{yy} = \frac{\partial v}{\partial y} + \frac{w}{R} - \frac{z}{R}\left(R\frac{\partial^2 w}{\partial y^2} - \frac{\partial v}{\partial y}\right) + \frac{1}{2}\left(\frac{\partial w}{\partial y}\right)^2 + \frac{\partial w}{\partial y}\frac{\partial \bar{w}}{\partial y} \quad . \tag{2.2.7}$$

The strain energy can now be determined through the integration of Eq. 2.2.6 over the thickness of the ring and around the circumference

$$V = \frac{E}{2}\int_0^{2\pi R} dy \int_{-h/2}^{h/2} [\varepsilon_{yy}]^2 \left(1+\frac{z}{R}\right) dz \quad . \tag{2.2.8}$$

Substituting the strain-displacement relation (Eq. 2.2.7) into the above expression yields

$$V = \frac{ER}{2}\int_0^{2\pi R} dy \int_{-h/2R}^{h/2R} \left[\alpha_1 - z'\alpha_2 + \alpha_3\right]^2 (1+z')\, dz' \quad , \tag{2.2.9}$$

where $\alpha_1 = \frac{\partial v}{\partial y} + \frac{w}{R}$, $\alpha_2 = R\frac{\partial^2 w}{\partial y^2} - \frac{\partial v}{\partial y}$, $\alpha_3 = \frac{1}{2}\left(\frac{\partial w}{\partial y}\right)^2 + \frac{\partial w}{\partial y}\frac{\partial \bar{w}}{\partial y}$, and $z' = \frac{z}{R}$.

Integrating Eq. 2.2.9 and keeping terms up to second order in z' yields

$$V = \frac{Eh}{2} \int_0^{2\pi R} \left[(\alpha_1 + \alpha_3)^2 + k \left(\alpha_2^2 - 2\, \alpha_1 \alpha_2 - 2\, \alpha_2 \alpha_3 \right) \right] dy \qquad (2.2.10)$$

where $k = \frac{h^2}{12R^2}$.

To apply Hamilton's principle, the first variation of the strain energy is needed. Applying the standard techniques of variational calculus to Eq. 2.2.10 yields

$$\begin{aligned} \delta V = Eh \int_0^{2\pi R} \Big\{ & \left[\alpha_1 + \alpha_3 - k\, \alpha_2 \right] \; \delta\alpha_1 + \\ & \left[k \left(\alpha_2 - \alpha_1 - \alpha_3 \right) \right] \delta\alpha_2 + \qquad (2.2.11) \\ & \left[\alpha_1 + \alpha_3 - k\, \alpha_2 \right] \delta\alpha_3 \Big\} \, dy \quad , \end{aligned}$$

where the variations $\delta\alpha_1$, $\delta\alpha_2$, and $\delta\alpha_3$ are taken with respect to v and w, respectively. Variations with respect to a particular variable will be denoted with a bar as

$\delta\alpha_1 \big|_w$ = the first variation of $\delta\alpha_1$ with respect to w, etc.

Using the definitions of α_1, α_2, and α_3, the variations are

$$\delta\alpha_1 \big|_w = \frac{\delta w}{R} \qquad \delta\alpha_1 \big|_v = \frac{\partial}{\partial y}(\delta v) \qquad (2.2.12a\text{-}b)$$

$$\delta\alpha_2 \big|_w = R \frac{\partial 2}{\partial y^2}(\delta w) \qquad \delta\alpha_2 \big|_v = - \frac{\partial}{\partial y}(\delta v) \qquad (2.2.13a\text{-}b)$$

$$\delta\alpha_3 \big|_w = \left(\frac{\partial w}{\partial y} + \frac{\partial \bar{w}}{\partial y} \right) \frac{\partial}{\partial y}(\delta w) \qquad \delta\alpha_3 \big|_v = 0 \quad . \qquad (2.2.14a\text{-}b)$$

To reduce the derivatives of the variations, it is necessary to integrate by parts as follows:

$$\int_0^{2\pi R} \gamma \frac{\partial}{\partial y}(\delta w)\, dy = \gamma\, \delta w \Big|_0^{2\pi R} - \int_0^{2\pi R} \frac{\partial \gamma}{\partial y}\, \delta w\, dy \qquad (2.2.15a)$$

$$\int_0^{2\pi R} \gamma \frac{\partial^2}{\partial y^2}(\delta w)\, dy = \gamma \frac{\partial}{\partial y}(\delta w) \Big|_0^{2\pi R} - \frac{\partial \gamma}{\partial y}(\delta w) \Big|_0^{2\pi R} + \int_0^{2\pi R} \frac{\partial^2 \gamma}{\partial y^2}\, \delta w\, dy \qquad (2.2.15b)$$

$$\int_0^{2\pi R} \gamma \frac{\partial}{\partial y}(\delta v)\, dy = \gamma\, \delta v \Big|_0^{2\pi R} - \int_0^{2\pi R} \frac{\partial \gamma}{\partial y}\, \delta v\, dy \quad , \qquad (2.2.15c)$$

where γ is defined as necessary when Eqs. 2.2.12-14 are substituted into Eq. 2.2.11.

With the application of Eqs. 2.2.15 on the substitution of Eqs. 2.2.12-14 into Eq. 2.2.11, two variations in V are obtained:

$$\delta V\Big|_w = Eh \int_0^{2\pi R} \Bigg\{ \frac{1}{R}\left(\alpha_1+\alpha_3-k\alpha_2\right) + kR\frac{\partial^2}{\partial y^2}\left(\alpha_2-\alpha_1-\alpha_3\right)$$

$$- \frac{\partial}{\partial y}\left[\left(\alpha_1+\alpha_3-k\alpha_2\right)\left(\frac{\partial w}{\partial y} + \frac{\partial \bar{w}}{\partial y}\right)\right]\Bigg\}\, \delta w\, dy \; +$$

$$Eh\left[\left(\alpha_1+\alpha_3-k\alpha_2\right)\left(\frac{\partial w}{\partial y} + \frac{\partial \bar{w}}{\partial y}\right) - kR\frac{\partial}{\partial y}\left(\alpha_2-\alpha_1-\alpha_3\right)\right] \delta w \Big|_0^{2\pi R} +$$

$$Eh\left[kR\left(\alpha_2-\alpha_2-\alpha_3\right)\right]\frac{\partial}{\partial y}(\delta w) \Big|_0^{2\pi R} \qquad (2.2.16a)$$

$$\delta V\big|_v = Eh \int_0^{2\pi R} \frac{\partial}{\partial y}\left[-(\alpha_1+\alpha_3)(1+k) + 2k\alpha_2\right] \delta v \, dy$$

$$+ \; Eh\left[(\alpha_1+\alpha_3)(1+k) - 2k\alpha_2\right]\delta v \Big|_0^{2\pi R} \quad . \qquad (2.2.16b)$$

These expressions (Eqs. 2.2.16a-b) are the variational form of the strain energy and will be used in the application of Hamilton's principle. The expressions for kinetic energy and virtual work will be developed next.

2.2.3 Kinetic Energy

The kinetic energy expression can be simply written for the translational components v and w without the kinetic energy of rotation:

$$T = \frac{\rho h}{2} \int_0^{2\pi R} \left[(\dot{w})^2 + (\dot{v})^2\right] dy \quad . \qquad (2.2.17)$$

The variational form of the kinetic energy is

$$\delta T = \rho h \int_0^{2\pi R} \left[\dot{w}\,\delta\dot{w} + \dot{v}\,\delta\dot{v}\right] dy \quad . \qquad (2.2.18)$$

Note that the variations in the time derivatives of w and v must be reduced. However, this must be handled in the full expression of Hamilton's principle since a time integral is needed for the application of the integration by parts.

2.2.4 Virtual Work

The virtual work of the nonconservative forces reduces to that of the external forces for an undamped system. The expression for the external loading (for a ring of unit width) is given by

$$\delta W_{nc} = \int_0^{2\pi R} q(y,t)\, \delta w\, dy \quad , \tag{2.2.19}$$

where the pressure q(y,t) is applied in the same direction as the positive virtual displacement δw.

2.2.5 Application of Hamilton's Principle

All the terms necessary for the application of Hamilton's principle have now been determined. The variational expressions for T, V, and W_{nc} are given by Eqs. 2.2.18, 2.2.16, and 2.2.19, respectively. When introduced into Eq. 2.2.1, a final integration by parts with respect to time must be applied for the kinetic energy terms. Two equations representing the variations with respect to w and v are obtained. Applying standard techniques of variational calculus, the partial differential equations of motion for v and w are determined to be

$$Eh\frac{\partial}{\partial y}\left[\frac{\partial v}{\partial y} + \frac{w}{R} + \frac{1}{2}\left(\frac{\partial w}{\partial y}\right)^2 + \frac{\partial w}{\partial y}\frac{\partial \bar{w}}{\partial y} + \underline{2}\,\frac{h^2}{12R^2}\left(\frac{\partial v}{\partial y} - R\frac{\partial^2 w}{\partial y^2}\right)\right] = \rho h\ddot{v} \tag{2.2.21a}$$

$$\begin{aligned}
&\frac{Eh^3}{12}\left\{\frac{\partial^4 w}{\partial y^4} - \frac{2}{\underline{R}}\frac{\partial^3 v}{\partial y^3} - \frac{1\,\partial^2 w}{\underline{R^2\partial y^2}} - \underline{\underline{\frac{1}{R}\left[\frac{\partial^2}{\partial y^2}\left\{\frac{1}{2}\left(\frac{\partial w}{\partial y}\right)^2\right\} + \frac{\partial^2}{\partial y^2}\left(\frac{\partial w}{\partial y}\frac{\partial \bar{w}}{\partial y}\right)\right]}}\right\} \\
&\quad - Eh\frac{\partial}{\partial y}\Biggl\{\Biggl[\frac{\partial v}{\partial y} + \frac{w}{R} + \frac{1}{2}\left(\frac{\partial w}{\partial y}\right)^2 + \frac{\partial w}{\partial y}\frac{\partial \bar{w}}{\partial y} \quad + \\
&\quad \frac{h^2}{12R^2}\left(\frac{\partial v}{\partial y} - R\frac{\partial^2 w}{\partial y^2}\right)\Biggr]\left(\frac{\partial w}{\partial y} \quad \underline{\underline{+\frac{\partial \bar{w}}{\partial y}}}\right)\Biggr\} + \frac{Eh}{R}\Biggl[\frac{\partial v}{\partial y} + \frac{w}{R} + \\
&\quad \frac{1}{2}\left(\frac{\partial w}{\partial y}\right)^2 + \frac{\partial w}{\partial y}\frac{\partial \bar{w}}{\partial y} + \frac{h^2}{12R^2}\left(\frac{\partial v}{\partial y} - R\frac{\partial^2 w}{\partial y^2}\right)\Biggr] + \rho h\ddot{w} = q(y,t) \quad ,
\end{aligned} \tag{2.2.21b}$$

where the underlined terms are the differences between the equations of motion above as derived from energy considerations and the equations of motion derived from the Sanders' modification to the Donnell-Mushtari shallow shell equations (Eqs. 2.1.8).

The terms that are single-underlined can be accounted for in Eqs. 2.1.8 if the $\frac{z}{R} \ll 1$ assumption is not applied in the force and moment resultant expressions (Eqs. 2.1.3) as indicated. The terms that are double-underlined are small nonlinear terms not accounted for in the shallow shell equation approach. The term that is triple-underlined is a geometric imperfection term that is not accounted for in the original form of the Donnell-Mushtari equations (Eqs. 2.1.1).

The object of deriving the equations of motion in two manners was twofold: (1) to fully understand the application of the shell equations to the ring, and (2) to understand the assumptions used in deriving the equations of motion. It is clear from the similarity between the two forms of the equations (Eqs. 2.1.8 and 2.2.21) that the Sanders' modification of the Donnell-Mushtari equations is valid for the analysis of thin rings. Note that the assumption $\frac{z}{R} \ll 1$ is used in both derivations. However, the Donnell-Mushtari equations alone are not sufficient for the analysis of low circumferential wavenumbers. Also, the effects of rotational inertia are ignored in both developments, though this point is made clear only in the kinetic energy terms of the energy approach.

The salient features of a system's dynamic equations of motion are that they are adequately accurate for the features that are relevant to the study and that they are not overly complicated so as to obscure the study. With this is mind, the equations of motion for the circular ring that will be used in the rest of this study are to be a combination of the best features of the simpler shallow shell equations and the more exact energy-derived equations.

Thus, returning to the energy-derived equations (Eqs. 2.2.21), the small nonlinear terms (double-underlined) will be neglected. The effects of the single-underlined terms are linear, but since the $\frac{z}{R} \ll 1$ assumption is considered valid, these will be neglected. Moreover, these terms are not included in the Sanders' equations quoted in Leissa (Ref. 39, pp. 32–35) or in Markus (Ref. 41, p. 72). The nonlinear and geometric imperfection terms of the equations are unaffected by these single-underlined linear terms. Thus, the accuracy of the equations of motion would not seem to be unduly compromised if these terms are neglected. The triple-underlined term is due to geometric imperfections and therefore may be important to understanding their effects. Thus, this term will also be kept.

To summarize then, the Sanders' modification of the Donnell-Mushtari equations reduced to apply to a circular ring will be used. These equations are augmented in that the first order geometric imperfection terms are included. These equations are stated below along with the boundary conditions.

2.2.6 Equations of Motion

$$Eh\frac{\partial}{\partial y}\left[\frac{\partial v}{\partial y}+\frac{w}{R}+\frac{1}{2}\left(\frac{\partial w}{\partial y}\right)^2+\frac{\partial w}{\partial y}\frac{\partial \bar{w}}{\partial y}+\frac{h^2}{12R^2}\left(\frac{\partial v}{\partial y}-R\frac{\partial^2 w}{\partial y^2}\right)\right]=\rho h\ddot{v} \qquad (2.2.22a)$$

$$\frac{Eh^3}{12}\left\{\frac{\partial^4 w}{\partial y^4}-\frac{1\partial^3 v}{R\partial y^3}\right\} - Eh\frac{\partial}{\partial y}\left\{\left[\frac{\partial v}{\partial y}+\frac{w}{R}+\frac{1}{2}\left(\frac{\partial w}{\partial y}\right)^2+\frac{\partial w}{\partial y}\frac{\partial \bar{w}}{\partial y}\right.\right.$$

$$\left.\left.+\frac{h^2}{12R^2}\left(\frac{\partial v}{\partial y}-R\frac{\partial^2 w}{\partial y^2}\right)\right]\left(\frac{\partial w}{\partial y}+\frac{\partial \bar{w}}{\partial y}\right)\right\}+\frac{Eh}{R}\left[\frac{\partial v}{\partial y}+\frac{w}{R}+\right.$$

$$\left.\frac{1}{2}\left(\frac{\partial w}{\partial y}\right)^2+\frac{\partial w}{\partial y}\frac{\partial \bar{w}}{\partial y}+\frac{h^2}{12R^2}\left(\frac{\partial v}{\partial y}-R\frac{\partial^2 w}{\partial y^2}\right)\right]+\rho h\ddot{w}=q(y,t) \quad . \qquad (2.2.22b)$$

2.2.7 Boundary Conditions

$$w(0,t)=w(2\pi R,t) \qquad \frac{\partial w}{\partial y}(0,t)=\frac{\partial w}{\partial y}(2\pi R,t) \qquad (2.2.23a\text{-}b)$$

$$\frac{\partial^2 w}{\partial y^2}(0,t)=\frac{\partial^2 w}{\partial y^2}(2\pi R,t) \qquad \frac{\partial^3 w}{\partial y^3}(0,t)=\frac{\partial^3 w}{\partial y^3}(2\pi R,t) \qquad (2.2.23c\text{-}d)$$

$$v(0,t)=v(2\pi R,t) \qquad \frac{\partial v}{\partial y}(0,t)=\frac{\partial v}{\partial y}(2\pi R,t) \quad . \qquad (2.2.24a\text{-}b)$$

2.3 GALERKIN'S PROCEDURE APPLIED TO THE RING EQUATIONS

In order to use the Galerkin procedure, admissible functions must be selected. Admissible functions are approximations to the deflection that must satisfy the geometric boundary conditions (Ref. 44, pp. 338-9). A general form for the radial deflection of the circular ring that satisfies the radial deflection boundary conditions may be written as

$$w(y,t) = \sum_{n=0}^{\infty} \left[A_n(t) \cos\left(\frac{ny}{R}\right) + B_n(t) \sin\left(\frac{ny}{R}\right) \right] \quad , \tag{2.3.1}$$

where A_n and B_n are periodic functions in time with period T such that $A_n(t) = A_n(t+T)$ and similarly for B_n. The functions $\cos\left(\frac{ny}{R}\right)$ and $\sin\left(\frac{ny}{R}\right)$ correspond to the n^{th} linear vibration mode of the ring. Note that $n=0$ corresponds to a breathing mode, $n=1$ corresponds to a rigid body mode, and $n>2$ are flexural modes (Appendix B contains brief descriptions and diagrams of the various mode shapes $n = 0$ to 5). Though the radial deflection boundary condition is satisfied by Eq. 2.3.1, it must be remembered that the tangential deflection boundary condition must also be satisfied.

In order to reduce all the partial derivatives in the equations of motion, a static deflection shape must also be defined for the geometric imperfections. The shape function can be written as an infinite Fourier series:

$$\bar{w}(y,t) = \sum_{n=2}^{\infty} \left[\delta_n \cos\left(\frac{ny}{R} + \phi_n\right) \right] \quad , \tag{2.3.2}$$

where δ_n and ϕ_n are the amplitude and spatial phase with respect to some fixed zero degree point of the nth component of the imperfection shape, respectively. The imperfection shape is flexural in nature, so the $n=0$ and $n=1$ components are not included. Important to the imperfections is that they are static and thus δ_n is <u>not</u> a function of time.

Using these forms (Eqs. 2.3.1–2) of the admissible function for w and the shape of $\bar{w}$, the partial differential equations (PDE) of motion can be reduced to ordinary differential equations (ODE) of motion.

In solving the equations of motion, it is often argued that the ring will vibrate in its lower modes in an inextensional manner; i.e., the mid-surface of the ring undergoes no stretching. A number of authors have investigated the importance of extension in the vibrations of circular rings and have produced varying criteria in the circumferential wavenumber, n, and the driving frequency, ω, for the proper application of the inextensional assumption.

One class of criteria relates the inextensional assumption to the natural frequency of the breathing mode, which can be written as (Ref. 12, p. 440)

$$\omega_0 = \sqrt{\frac{E}{\rho R^2}} \quad , \tag{2.3.3}$$

where the subscript of ω_0 corresponds to n=0, the breathing mode. Note that this frequency is not a function of the thickness of the ring. Evensen (Ref. 2, p. 43) determined that if the frequency of vibration, ω, is such that

$$\omega << \frac{\omega_0}{2} \quad , \tag{2.3.4a}$$

then the bending vibrations are basically inextensional. Philipson's (Ref. 45, p. 366) condition is similar, but without the $\frac{1}{2}$, i.e.,

$$\omega << \omega_0 \quad . \tag{2.3.4b}$$

These criteria, in essence, indicate that if the frequency of forced vibration is much less than the frequency of vibration of the lowest extensional mode of vibration, then the vibrations will be inextensional.

A second approach for the inextensional assumption involves the relative magnitudes of the wavelengths of the modes and the thickness of the ring. Goodier and McIvor (Ref. 25), for instance, indicate that for inextensional vibrations

$$\frac{n^2h^2}{12R^2} << 1 \quad , \tag{2.3.5}$$

or that the wavelengths of the modes considered must be large compared with the ring thickness.

For higher excitation frequencies (smaller wavelengths), the ring will vibrate in an extensional manner where stretching of the midplane does occur. As indicated by Evensen (Ref. 2, pp. 103-4), the inextensional modes of vibration used by Goodier and McIvor must satisfy a <u>linear</u> strain-displacement relation, not a nonlinear relation as considered in the present work. Thus, this criterion (Eq. 2.3.5) does not apply for this paper and Evensen's criterion (Eq. 2.3.4a), the most conservative of Evensen's and Philipson's, will be used for the inextensional criteria of this paper.

For inextensional vibrations, the working assumption is that the circumferential strain along the midplane (z=0) must be zero. Thus, from Eq. 2.2.7

$$\varepsilon_{yy}\big|_{z=0} = \frac{\partial v}{\partial y} + \frac{w}{R} + \frac{1}{2}\left(\frac{\partial w}{\partial y}\right)^2 + \frac{\partial w}{\partial y}\frac{\partial \bar{w}}{\partial y} = 0 \quad . \tag{2.3.6}$$

Using Eqs. 2.3.1–2, the derivative of v with respect to y may be solved for

$$\frac{\partial v}{\partial y} = -\frac{w}{R} - \frac{1}{2}\left(\frac{\partial w}{\partial y}\right)^2 - \frac{\partial w}{\partial y}\frac{\partial \bar{w}}{\partial y} \tag{2.3.7a}$$

$$= -\sum_{n=0}^{\infty}\left[\frac{A_n(t)}{R}\cos\left(\frac{ny}{R}\right) + \frac{B_n(t)}{R}\sin\left(\frac{ny}{R}\right)\right]$$

$$-\frac{1}{2}\left\{\sum_{n=1}^{\infty}\left[\frac{nA_n(t)}{R}\sin\left(\frac{ny}{R}\right) - \frac{nB_n(t)}{R}\cos\left(\frac{ny}{R}\right)\right] \mathrm{X}\right.$$

$$\left.\sum_{m=1}^{\infty}\left[\frac{mA_m(t)}{R}\sin\left(\frac{my}{R}\right) - \frac{mB_m(t)}{R}\cos\left(\frac{my}{R}\right)\right]\right\}$$

$$-\left\{\sum_{n=1}^{\infty}\left[\frac{nA_n(t)}{R}\sin\left(\frac{ny}{R}\right)-\frac{nB_n(t)}{R}\cos\left(\frac{ny}{R}\right)\right]\ \mathrm{X}\right.$$

$$\left.\sum_{m=2}^{\infty}\left[\frac{m\delta_m}{R}\sin\left(\frac{my}{R}+\phi_m\right)\right]\right\} \quad . \qquad (2.3.7b)$$

This equation may be separated into two parts, one which is a function of time only, $g_1(t)$, and the other which is a function both of time and y, $g_2(y,t)$:

$$\frac{\partial v}{\partial y} = -\,g_1(t)\ -\ g_2(y,t) \quad . \qquad (2.3.7c)$$

By expanding the summations of 2.3.7b and using various trigonometic identities

$$g_1(t) = \frac{A_0(t)}{R} + \frac{1}{4}\sum_{n=1}^{\infty}\frac{n^2}{R^2}\left[A_n^2(t) + B_n^2(t) + 2\delta_n\left(A_n(t)\cos\phi_n - B_n(t)\sin\phi_n\right)\right] (2.3.8a)$$

and

$$g_2(t) = \sum_{n=1}^{\infty}\frac{1}{R}\left[A_n(t)\cos\left(\frac{ny}{R}\right) + B_n(t)\sin\left(\frac{ny}{R}\right)\right] +$$

$$\frac{1}{4}\sum_{n=1}^{\infty}\frac{n^2}{R^2}\left[\left(B^2{}_n(t) - A_n^2(t)\right)\cos\left(\frac{2ny}{R}\right) - 2A_n(t)\,B_n(t)\sin\left(\frac{2ny}{R}\right)\right] -$$

$$\frac{1}{2}\sum_{n=2}^{\infty}\frac{n^2}{R^2}\delta_n\left[A_n(t)\cos\left(\frac{2ny}{R}+\phi_n\right) + B_n(t)\sin\left(\frac{2ny}{R}+\phi_n\right)\right] +$$

$$\frac{1}{4}\sum_{\substack{n=1\\ n\neq m}}^{\infty}\sum_{m=1}^{\infty}\frac{mn}{R^2}\left[\left(B_n(t)B_m(t) - A_n(t)A_m(t)\right)\cos\left(\frac{(m+n)y}{R}\right)\right.$$

$$\left. +\ \left(B_n(t)B_m(t) + A_n(t)A_m(t)\right)\cos\left(\frac{(m-n)y}{R}\right)\right.$$

$$- \left(A_n(t)B_m(t) + A_m(t)B_n(t)\right) \sin\left(\frac{(m+n)y}{R}\right)$$

$$- \left(A_m(t)B_n(t) - A_n(t)B_m(t)\right) \sin\left(\frac{(m-n)y}{R}\right)\Bigg] \; +$$

$$\frac{1}{2}\sum_{\substack{n=1\\n\neq m}}^{\infty}\sum_{m=2}^{\infty}\frac{mn}{R^2}\,\delta_m\Bigg\{A_n(t)\left[\cos\left(\frac{(m-n)y}{R}+\phi_m\right)-\cos\left(\frac{(m+n)y}{R}+\phi_m\right)\right]$$

$$- B_n(t)\left[\sin\left(\frac{(m-n)y}{R}+\phi_m\right)+\sin\left(\frac{(m+n)y}{R}+\phi_m\right)\right]\Bigg\} \quad , \qquad (2.3.8b)$$

where it can be seen that $g_2(y,t)$ is periodic in y such that $g_2(0,t) = g_2(2\pi R,t)$. This form for $\frac{\partial v}{\partial y}$ satisfies the slope continuity condition (i.e., $\frac{\partial v}{\partial y}(y=0) = \frac{\partial v}{\partial y}(y=2\pi R)$). Direct integration of Eq. 2.3.7c with respect to y yields

$$v \;=\; g_0(t) \;-\; g_1(t)\,y \;-\; g_3(y,t) \quad , \qquad (2.3.9)$$

which cannot satisfy the displacement continuity criterion unless $g_1(t)$ is identically zero. (Note that the integral of the function $g_2(y,t)$, which contains only linear periodic terms, is also a periodic function). Thus,

$$g_1(t) = 0 \qquad (2.3.10a)$$

or

$$\frac{A_0(t)}{R} + \frac{1}{4}\sum_{n=1}^{\infty}\frac{n^2}{R^2}\left[A_n^2(t) + B_n^2(t) + 2\delta_n\left(A_n(t)\cos\phi_n - B_n(t)\sin\phi_n\right)\right] = 0 \quad . \qquad (2.3.10b)$$

Solving for A_0 yields

$$A_0 \;=\; -\frac{1}{4}\sum_{n=1}^{\infty}\frac{n^2}{R}\left[A_n^2(t) + B_n^2(t) + 2\delta_n\left(A_n(t)\cos\phi_n - B_n(t)\sin\phi_n\right)\right] \quad . \qquad (2.3.11)$$

Thus, the inextensional form for the assumed mode shape is

$$w(y,t) = \sum_{n=1}^{\infty} \left[A_n(t)\cos\left(\frac{ny}{R}\right) + B_n(t)\sin\left(\frac{ny}{R}\right)\right] -$$

$$\frac{1}{4}\sum_{n=1}^{\infty} \frac{n^2}{R}\left[A_n{}^2(t) + B_n{}^2(t) + 2\delta_n\big(A_n(t)\cos\phi_n - B_n(t)\sin\phi_n\big)\right] \quad . \qquad (2.3.12)$$

Using the inextensional assumption (Eq. 2.3.6), the partial differential equations of motion are reduced to

$$Eh\frac{\partial}{\partial y}\left[\frac{h^2}{12R^2}\left(\frac{\partial v}{\partial y} - R\frac{\partial^2 w}{\partial y^2}\right)\right] = \rho h\ddot{v} \qquad (2.3.13a)$$

$$\frac{Eh^3}{12}\Bigg\{\frac{\partial^4 w}{\partial y^4} - \frac{1\partial^3 v}{R\partial y^3} - \frac{1}{R^2}\frac{\partial}{\partial y}\left[\left(\frac{\partial v}{\partial y} - R\frac{\partial^2 w}{\partial y^2}\right)\left(\frac{\partial w}{\partial y} + \frac{\partial \bar{w}}{\partial y}\right)\right]$$

$$+\frac{1}{R^3}\left(\frac{\partial v}{\partial y} - R\frac{\partial^2 w}{\partial y^2}\right)\Bigg]\Bigg\} + \rho h\ddot{w} = q(y,t) \quad . \qquad (2.3.13b)$$

Before substituting the assumed deflection and geometric imperfecton shapes, tangential inertia will be neglected. This assumption ($\rho h\,\ddot{v} = 0$) is much less limiting than that of the inextensional assumption. Evensen (Ref. 2, p. 30) has shown that this approximation is valid for

$$\omega^2 << n^2\,\omega_0{}^2 \quad , \qquad (2.3.14)$$

where, again, ω_0 is the natural frequency of the breathing mode. A comparison of this criterion with Evensen's inextensional criterion (Eq. 2.3.4a) shows that if the inextensional assumption is valid, then the neglecting of tangential inertia is certainly justifiable.

If tangential inertia is neglected, Eq. 2.3.13a reduces to

$$Eh\frac{\partial}{\partial y}\left[\frac{h^2}{12R^2}\left(\frac{\partial v}{\partial y} - R\frac{\partial^2 w}{\partial y^2}\right)\right] = \rho h\ddot{v} = 0 \quad , \qquad (2.3.15)$$

which can only be satisfied if

$$\frac{\partial}{\partial y}\left[\left(\frac{\partial v}{\partial y} - R\frac{\partial^2 w}{\partial y^2}\right)\right] = 0 \tag{2.3.16a}$$

or

$$\left(\frac{\partial v}{\partial y} - R\frac{\partial^2 w}{\partial y^2}\right) = \text{fnct}(t) \quad . \tag{2.3.16b}$$

As shown earlier, the tangential displacement boundary condition requires that $\frac{\partial v}{\partial y}$ must not contain terms that are functions of time only. Since all of the terms of $\frac{\partial^2 w}{\partial y^2}$ are periodic functions of y, it is easily seen that fnct(t) = 0 in Eq. 2.3.16b and thus,

$$\left(\frac{\partial v}{\partial y} - R\frac{\partial^2 w}{\partial y^2}\right) = 0 \quad . \tag{2.3.17}$$

Thus, with the inextensional vibration assumption and the neglecting of tangential inertia, the dynamic response of the transverse vibrations of circular rings reduces to a single partial differential equation of motion:

$$\frac{Eh^3}{12}\left[\frac{\partial^4 w}{\partial y^4} - \frac{1\partial^3 v}{R\partial y^3}\right] + \rho h\ddot{w} = q(y,t) \quad . \tag{2.3.18}$$

This equation can be written entirely in terms of w using the solution for $\frac{\partial v}{\partial y}$ from the inextentional result (Eq. 2.3.7a):

$$\frac{Eh^3}{12}\left\{\frac{\partial^4 w}{\partial y^4} + \frac{1\,\partial^2}{R\partial y^2}\left[\frac{w}{R} + \frac{1}{2}\left(\frac{\partial w}{\partial y}\right)^2 + \frac{\partial w}{\partial y}\frac{\partial \bar{w}}{\partial y}\right]\right\} + \rho h\ddot{w} = q(y,t) \quad . \tag{2.3.19}$$

Along with the inextensional assumption and the neglection of tangential inertia, additional assumptions used in the derivation of this equation should be restated. The circular ring is considered to be thin such that $\frac{h}{R} << 1$. Shearing strains and rotary inertia have been neglected. Evensen has shown that shearing and rotary inertia effects can be neglected if

$$\frac{n^2h^2}{3R^2} << 1 \quad , \tag{2.3.20}$$

which is even less restrictive than that for tangential inertia of thin rings. Thus, the assumption of inextensionality is the most limiting of the assumptions used in the derivation of this partial differential equation of motion.

An ordinary differential equation of motion can now be derived from this partial differential equation (Eq. 2.3.18) using the assumed mode shape for the inextensional case (Eq. 2.3.12) and the solution for $\frac{\partial v}{\partial y}$ (Eq. 2.3.7c):

$$\begin{aligned} &\frac{Eh^3}{12}\left[\sum_{n=1}^{\infty} \frac{n^4}{R^4}\left[A_n(t)\cos\left(\frac{ny}{R}\right) + B_n(t)\sin\left(\frac{ny}{R}\right)\right] + \frac{1}{R}\frac{\partial^2}{\partial y^2}[g_2(y,t)]\right] + \\ &\qquad \rho h \sum_{n=1}^{\infty}\left\{\ddot{A}_n(t)\cos\left(\frac{ny}{R}\right) + \ddot{B}_n(t)\sin\left(\frac{ny}{R}\right) - \frac{1n^2}{2R}\left[\dot{A}_n^2(t) + A_n(t)\ddot{A}_n(t) + \right.\right. \\ &\qquad\qquad \left.\left.\dot{B}_n^2(t) + B_n(t)\ddot{B}_n(t) - \delta_n\left(\ddot{A}_n(t)\cos\phi_n - \ddot{B}_n(t)\sin\phi_n\right)\right]\right\} = q(y,t) \quad , \end{aligned} \tag{2.3.21}$$

where $g_2(y,t)$ is defined as in Eq. 2.3.8b. Note that this is an equation of motion that defines the dynamic amplitude functions $A_n(t)$ and $B_n(t)$. The solutions of these functions must then be substituted into the assumed displacement solution for $w(y,t)$ (Eq. 2.3.12) to determine the actual transverse motion of the circular ring.

An analysis of the forcing function $q(y,t)$ allows the further simplification of Eq. 2.3.21. Experimentally (see Section 3) the ring will be excited at a single point. Thus, the forcing function can be written as

$$q(y,t) = \delta^k(y_o)\, q(t) \quad , \tag{2.3.22}$$

where $\delta^k(y_0)$ is the Dirac delta function which describes a spatial impulse applied at the circumferential location y_0, and $q(t)$ is the time amplitude function of this spatial input. Without loss of generality, the point of application of the force will be defined as $y_0 = 0$.

Examining the linear terms of the dynamic equation of motion (Eq. 2.3.21) shows that $A_n(t)$ is directly excited by this point input force since $y = 0$ is an anti-node of the cosine modal components. In the absence of geometric imperfections, $B_n(t)$, however, is not linearly excited since the input will lie at a node of the sine modes. Thus $A_n(t)$ has been labeled the ampltiude of the nth driven mode of the solution while $B_n(t)$ is the amplitude of the nth companion mode (Ref. 21, p. 556). By examining the nonlinear function $g_2(y,t)$, it can be shown that the companion mode can be indirectly excited through the nonlinear interactions since $B_n(t)$ multiplies terms such as $\cos\left(\frac{(m+n)y}{R}\right)$ and $\cos\left(\frac{(m-n)y}{R}\right)$.

Evensen has performed a detailed analysis of the excitation of the companion modes. He has determined that the companion modes will have nonzero amplitudes only in a small region surrounding natural frequencies of vibrations. In non-dimensional notation, the regions of instabiliy where the companion modes are excited are bounded by (Ref. 21, p. 555):

$$1 - \frac{\varepsilon a_n^2}{8} + O[\varepsilon^2] < \Omega < 1 + \frac{\varepsilon a_n^2}{8} + O[\varepsilon^2] \quad , \tag{2.3.23}$$

where $\varepsilon = \left(\frac{n^2 h}{R}\right)^2 \quad a_n = \frac{A_n}{h} \quad \Omega = \frac{\omega}{\omega_M}$

and ω_M is the linear natural frequency defined by Evensen (Ref. 21, p. 554) as

$$\omega_M{}^2 = \frac{E}{\rho R^2} \frac{(n^2 - 1)^2}{12} \left(\frac{h}{R}\right)^2 \quad .$$

If the amplitudes of excitation are less than the thickness of the ring, then the regions of companion mode excitation will be extremely narrow regions about the natural frequencies of flexural ring vibration. Thus, except for rather limited types of excitation, the transverse vibrations may be defined entirely in terms of the driven modes, and $B_n(t)$ can be set to zero for all n.

2.3.1 Assumed Mode Shape and Dynamic Amplitude Function

Thus the assumed mode shape and the dynamic amplitude function for the analysis of nonlinear transverse ring vibrations with geometric imperfections accounted for are finally established. For inextensional vibrations where only the driven modes are considered, the dynamic deflection shape can be described, referring to Eq. 2.3.12, by

$$w(y,t) = \sum_{n=1}^{\infty} \left[A_n(t) \cos\left(\frac{ny}{R}\right) - \frac{n^2}{4R} \left(A_n^2(t) + 2\delta_n A_n(t) \cos\phi_n \right) \right] . \qquad (2.3.24)$$

The dynamic amplitude functions $A_n(t)$ are then defined by

$$\frac{Eh^3}{12} \left[\sum_{n=1}^{\infty} \frac{n^4}{R^4} \left[A_n(t) \cos\left(\frac{ny}{R}\right) \right] + \frac{1}{R} \frac{\partial^2}{\partial y^2} [g_{2M}(y,t)] \right] +$$

$$\rho h \sum_{n=1}^{\infty} \left[\ddot{A}_n(t) \cos\left(\frac{ny}{R}\right) - \frac{n^2}{2R} \left(\dot{A}_n^2(t) + A_n(t) \ddot{A}_n(t) - \delta_n \ddot{A}_n(t) \cos\phi_n \right) \right]$$

$$= q(y,t) \quad , \qquad (2.3.25)$$

where

$$g_{2M}(y,t) = \sum_{n=1}^{\infty} \left[\frac{1}{R} A_n(t) \cos\left(\frac{ny}{R}\right) - \frac{n^2}{4R^2} A_n^2(t) \cos\left(\frac{2ny}{R}\right) \right]$$

$$- \frac{1}{2} \sum_{n=2}^{\infty} \frac{n^2}{R^2} \delta_n \left[A_n(t) \cos\left(\frac{2ny}{R} + \phi_n\right) \right]$$

$$+ \frac{1}{4} \sum_{\substack{n=1 \\ n \neq m}}^{\infty} \sum_{m=1}^{\infty} \frac{mn}{R^2} A_n(t) A_m(t) \left[\cos\left(\frac{(m-n)y}{R}\right) - \cos\left(\frac{(m+n)y}{R}\right) \right]$$

$$+ \frac{1}{2} \sum_{\substack{n=1 \\ n \neq m}}^{\infty} \sum_{m=2}^{\infty} \frac{mn}{R^2} \delta_m A_n(t) \left[\cos\left(\frac{(m-n)y}{R} + \phi_m\right) - \cos\left(\frac{(m+n)y}{R} + \phi_m\right) \right] .$$

(2.3.26)

Carrying out the differentiation of Equation 2.3.25 yields

$$\frac{Eh^3}{12}\left[\sum_{n=1}^{\infty}\frac{n^4}{R^4}\left[A_n(t)\cos\left(\frac{ny}{R}\right)\right]-g_{2M}(y,t)\right]+$$

$$\rho h\sum_{n=1}^{\infty}\left[\ddot{A}_n(t)\cos\left(\frac{ny}{R}\right)-\frac{n^2}{2R}\left(\dot{A}_n^2(t)+A_n(t)\ddot{A}_n(t)-\delta_n\ddot{A}_n(t)\cos\phi_n\right)\right]$$

$$=q(y,t)\quad,\tag{2.3.27}$$

where

$$g_{2M}(y,t)=\sum_{n=1}^{\infty}\left[\frac{n^2}{R^4}A_n(t)\cos\left(\frac{ny}{R}\right)-\frac{n^4}{R^5}A_n^2(t)\cos\left(\frac{2ny}{R}\right)\right]$$

$$-2\sum_{n=2}^{\infty}\frac{n^4}{R^5}\delta_n\left[A_n(t)\cos\left(\frac{2ny}{R}+\phi_n\right)\right]$$

$$+\sum_{n=1}^{\infty}\sum_{\substack{m=1\\ n\neq m}}^{\infty}\frac{mn}{4R^5}A_n(t)A_m(t)\left[(m-n)^2\cos\left(\frac{(m-n)y}{R}\right)-(m+n)^2\cos\left(\frac{(m+n)y}{R}\right)\right]$$

$$+\sum_{n=1}^{\infty}\sum_{\substack{m=2\\ n\neq m}}^{\infty}\frac{mn}{2R^5}\delta_mA_n(t)\left[(m-n)^2\cos\left(\frac{(m-n)y}{R}+\phi_m\right)-\right.$$

$$\left.(m+n)^2\cos\left(\frac{(m+n)y}{R}+\phi_m\right)\right]\quad.\tag{2.3.28}$$

These equations define the dynamic, ordinary differential equation of motion. These equations will be used throughout the remaining portions of this section to analyze nonlinear ring motion.

However, the dependence on the spatial variable is still present. The Galerkin's procedure, which is a particular method of weighted residuals, eliminates the spatial dependence by integrating a weighted product of the ordinary differential equation of motion over the spatial domain. The weighting function used in the Galerkin's procedure is of the same form as the assumed spatial mode (Eq. 2.3.24). To eliminate the dimensionality of this spatial mode, the weighted function used is of the form $\frac{\partial w}{\partial A_i}$, where A_i is the ith element of the assumed mode shape taken from the same domain as the number of assumed modes used in solving the problem. To more clearly explain the use of Galerkin's procedure, the solution for a single mode will be shown in detail.

2.3.2 Solution for Single Mode

As described, the Galerkin's procedure is used to reduce the spatially dependent equation of motion to a time only dependent equation. An example of the application of Galerkin's procedure to the circular ring will be developed for vibrations limited to a single mode, *m*, $m \neq 0$. For a single mode, the assumed mode shape is (referring to Eq. 2.3.24)

$$w(y,t) = \left[A_m \cos\left(\frac{my}{R}\right) - \frac{m^2}{4R}\left(A_m^2 + 2\delta_m A_m \cos\phi_m\right)\right] \quad . \tag{2.3.29}$$

It will be implied that for the rest of this discourse, the dynamic amplitude function is a function of time, $A_m = A_m(t)$. The dynamic amplitude function A_m is defined by the ODE (see Eq. 2.3.27):

$$\begin{aligned} &\frac{Eh^3}{12}\left[\frac{m^4 - m^2}{R^4} A_m \cos\left(\frac{my}{R}\right) + \frac{m^4}{R^5} A_m^2 \cos\left(\frac{2my}{R}\right) + \right. \\ &\qquad \left. 2\frac{m^4}{R^5}\delta_m A_m \cos\left(\frac{2my}{R} + \phi_m\right)\right] + \rho h\left[\ddot{A}_m \cos\left(\frac{my}{R}\right) - \right. \\ &\qquad \left. \frac{m^2}{2R}\left(\dot{A}_m^2 + A_m \ddot{A}_m - \delta_m \ddot{A}_m \cos\phi_m\right)\right] = q(y,t) \quad . \end{aligned} \tag{2.3.30}$$

To remove the spatial variable y from the above equations, Galerkin's procedure uses a weighting function of the form:

$$\text{Galerkin weighting function} = \frac{\partial w}{\partial A_i} \quad , \tag{2.3.31}$$

where the domain of the weighting function is the same as that for the assumed solution. Thus, for a single mode assumption, *i* = *m* and

$$\frac{\partial w}{\partial A_m} = \cos\left(\frac{my}{R}\right) - \frac{m^2}{2R}\left(A_m + \delta_m \cos\phi_m\right) \quad . \tag{2.3.32}$$

This choice of the weighting function maintains the equivalence of the Galerkin's procedure to the energy method which culminates in Lagrange's equations. Evensen has shown the equivalence of these two methods (Ref. 2, pp. 20-22). Singer (Ref. 46) has shown that this equivalence is dependent on the requirement that the original form of the differential equations must be used rather than a derivative as the Donnell shallow shell equation is frequently presented (see for instance Morley, Ref. 42). Since the original form of the ring equations is used in this paper, the equivalence of Galerkin's procedure to the energy method is guaranteed.

This weighting function is multiplied by Eq. 2.3.30 and the result is integrated over the spatial extent of the system:

$$\int_0^{2\pi R} \frac{\partial w}{\partial A_m} (\text{ Eq. 2.3.30 }) \, dy \Rightarrow \text{ ODE (function of time only)} \quad . \tag{2.3.33}$$

Taking proper account of the orthogonality conditions on cosines that result from this circular integration, the resulting ordinary differential equation for the dynamic amplitude is

$$\begin{aligned} &\frac{Eh^3}{12}\left(\frac{m^4-m^2}{R^4} A_m\right) + \\ &\quad \rho h\left[\ddot{A}_m + \frac{m^4}{2R^2}\left(\dot{A}_m^2 + \ddot{A}_m A_m - \delta_m \ddot{A}_m \cos\phi_m\right)\left(A_m + \delta_m \cos\phi_m\right)\right] \\ &\quad + \frac{m^2}{2\pi R^2}\left(A_m + \delta_m \cos\phi_m\right) Q_0(t) = \frac{Q_m(t)}{\pi R} \quad , \end{aligned} \tag{2.3.34}$$

where, if $q(y,t) = \delta^k(y_o)\, q(t)$ as mentioned above (Eq. 2.3.22),

$$Q_0(t) = \int_0^{2\pi R} q(y,t)\, dy = q(t) \tag{2.3.35}$$

and

$$Q_m(t) = \int_0^{2\pi R} q(y,t) \cos\left(\frac{my}{R}\right) dy = q(t) \cos\left(\frac{my_o}{R}\right) \quad . \tag{2.3.36}$$

Again, the complete solution must include the assumed mode solution (Eq. 2.3.29):

$$w(y,t) = \left[A_m \cos\left(\frac{my}{R}\right) - \frac{m^2}{4R}\left(A_m{}^2 + 2\delta_m A_m \cos\phi_m\right)\right] \quad .$$

It should be noted here that the selection of the mode, *m*, for the assumed solution is not an arbitrary choice. Since the spatial form of the input is a Dirac delta function, all spatial modes of the ring can be excited as shown in Eq. 2.3.36. In this equation $Q_m(t)$ is never zero strictly based on the spatial integration. However, as with all structures, the circular ring will respond with a mode shape *m*, which corresponds to the mode with a natural frequency that lies closest to the excitation frequency. This is most obvious in the case of resonance for which the frequency of excitation is exactly the same as the natural frequency of a particular mode. If the frequency of excitation lies between two natural frequencies, then both modes can potentially be excited in varying amplitudes depending upon the frequency response function of the structure. In this paper, though, it is assumed that the frequency of excitation is such that only one linear mode is excited for each freqency component in the input. Thus, an input frequency dominated by the frequency f_1 will produce a ring response dominated by the mode *m* that has a natural frequency that lies closest to f_1. (See specifically the discussion by Evensen, Ref. 2, pp. 91-93.)

2.3.3 Solution for Two Independent Modes

If a two-mode solution is assumed in which the two modes are independent of each other, the assumed solution becomes

$$
\begin{aligned}
w(y,t) = {} & \left[A_m \cos\left(\frac{my}{R}\right) - \frac{m^2}{4R}\left(A_m{}^2 + 2\delta_m A_m \cos\phi_m\right)\right] + \\
& \left[A_n \cos\left(\frac{ny}{R}\right) - \frac{n^2}{4R}\left(A_n{}^2 + 2\delta_n A_n \cos\phi_n\right)\right] \quad ,
\end{aligned}
\tag{2.3.37}
$$

where *m* and *n* are the independent wavenumber components of the solution. The defining ODE for the dynamic amplitude functions A_m and A_n becomes

$$
\begin{aligned}
& \frac{Eh^3}{12}\left[\frac{m^4}{R^4} A_m \cos\left(\frac{my}{R}\right) + \frac{n^4}{R^4} A_n \cos\left(\frac{ny}{R}\right) - \zeta_{mn}\right] + \\
& \quad \rho h\left[\ddot{A}_m \cos\left(\frac{my}{R}\right) + \ddot{A}_n \cos\left(\frac{ny}{R}\right) - \psi_m - \psi_n\right] \quad ,
\end{aligned}
\tag{2.3.38}
$$

where

$$
\begin{aligned}
\zeta_{mn} = {} & \left[\frac{n^2}{R^4} A_n \cos\left(\frac{ny}{R}\right) + \frac{m^2}{R^4} A_m \cos\left(\frac{my}{R}\right)\right] \\
& - \frac{n^4}{R^5} A_n{}^2 \cos\left(\frac{2ny}{R}\right) - \frac{m^4}{R^5} A_m{}^2 \cos\left(\frac{2my}{R}\right) \\
& - 2\frac{n^4}{R^5} \delta_n A_n \cos\left(\frac{2ny}{R} + \phi_n\right) - 2\frac{m^4}{R^5} \delta_m A_m \cos\left(\frac{2my}{R} + \phi_m\right) \\
& + \frac{1}{2}\,\frac{mn}{R^5} A_n A_m\left[(m-n)^2 \cos\left(\frac{(m-n)y}{R}\right) - (m+n)^2 \cos\left(\frac{(m+n)y}{R}\right)\right] \\
& + \frac{1}{2}\,\frac{mn}{R^5} \delta_m A_n\left[(m-n)^2 \cos\left(\frac{(m-n)y}{R} + \phi_m\right) - (m+n)^2 \cos\left(\frac{(m+n)y}{R} + \phi_m\right)\right] \\
& + \frac{1}{2}\,\frac{mn}{R^5} \delta_n A_m\left[(m-n)^2 \cos\left(\frac{(m-n)y}{R} - \phi_n\right) - (m+n)^2 \cos\left(\frac{(m+n)y}{R} + \phi_n\right)\right]
\end{aligned}
\tag{2.3.39}
$$

and

$$
\psi_i = \frac{i^2}{2R}\left(\dot{A}_i{}^2 + A_i \ddot{A}_i - \delta_i \ddot{A}_i \cos\phi_i\right) \quad ; \; i = m, n \quad .
\tag{2.3.40}
$$

Following through with the Galerkin's procedure results in two spatial integrations about two weighting functions:

$$\int_0^{2\pi R} \frac{\partial w}{\partial A_m}\,(\text{ Eq. 2.3.38 })\,dy \;\Rightarrow\; \text{ODE (function of time only)} \qquad (2.3.41a)$$

and

$$\int_0^{2\pi R} \frac{\partial w}{\partial A_n}\,(\text{ Eq. 2.3.38 })\,dy \;\Rightarrow\; \text{ODE (function of time only)} \quad . \qquad (2.3.41b)$$

Carrying out these integrations yields two coupled nonlinear ODEs:

$$\begin{aligned}
&\frac{Eh^3}{12}\left(\frac{m^4-m^2}{R^4}A_m\right)+\\
&\quad \rho h\left[\ddot{A}_m+\frac{m^4}{2R^2}\left(\dot{A}_m^2+\ddot{A}_mA_m-\delta_m\ddot{A}_m\cos\phi_m\right)\left(A_m+\delta_m\cos\phi_m\right)\right.\\
&\quad \left.+\frac{m^2n^2}{2R^2}\left(\dot{A}_n^2+\ddot{A}_nA_n-\delta_n\ddot{A}_n\cos\phi_n\right)\left(A_m+\delta_m\cos\phi_m\right)\right]\\
&\quad +\frac{m^2}{2\pi R^2}\left(A_m+\delta_m\cos\phi_m\right)Q_0(t)=\frac{Q_m(t)}{\pi R} \quad ,
\end{aligned} \qquad (2.3.42a)$$

and

$$\begin{aligned}
&\frac{Eh^3}{12}\left(\frac{n^4-n^2}{R^4}A_n\right)+\\
&\quad \rho h\left[\ddot{A}_n+\frac{n^4}{2R^2}\left(\dot{A}_n^2+\ddot{A}_nA_n-\delta_n\ddot{A}_n\cos\phi_n\right)\left(A_n+\delta_n\cos\phi_n\right)\right.\\
&\quad \left.+\frac{m^2n^2}{2R^2}\left(\dot{A}_m^2+\ddot{A}_mA_m-\delta_m\ddot{A}_m\cos\phi_m\right)\left(A_n+\delta_n\cos\phi_n\right)\right]\\
&\quad +\frac{n^2}{2\pi R^2}\left(A_n+\delta_n\cos\phi_n\right)Q_0(t)=\frac{Q_n(t)}{\pi R} \quad .
\end{aligned} \qquad (2.3.42b)$$

If $q(y,t) = \delta^k(y_o)\, q(t)$ as previously assumed, then the functions $Q_0(t)$, $Q_m(t)$, and $Q_n(t)$ are defined as

$$Q_0(t) = \int_0^{2\pi R} q(y,t)\, dy = q(t) \quad , \tag{2.3.43}$$

$$Q_m(t) = \int_0^{2\pi R} q(y,t) \cos\left(\frac{my}{R}\right) dy = q(t) \cos\left(\frac{my_o}{R}\right) \quad , \tag{2.3.44}$$

and

$$Q_n(t) = \int_0^{2\pi R} q(y,t) \cos\left(\frac{ny}{R}\right) dy = q(t) \cos\left(\frac{ny_o}{R}\right) \quad . \tag{2.3.45}$$

As described following the discussion of the single assumed mode response, the choice of the response modes, *m* and *n*, is not arbitrary. If, for instance, the input is composed of a single driving frequency component, then the *m* mode, say, will correspond to the mode with the natural frequency closest to the driving frequency. The same will be true for the second mode driven by a second frequency.

2.4 DISCUSSION OF SIGNIFICANT RESULTS FROM EQUATIONS OF MOTION

2.4.1 Single Mode Solution

Since a single spatial mode, *m*, is assumed, the flexural part of the solution contains only this single mode. Note that the dynamic ODE (Eq. 2.3.28) contains $\cos\left(\frac{2my}{R}\right)$ terms which are integrated to zero in the application of the method of weighted residuals (i.e., Galerkin's procedure). The time domain part of this flexural mode solution is derived from the dynamic amplitude ODE (Eq. 2.3.32) and thus will contain the transferred frequencies from the input function. If the geometric imperfections are neglected, the ODE contains linear terms proportional to A_m and cubic terms proportional to $\frac{m^4}{2R^2}\left(\dot{A}_m{}^2 + \ddot{A}_m A_m\right) A_m$. Thus, if small amplitudes of motion are considered and the input signal contains a single frequency ω, then the flexural waves will vibrate primarily at a frequency of ω and to a lesser extent at a frequency of 3ω.

The flexural mode solution also contains the contributions of the geometric imperfections. The dynamic solution corresponding to the wavenumber *m* will contain quadratic terms proportional to $\frac{m^4}{2R^2}\delta_m \cos\phi_m \dot{A}_m{}^2$. Only the imperfection form corresponding to the wavenumber *m* participates in the dynamic solution as all other components are not included in the single mode solution form. Thus, the geometric imperfections introduce a double frequency component, 2ω, of the flexural solution.

The double frequency component of the response, in addition to containing the geometric imperfection flexural wavenumber, also contains the breathing mode proportional to $\frac{m^2}{4R^2}A_m{}^2$. Thus, two wavenumbers are present in the nonlinearly generated double frequency solution, the flexural wavenumber, *m*, and the breathing mode wavenumber, zero.

The single frequency 2ω is composed of two distinct modes of vibration. To clarify, Table 2.4.1 indicates the type of frequency and wavenumber solutions expected in the single mode vibration. The terms that contribute to the various components have been nondimensionalized with

$$\tilde{A}_m = \frac{A_m}{h} , \quad \tilde{\delta}_m = \frac{\delta_m}{h} , \text{ and } \quad \tau = \omega_0 t \quad . \tag{2.4.1}$$

Note the two types of double frequency or quadratic response.†

Table 2.4.1
Wavenumber and Frequency Responses, Single Mode

Frequency	Amplitude Proportionality	Wave	Response
ω	$\tilde{A}_m$	m	**Linear Response**
2 ω	$\frac{m^4}{2}\left(\frac{h}{R}\right)^2 \tilde{\delta}_m \cos\phi_m \left(\frac{\partial \tilde{A}_m}{\partial t}\right)^2$	m	**Geometric Imperfection**
2 ω	$\frac{m^2}{4}\left(\frac{h}{R}\right) \tilde{A}_m{}^2$	0	**Breathing Mode**
3 ω	$\frac{m^4}{2}\left(\frac{h}{R}\right)^2 \left(\left(\frac{\partial \tilde{A}_m}{\partial t}\right)^2 + \left(\frac{\partial^2 \tilde{A}_m}{\partial t^2}\right)\right)\tilde{A}_m$	m	**Cubic Flexural**

---

† This list of possible wavenumber and frequency responses is not comprehensible since the parametric excitation terms are not included and all of the linear terms have not been included.

Though not fully investigated in this paper, the ring equations also exhibit parametric excitation features with the $Q_0(t)$ term (Eq. 2.3.35). This parametric excitation force is nonlinear, though not quadratic or cubic in nature.

2.4.2 *Two Mode Solution*

The two mode solution contains all of the mechanisms exhibited in the single mode solution. In particular the double frequency flexural mode response due to the imperfections is present as is the double frequency breathing mode response. However, the expression becomes more complicated since the modes are developed from two coupled differential equations.

Table 2.4.2 contains the two mode results comparable to the single mode solution except that the cubic terms have not been shown due to their complexity. In Table 2.4.2, ω_m indicates the input frequency that falls closest to the natural frequency of the mth wavenumber, and ω_n is the input frequency that is closest to the nth wavenumber natural frequency. Note that the expressions for the geometric imperfection terms become quite complicated in that both the *m* and *n* wavenumbers contain the $\cos\phi_m$ and $\cos\phi_n$ functions as well as the dynamic amplitude functions A_m and A_n. Thus, the location of the input to both the *m* and *n* geometric imperfection waveshapes will influence the double frequency response. Also, the breathing mode response can occur at two frequencies. This two mode solution begins to indicate the types of nonlinear wavenumber interactions that can occur in the nonlinear ring vibrations.

One interesting example of a two mode solution occurs when the input to the system comes from a quadratically nonlinear source so that $\omega_n = 2\,\omega_m$. Thus, Table 2.4.2 indicates that at the $\omega_n = 2\,\omega_m$ frequency, a linear response at the *n* wavenumber, a geometric imperfection response at the *m* wavenumber, and a breathing mode mechanisms can all occur. Thus, three distinct wavenumbers produced by three different sources (linear, geometric imperfections, and the geometric nonlinearities) can occur simultaneously at the same frequency. Again these wavenumber results are not comprehensive since the parametric excitation and the cubic response have not been examined in this example.

Table 2.4.2
Wavenumber and Frequency Responses, Two Modes

Frequency	Amplitude Proportionality	Wave	Response
ω_m	$\tilde{A}_m$	m	**Linear Response**
ω_n	$\tilde{A}_n$	n	**Linear Response**
$2\ \omega_m$	$\frac{m^2}{2}\left(\frac{h}{R}\right)^2 \Bigl\{ m^2\tilde{\delta}_m\cos\phi_m\left(\frac{\partial\tilde{A}_m}{\partial t}\right)^2 +$ $n^2\Bigl[\Bigl(\left(\frac{\partial\tilde{A}_n}{\partial t}\right)^2 + \frac{\partial^2\tilde{A}_n}{\partial t^2}\tilde{A}_n\Bigr)\tilde{\delta}_m\cos\phi_m$ $-\frac{\partial^2\tilde{A}_n}{\partial t^2}\tilde{A}_m\,\tilde{\delta}_n\cos\phi_n\Bigr]\Bigr\}$	m	**Geometric Imperfection**
$2\ \omega_n$	$\frac{n^2}{2}\left(\frac{h}{R}\right)^2 \Bigl\{ n^2\,\tilde{\delta}_n\cos\phi_n\left(\frac{\partial\tilde{A}_n}{\partial t}\right)^2 +$ $m^2\Bigl[\Bigl(\left(\frac{\partial\tilde{A}_m}{\partial t}\right)^2 + \frac{\partial^2\tilde{A}_m}{\partial t^2}\tilde{A}_m\Bigr)\tilde{\delta}_n\cos\phi_n$ $-\frac{\partial^2\tilde{A}_m}{\partial t^2}\tilde{A}_n\,\tilde{\delta}_m\cos\phi_m\Bigr]\Bigr\}$	n	**Geometric Imperfection**
$2\ \omega_m$	$\frac{m^2}{4}\left(\frac{h}{R}\right)\tilde{A}_m^2$	0	**Breathing Mode**
$2\ \omega_n$	$\frac{n^2}{4}\left(\frac{h}{R}\right)\tilde{A}_n^2$	0	**Breathing Mode**

This page intentionally left blank.

SECTION 3
EXPERIMENTAL INVESTIGATION

3.1 EXPERIMENTAL SET-UP AND CALIBRATION

As in all investigations, the analytical work can be truly verified only by an experimental investigation. The driving force behind the experimental investigation of nonlinear vibrations of circular rings is to better understand the various phenomena previously discussed. These phenomena include the usefulness of higher order spectral signal processing in investigating nonlinear vibrations, the effects of geometric imperfections on the wave response of the circular rings, and the presence of nonlinear wavenumber interactions.

The basic experimental set-up for the investigation of the nonlinear response of circular rings is shown in Fig. 3.1.1. All of the rings were composed of mild steel ASTM 1018 with the following assumed properties:

E = Young's modulus = 30×10^6 psi
ρ = weight density = 0.283 lb/in^3
ν = Poisson's ratio = 0.3

The input to the rings is accomplished via a thin 14 gauge steel wire held in high tension and attached to a point on the ring through a piezoelectric force gauge. The steel wire was excited by an electrodynamic shaker that was rigidly attached to it through a thin wire stinger. Thus the input system excited the interior of the ring at approximately a single circumferential point, y_o, which could be modeled analytically as a delta function, $\delta^k(y_o)$.

The displacement of the ring was measured with two noncontacting, inductance-type proximity probes. Both probes were located on the exterior surface of the ring with a fixed probe located at the input position directly opposite the force gauge input attachment point and an external probe that was free to rotate to any circumferential position about the ring. The probes were calibrated against the exterior surface of the ring so that material properties and curvature of the ring are accounted for. The calibration curves are shown in Appendix C. The linear displacement range of the probes is conservatively estimated to be 0.04 inches for both probes. The fixed probe was determined to have a sensitivity of $28.2\frac{\mathrm{V}}{\mathrm{in}}$, while the external probe had a sensitivity of

$27.6\,\frac{\text{V}}{\text{in}}$. During the experiment, the mean distance of the probes from the ring surface was monitored. This was done to ensure that the ring was near the midpoint of the linear range of the probes and thus guaranteed that the full linear range of the probes was utilized.

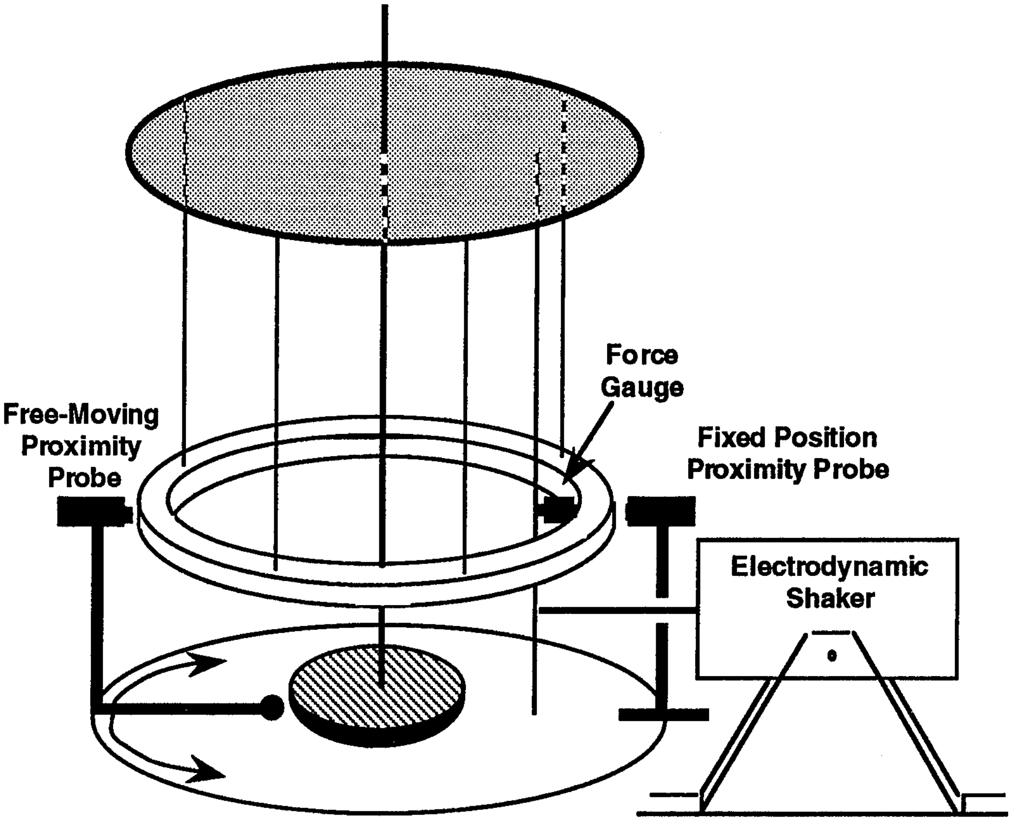

Figure 3.1.1
Set-Up of Physical Apparatus

AS-94-1147

The instrumentation used during the experiment is shown in Fig. 3.1.2. There are four major groups into which the instrumentation and experimental set-up can be divided. The input instrumentation group is used to produce the signal used to drive the electrodynamic shaker. This input system was capable of generating signals for which second and higher harmonic components were attenuated at least 60 dB. The input signal was monitored with an AC voltmeter as well as recorded by the data acquisition system. The electrodynamic shaker, force gauge, proximity probes, and the ring apparatus itself make up the hardware group (see Fig. 3.1.1).

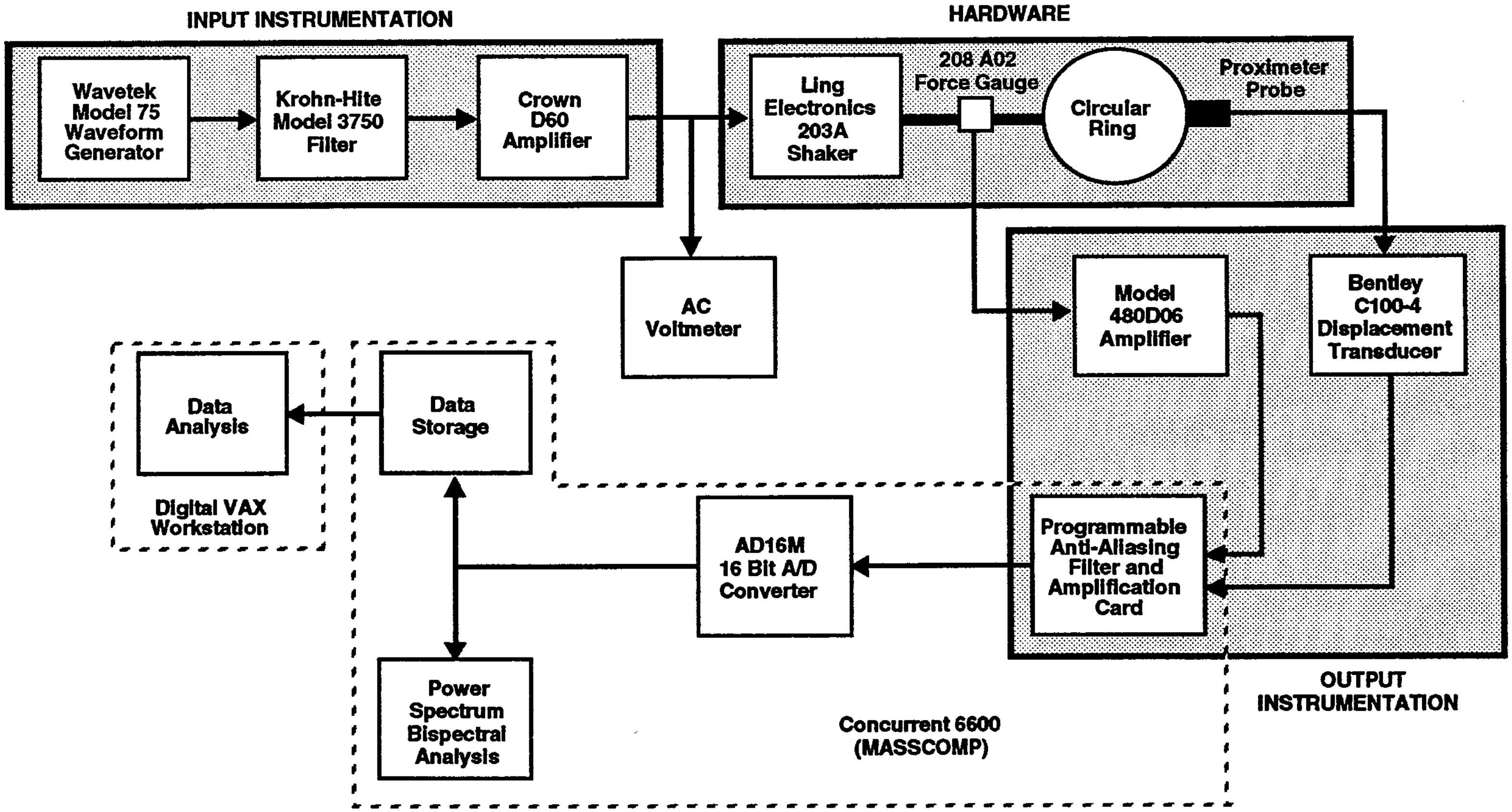

Figure 3.1.2
Ring Experiment Instrumentation

The force gauge and proximity probe signals were processed through the output instrumentation group, which amplified and filtered the signals. The filters consisted of high pass filters to reduce some of the low frequency noise and low pass analog filters to prevent aliasing. The cut-off frequencies as well as the amplification values were all controllable.

Finally the input, force gauge, and proximity probe signals were digitized and analyzed by a data acquisition and analysis system consisting of a Concurrent 6600 and a Digital VAX workstation. The Concurrent contained 16-bit data acquisition boards and real-time data analysis software for continual storage and monitoring of the data. The Concurrent was capable of calculating the power spectrum as well as the bispectrum (or bicoherency) of all the signals in real-time and displaying a single signal in a grayscale waterfall display.

The VAX was used to analyze the data in more detail after storage and thus was not used for real-time analysis. The system contained software that could calculate the power spectrum, bispectrum and bicoherency, spectral correlation, and cross-spectra of each of these. A description of the actual signal processing techniques will be mentioned as appropriate in describing the experimental results.

3.2 HIGHER ORDER SPECTRAL RESULTS

Some experimental results obtained from the nonlinear vibration studies of circular rings indicate a few of the interesting issues in the observability of power spectral and bicoherence vibration signatures. The single mode displacement response of a circular ring was estimated to be of the form

$$w(y,t) = A_n(t) \cos\frac{ny}{R} - \frac{n^2}{4R}\left[A^2_n(t) + 2A_n(t)\delta_n \cos\phi_n\right] ,$$

as shown previously (see Eq. 2.3.27). If the ring is excited by a single frequency, the dominant wavenumber of the response will be that wavenumber having natural frequency closest to the driving frequency. This assumes that all adjacent natural frequencies are approximately equally damped, as would be expected for a simple circular ring. The natural frequencies of four circular rings are listed in Appendix D.

For instance, the 0.073 inch thick circular ring is driven at a frequency of 199.22 Hz. An examination of the natural frequency information for this ring in Appendix D reveals that the n=3 wavenumber has the closest natural frequency at 218.8 Hz. Thus the dominant spatial wave response should be a second harmonic flexural mode corresponding to the n=3 wavenumber (see Fig. B.3b of Appendix B). A plot of the experimentally determined wavenumber response at the driving frequency shown in relative dB amplitude is shown in Fig. 3.2.1. Recalling that the dB scale is an absolute value scale, the n=3 wavenumber response can be clearly seen. The wavenumber response of the second harmonic of the driving frequency may have a more complex response as described in the analytical development of Section 2. The spatial wavenumber response of the circular ring is a topic that will be addressed in more detail in subsection 3.3.

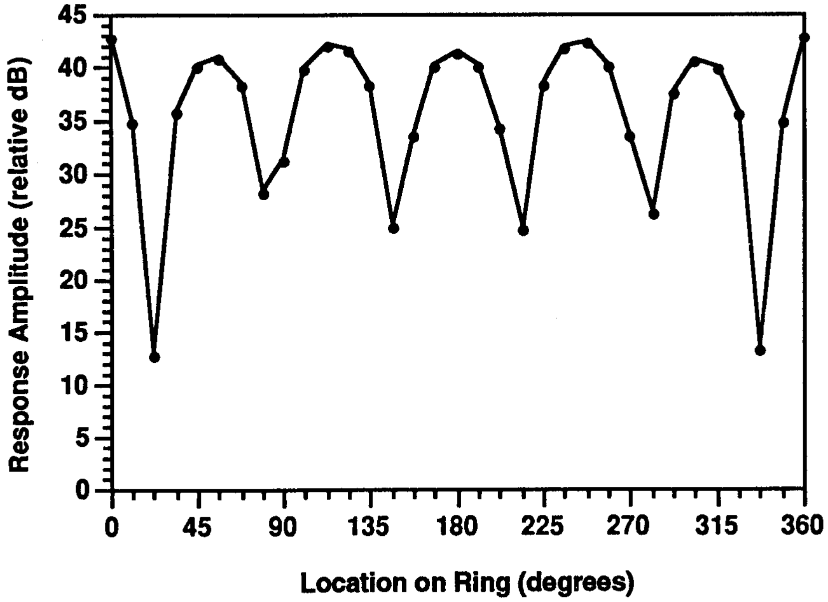

Figure 3.2.1
Wavenumber Response of 0.073 Inch Thick Ring at Driving Frequency (199.22 Hz)

AS-94-1149

As an example of the usefulness of higher order signal processing, the 0.073 inch thick circular ring was driven by a voltage having a power spectral signature going into the electrodynamic shaker as shown in Fig. 3.2.2. The signal is extremely clean in that there is no evidence, at least in the power spectrum, of any nonlinearities such as harmonic or subharmonic frequencies. The transfer function of an electrodynamic shaker has been shown to be inherently cubic in nature (Ref. 47). As expected, then, the power spectrum of the measured force gauge output of the electrodynamic shaker contains strong cubic spectral lines at frequencies three and six times the fundamental frequency (see Fig. 3.2.3). The bicoherency, however, will not detect cubic nonlinearities and thus should be null. As shown in Fig. 3.2.4, the bicoherence of electrodynamic shaker output indicates the presence of no significant quadratic nonlinearities or parametric interactions excluding the background noise peak.

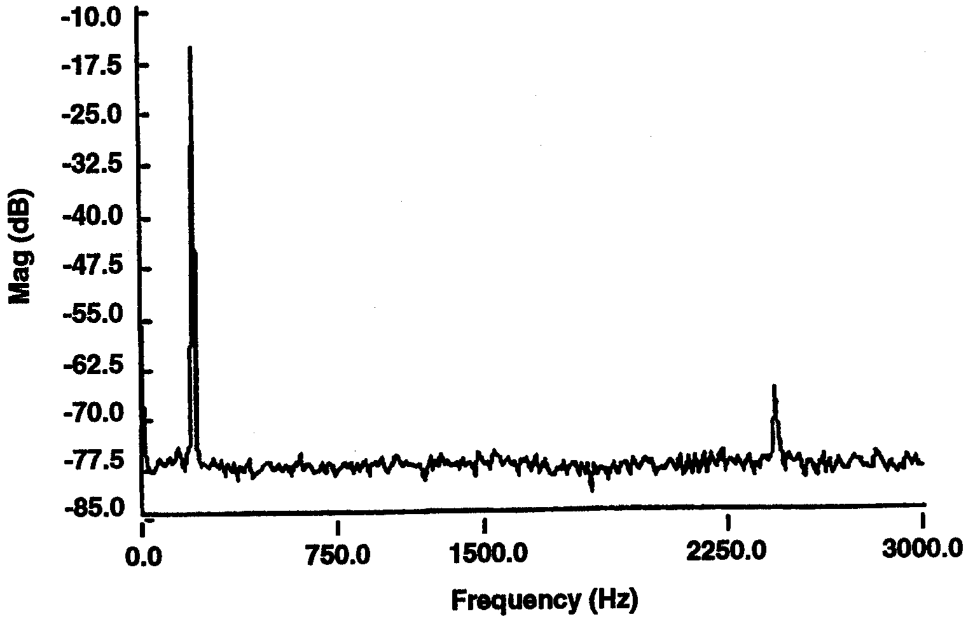

Figure 3.2.2
Power Spectrum of Voltage Input to Electromagnetic Shaker

AS-94-1150

Using the theoretical significance levels of Table 1.3.1, the 95% significance bicoherence amplitude is $b_{xx}^2(f_1,f_2) > 0.24$ for this case since there were 50 records. The 99% significance level is 0.30. The point shown on the autobicoherence of the force gauge has an amplitude equal to the 99% significance level but occurs at frequencies of 445 Hz and two times this frequency. These frequencies are not related to the force gauge or the ring system, and thus this autobicoherence point should be considered due to some extraneous noise source.

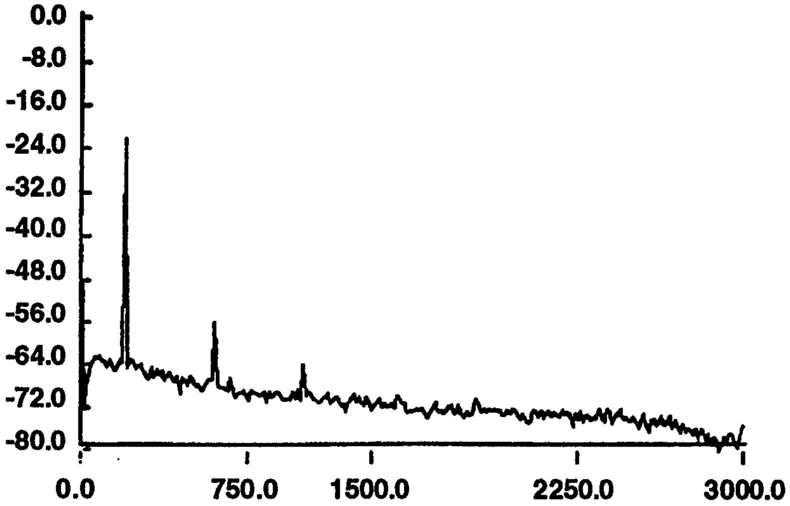

Figure 3.2.3
Power Spectrum of Force Gauge Measurement

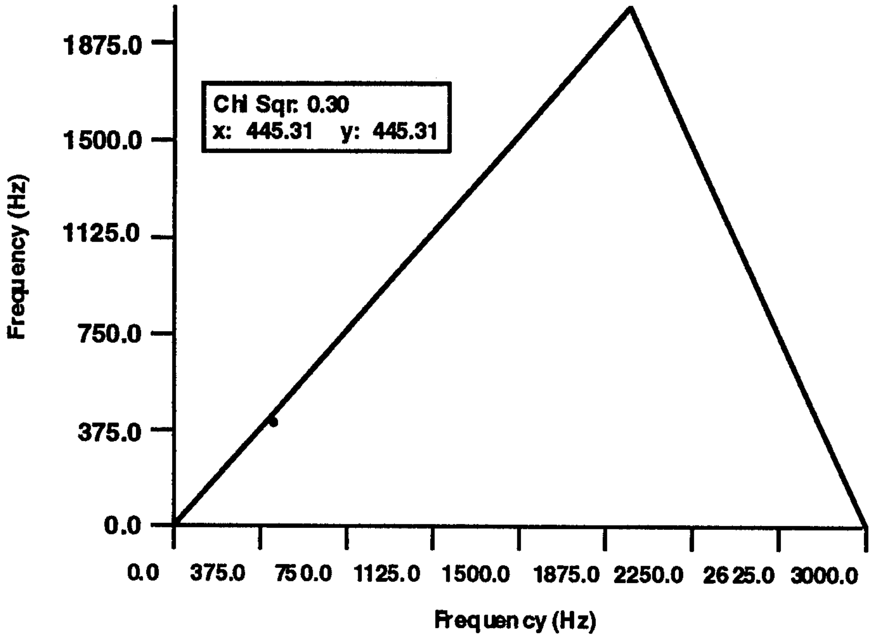

Figure 3.2.4
Auto Bicoherence of Force Gauge Measurement

AS-94-1151

The displacement of the circular ring, as measured with a single proximity probe, appears to respond in a purely linear fashion to the input of the fundamental frequency (Fig. 3.2.5). Only the fundamental frequency is observable in the power spectrum. Even the cubic harmonics present in the force gauge measurements are absent in the response spectrum. The conclusion from examining solely the input and output power spectrums could be that the ring is a linear system and does not appear to respond in a quadratically nonlinear fashion at all.

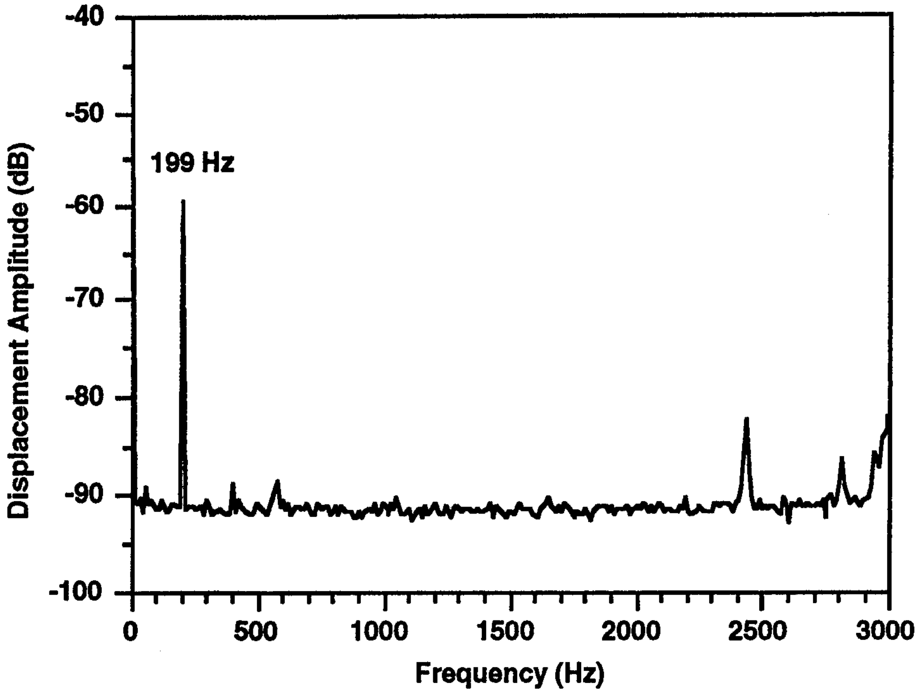

Figure 3.2.5
Power Spectrum of Ring Displacement Response

AS-94-1152

However, the response is not purely linear. The bicoherency of the ring displacement (Fig. 3.2.6) has a significant response at the (f_1, f_1, $f_1 + f_1$) location where f_1 is the fundamental frequency of excitation (199.22 Hz). The bicoherency signature indicates that there is a ring response at the $f_1 + f_1 = 398.44$ Hz frequency even though there is no evidence for this frequency present in the power spectral signatures. Thus, there is evidence that the ring is acting as a quadratically nonlinear system, this nonlinearity being clearly evident only in the output bicoherency. The input bicoherency signature being null indicates an insignificant quadratic element in the input.

Of course, the quadratic nature of the circular ring can be determined through analytical means as done in Section 2. However, these results provide evidence for the utility of higher order signal processing in detection of nonlinear processes. Each signal processing tool has its limitations (e.g., the bicoherency cannot detect cubic nonlinearities), but the arsenal of the complete higher order spectral signatures can provide a wealth of information concerning the true order of the system under study.

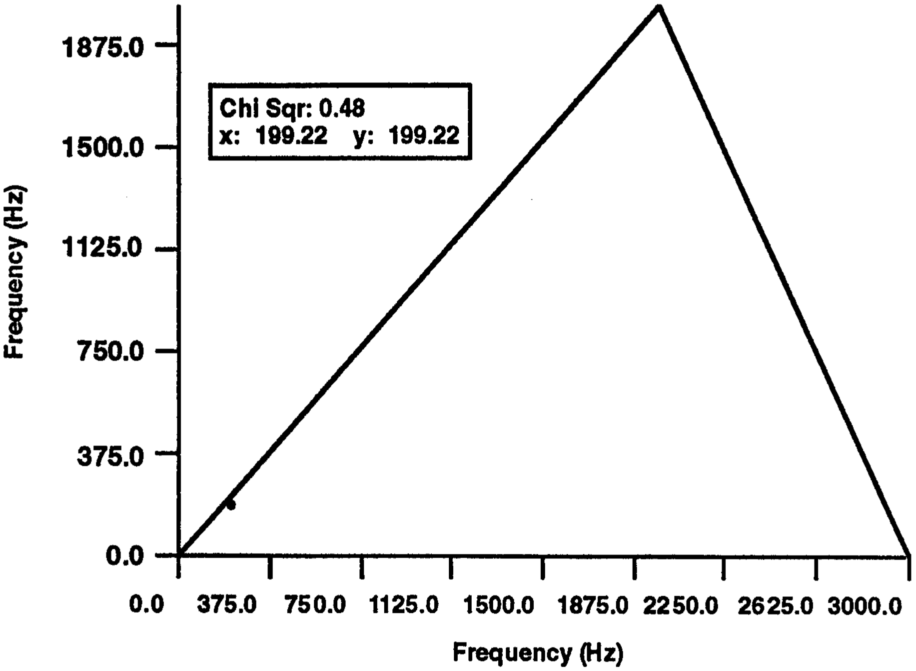

Figure 3.2.6
Auto Bicoherence of Ring Displacement Response

AS-94-1153

3.3 GEOMETRIC IMPERFECTION RESULTS

In order to understand the effects of geometric imperfections, the imperfections were first measured for each ring. Appendix E presents the detailed method and results from the geometric imperfection measurements. The measurements were made by a precision gauge deflection sensor with the rings mounted on a rotating platform. As shown in Appendix E, the imperfections are reasonably constant in the radial and axial directions; thus the assumption that the imperfections are only dependent upon the circumferential coordinate is justified.

The effect that the geometric imperfections have on the ring geometry can be clearly seen in Fig. 3.3.1 and Fig. 3.3.2. In these figures the actual geometric imperfections for the 0.034 and 0.073 inch thick rings are exaggerated. In essence, these rings are not perfectly axisymmetric. The position and amplitude of the individual wavenumber components of the geometric imperfections are revealed in Appendix E.

In Section 2, the effects of the geometric imperfections on the dynamic response were analytically investigated. For a single mode input, Table 2.4.1 indicates the expected results for the linear mode, the quadratic imperfection mode, the quadratic breathing mode, and the cubic mode. In this section the quadratic effects are experimentally investigated.

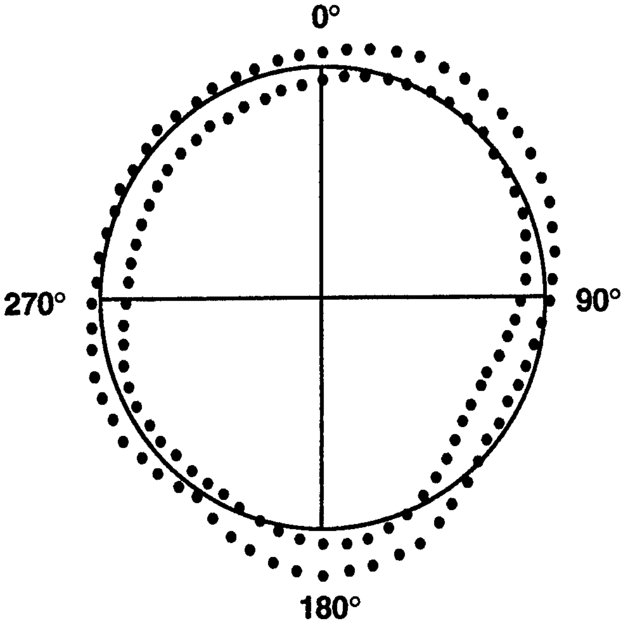

Figure 3.3.1
Exaggerated Geometric Imperfections for 0.034 Inch Thick Ring

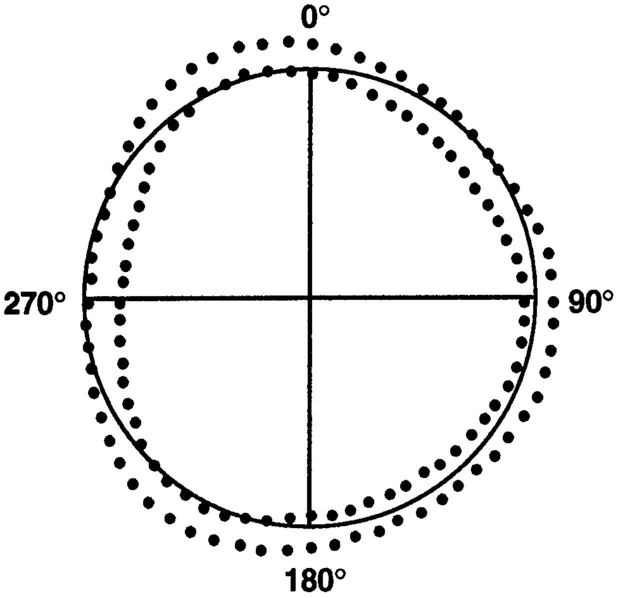

Figure 3.3.2
Exaggerated Geometric Imperfections for 0.073 Inch Thick Ring

From Section 2, the single mode solution was (see Eq. 2.3.29)

$$w(y,t) = \left[A_m \cos\left(\frac{my}{R}\right) - \frac{m^2}{4R}\left(A_m{}^2 + 2\delta_m A_m \cos\phi_m\right)\right] . \qquad (3.3.1)$$

From the differential equation of motion and the assumed mode solution, the response was determined to have the following linear, quadratic, and cubic major components written in nondimensional form (see Table 2.4.1):

$$\tilde{A}_m \qquad \text{linear frequency flexural mode} \qquad (3.3.2)$$

$$\frac{m^4}{2}\left(\frac{h}{R}\right)^2 \delta_m \cos\phi_m \left(\frac{\partial \tilde{A}_m}{\partial \tau}\right)^2 \qquad \text{quadratic frequency flexural mode} \qquad (3.3.3)$$

$$\frac{m^2}{4}\left(\frac{h}{R}\right)\tilde{A}_m{}^2 \qquad \text{quadratic breathing mode} \qquad (3.3.4)$$

$$\frac{m^4}{2}\left(\frac{h}{R}\right)^2 \left(\left(\frac{\partial \tilde{A}_m}{\partial \tau}\right)^2 + \left(\frac{\partial^2 \tilde{A}_m}{\partial \tau^2}\right)\right)\tilde{A}_m \qquad \text{cubic frequency flexural mode.} \qquad (3.3.5)$$

Thus, the ring will vibrate flexurally at the fundamental, quadratic, and cubic frequencies in the shape of the *m* wavenumber. In addition, the quadratic frequency should be excited in the form of the breathing mode.

A closer examination of the quadratic amplitude form (Eq. 3.3.3) reveals the dependency of the quadratic flexural response on $\cos\phi_m$ where ϕ_m is the geometric phase of the *m*th component of the geometric imperfections with respect to the input location. Two extremes of this phase are defined as

$$\cos\phi_m = 0 \qquad \text{orthogonal input} \qquad (3.3.6)$$

$$\cos\phi_m = 1 \qquad \text{affine input.} \qquad (3.3.7)$$

If the input position is located at a nodal point of a geometric imperfection component (i.e., the input and imperfection shape are out of phase with respect to each other), the input is considered orthogonal. If the input is located at A, physical description of these two inputs is shown in Fig. 3.3.3. The orthogonal input will not excite the quadratic flexural mode while the affine input will. The experiment was designed to investigate this hypothesis.

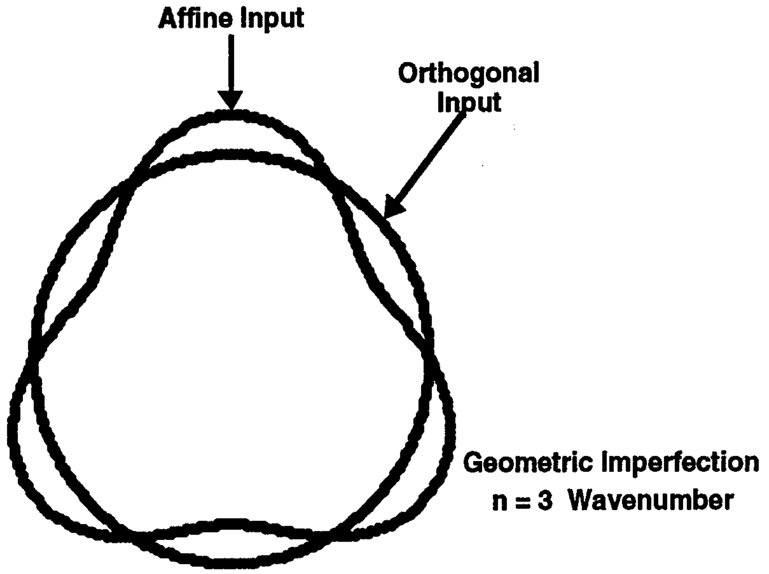

Figure 3.3.3
Affine and Orthogonal Inputs to Geometrically Imperfect Ring

AS-94-1155

The experiment was set up as described in subsection 3.1; however, the orientation of the ring in relation to the input frequency was not arbitrary. Using the geometric imperfection information as described in Appendix E, the ring was positioned so that there was either an affine or orthogonal input at the input frequency. For instance, if the input frequency was such that it linearly excited the *m* wavenumber, the ring was positioned so that the ring could be excited at a maximum of the imperfection for the affine input and at a zero crossing of the imperfection for the orthogonal input.

To measure the wavenumber response at each frequency, the displacement response at 1 of 16 evenly spaced points around the circumference of the ring and at the fixed input location were taken simultaneously. In the frequency domain, the amplitude of the response at the input frequency and at its second harmonic (double frequency) were determined as well as the positive or negative phase relationship between the response and the input displacements. It should be noted that the sampling rate of the data acquisition system was set so that an exact number of fundamental cycles could be measured in 512 points so that leakage was minimized. This was confirmed by online monitoring of the power spectrum of the response signals.

As a first example, a 176 Hz input frequency was applied to the 0.034 inch ring at the 30.8 degree circumferential location. This circumferential location corresponds to an affine input at the fourth wavenumber component of the geometric imperfections of this ring. This can be seen by referring to Figs. E.1.5a and E.1.5b in Appendix E and Table 3.3.1, which shows the wavenumbers, natural frequencies, and response frequencies that would be expected for this ring. In Table 3.3.1, the second column is the natural frequency of the wavenumber response as found in Appendix D. The third column lists the fundamental input frequency (176 Hz), the quadratic frequency response (352 Hz), and the cubic frequency response (528 Hz) with the wavenumber that has a natural frequency closest to the response frequency.

Table 3.3.1
Natural and Response Frequencies of the 0.034 Inch Ring

Wavenumber	Natural Frequency	Response Frequency
2	31.3 Hz	
3	93.8 Hz	
4	187.5 Hz	176 Hz
5	313 Hz	352 Hz
6	469 Hz	528 Hz
7	640 Hz	
8	844 Hz	

The response amplitude of the 0.034 inch thick ring at the fundamental input frequency of 176 Hz as measured at 16 evenly spaced points about the circumference of the ring is shown in Fig. 3.3.4. Note that, as expected, the response clearly shows the character of the fourth wavenumber at the fundamental input frequency. The spatial response at the second harmonic (352 Hz) of the fundamental input frequency is shown in Fig. 3.3.5. The spatial response at this frequency is more complicated, and no dominant response wavenumber is apparent in this plotting domain. The spatial Fourier domain (i.e., the wavenumber domain) can be used to examine the content of the spatial wavenumbers at this second harmonic frequency.

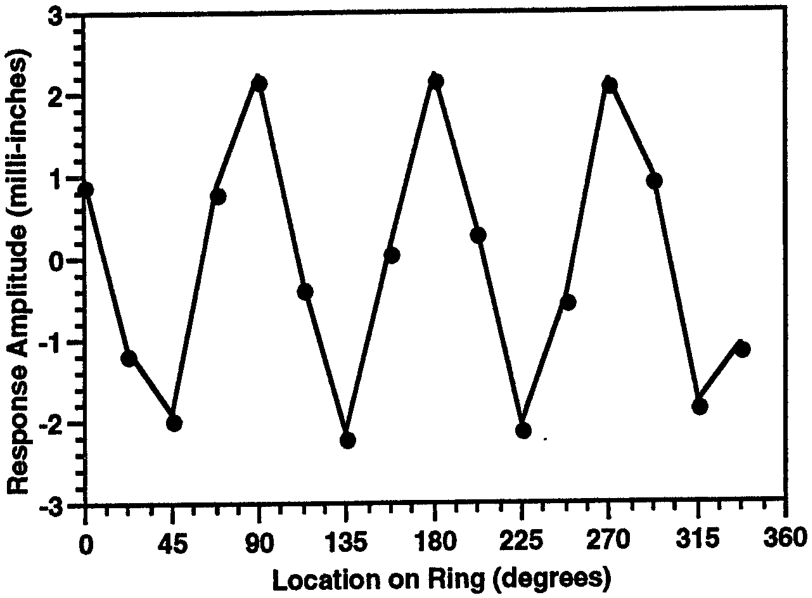

Figure 3.3.4
F_1 Frequency Affine Amplitude Response

0.034 inch ring I F_1 = 176 Hz I $\theta_{input} = 30.8^\circ$

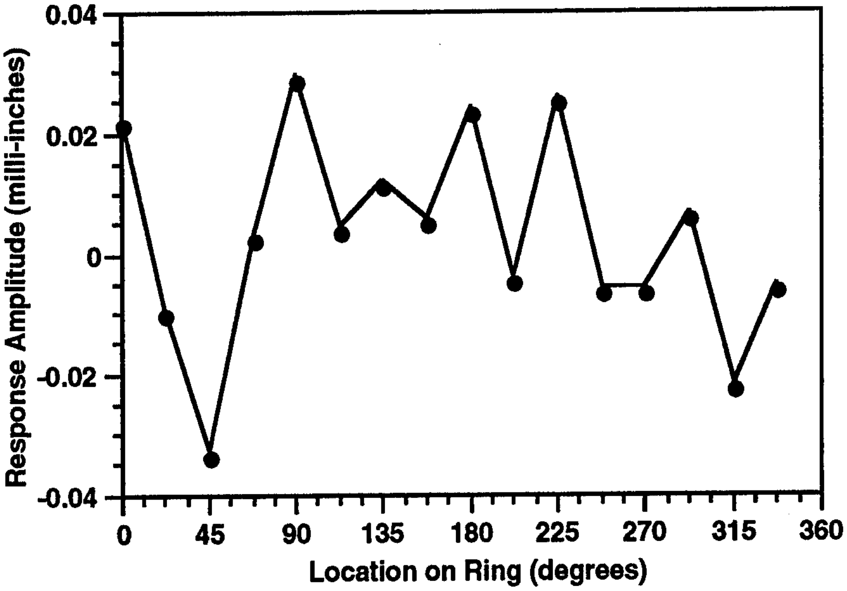

Figure 3.3.5
F_2 Frequency Affine Amplitude Response

0.034 inch ring I F_1 = 176 Hz I F_2 = 352 Hz I $\theta_{input} = 30.8^\circ$

Before discussing the results obtained using the wavenumber domain, the same spatial response plots will be shown for the corresponding orthogonal input case. The orthogonal input case was obtained by shifting the input circumferential position of the ring while maintaining the identical input signal (amplitude and frequency). Referring again to Figs. E.1.4a and E.1.4b, an orthogonal input with respect to the fourth component of the geometric imperfection occurs at a circumferential position of 8.3 degrees. Note that, as would be expected, this position is 22.5 degrees or one-quarter of a wavelength from the affine input to the ring at 30.8 degrees.

The spatial response at the fundamental frequency for the orthogonal case is shown in Fig. 3.3.6. Note again the dominant response characteristic of the fourth wavenumber. The spatial response of the second harmonic of the fundamental input frequency is shown in Fig. 3.3.7. As in the affine case, the dominant wavenumber response is not apparent.

Fig. 3.3.8 is the overlaid spatial response plots at the fundamental 176 Hz frequency for the affine and orthogonal input cases. The response characteristics at the fundamental frequency for the two cases are nearly identical. The Fourier transform of the spatial response data was performed to calculate the wavenumber spectrum for the response data. (Recall that the Fourier transform of time series data produces a frequency spectrum while the Fourier transform of spatial data produces a wavenumber spectrum.) The overlaid wavenumber spectrum of the fundamental frequency response for the affine and orthogonal input conditions is shown in Fig. 3.3.9. As with the spatial response of Fig. 3.3.8, the wavenumber spectrum reveals the identical characteristics of the fundamental frequency response for the affine and orthogonal cases.

Turning to the response of the second harmonic of the fundamental frequency, the overlaid spatial response plots in Fig. 3.3.10 are quite different. Shown in Fig. 3.3.11, the wavenumber spectrums of the affine and orthogonal inputs reveal the differences. As predicted by the analysis, the orthogonal input produces a response that has a minimal fourth wavenumber component. The affine response at the second harmonic frequency reveals that the fourth wavenumber component was excited. Recall that the only difference between the two wavenumber spectra is the input position. Again, the affine input aligns the input frequency with the geometric imperfection so that the imperfection produces a double frequency response at that wavenumber.

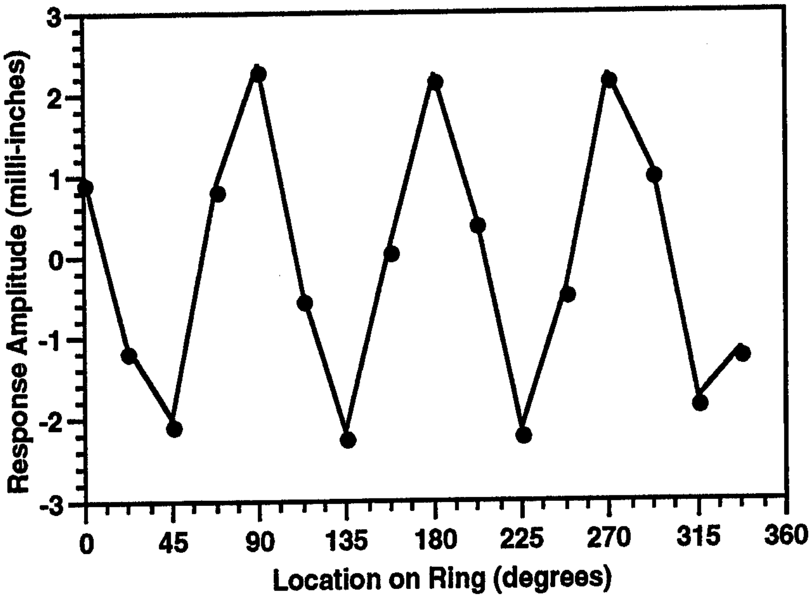

Figure 3.3.6
F_1 Frequency Orthogonal Amplitude Response

0.034 inch ring | F_1 = 178 Hz | θ_{input} = 8.3°

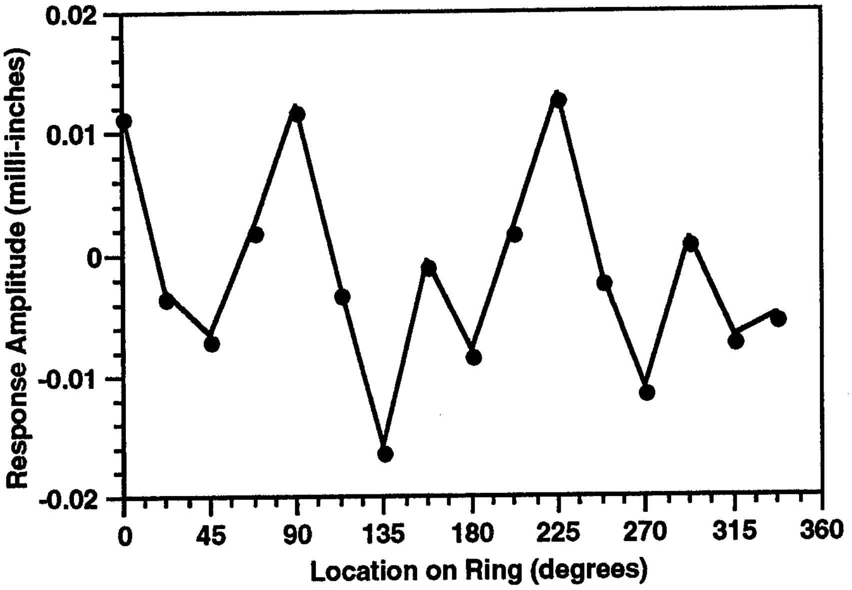

Figure 3.3.7
F_2 Frequency Orthogonal Amplitude Response

0.034 inch ring | F_1 = 176 Hz | F_2 = 352 Hz | θ_{input} = 8.3°

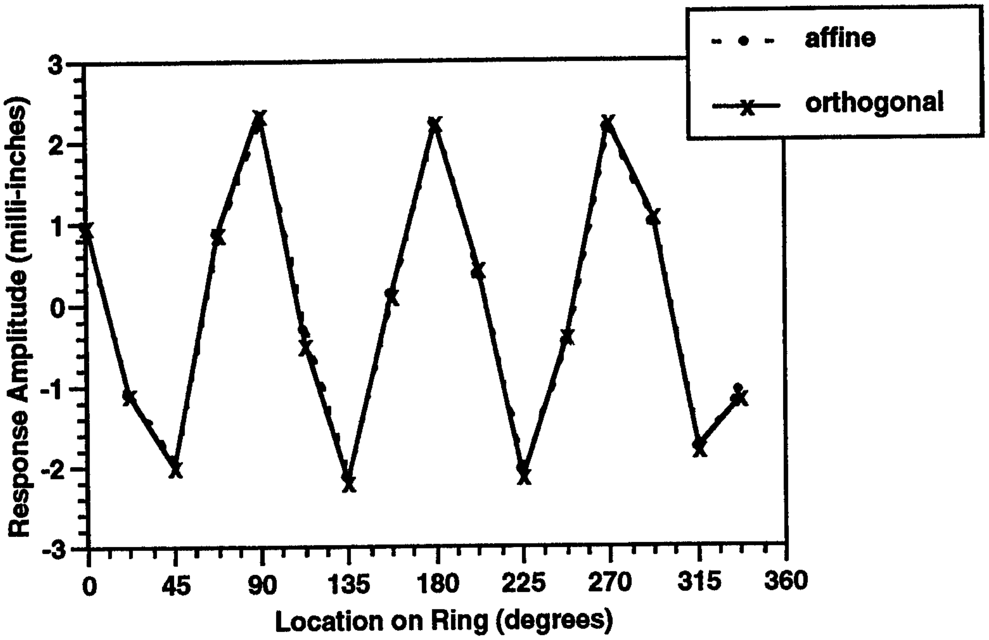

Figure 3.3.8
F_1 Frequency Affine and Orthogonal Amplitude Response

0.034 inch ring | F_1 = 176 Hz | $\theta_{ortho} = 8.3°$ | $\theta_{affine} = 30.8°$

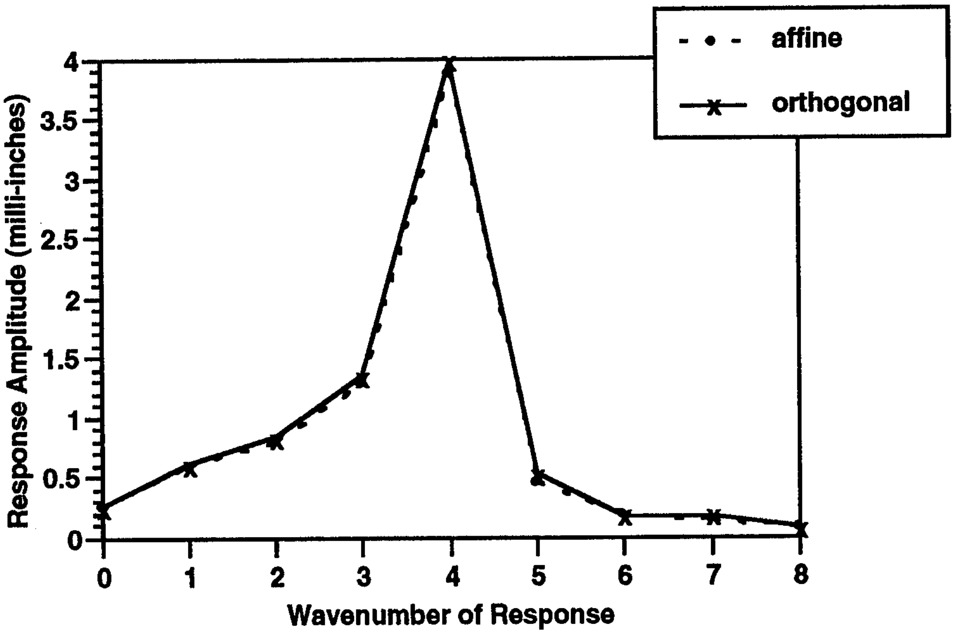

Figure 3.3.9
F_1 Frequency Affine and Orthogonal Wavenumber Spectrum

0.034 inch ring | F_1 = 176 Hz | $\theta_{ortho} = 8.3°$ | $\theta_{affine} = 30.8°$

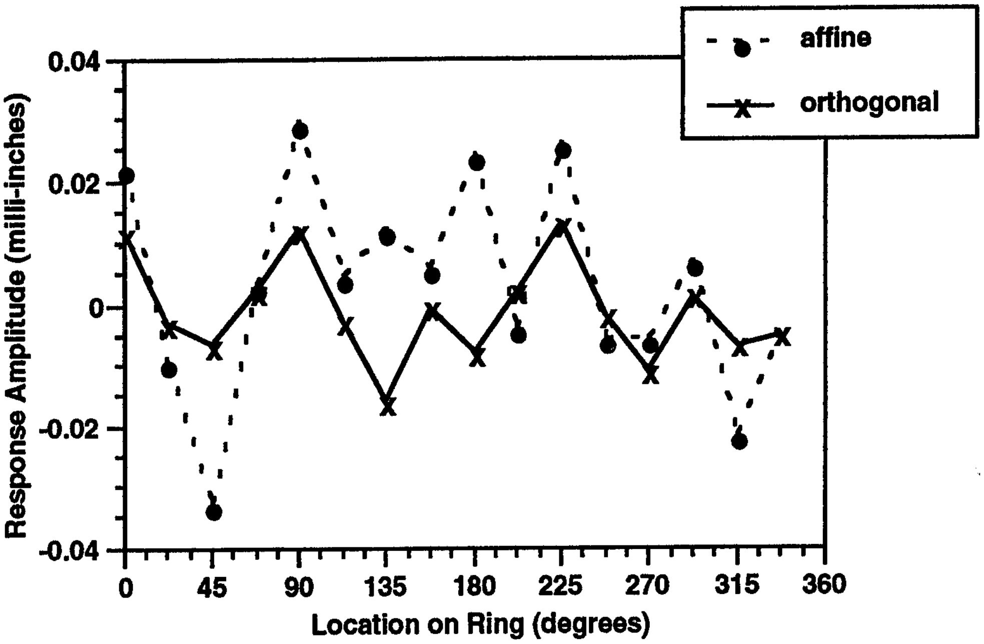

Figure 3.3.10
F_2 Frequency Affine and Orthogonal Amplitude Response

0.034 inch ring | F_2 = 352 Hz | θ_{ortho} = 8.3° | θ_{affine} = 30.8°

AS-94-1159

There is some fifth order component in Fig. 3.3.11, which is the linear response of the double frequency input to the system (see Table 3.3.1). Some double frequency input was allowed into the input signal to the ring so that the double frequency amplitude was above the background noise of the system. Without sufficient double frequency amplitude, it would not have been possible to determine the wavenumber response of the system. This corresponds to a two-mode solution of Section 2 in which two frequencies are input into the system. In this case the second frequency is double the first frequency. With the wavenumber spectrum, the linear response to this double frequency can be distinguished from the nonlinear quadratic response.

Interestingly, the n=1 wavenumber also increases dramatically with the affine input. This could be due to the wavenumber interaction, revealed in the analysis of Section 2, between the n=5 and n=4 double frequency wavenumber response. The difference between the fifth and fourth wavenumber is the n=1 wavenumber. Thus, some evidence for nonlinear wavenumber interactions is present.

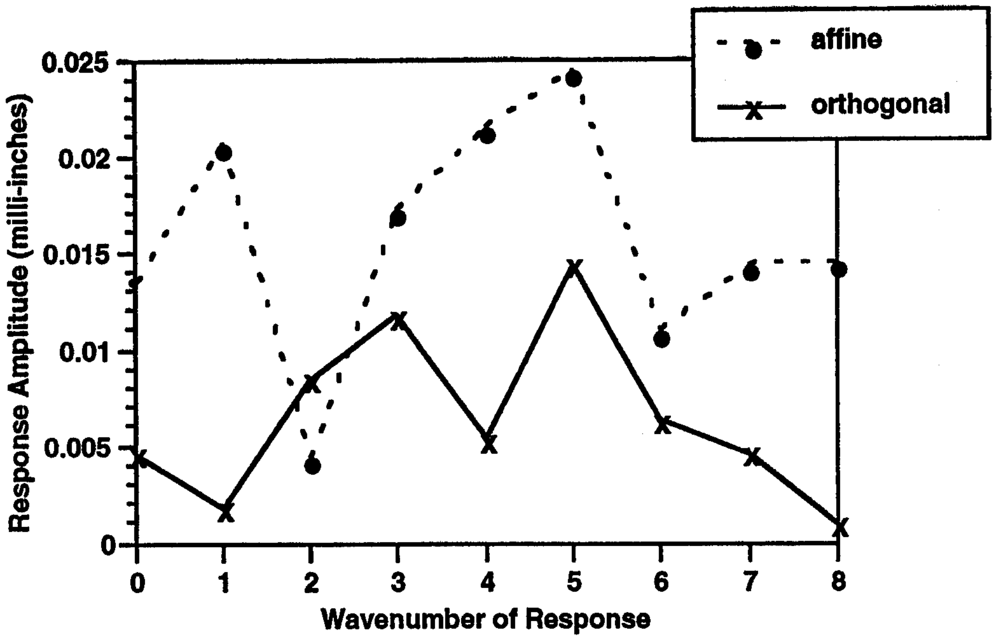

Figure 3.3.11
F_2 Frequency Affine and Orthogonal Wavenumber Spectrum

0.034 inch ring | F_2 = 352 Hz | $\theta_{ortho} = 8.3°$ | $\theta_{affine} = 30.8°$

AS-94-1160

Neither the affine nor orthogonal input conditions produced the level of response of the breathing mode (m=0 wavenumber) predicted for inextensional ring vibrations. The breathing mode response, in fact, should be the dominant response of the double frequency since it is proportional to

$$\frac{m^2}{4}\left(\frac{h}{R}\right)\tilde{A}_m{}^2 \quad , \qquad \text{(see Eq. 3.3.4)}$$

while the geometric imperfection response is proportional to the smaller

$$\frac{m^4}{2}\left(\frac{h}{R}\right)^2 \tilde{\delta}_m \cos\phi_m \left(\frac{\partial \tilde{A}_m}{\partial \tau}\right)^2 \quad . \qquad \text{(see Eq. 3.3.3)}$$

A quick comparison of these values for

$$m{=}4, \frac{h}{R} = \frac{0.034}{4.75} = 0.0072\ , \text{ and } \tilde{\delta}_m = 0.1$$

shows that the breathing mode should respond at an amplitude 44 times greater than that of the geometric imperfection mode. It appears then, that the ring may not be responding inextensionally and that the breathing mode is not excited as expected in the double frequency.

Similar results were obtained for a 199 Hz excitation of the 0.073 inch thick ring. Table 3.3.2 contains the wavenumber and frequency information for this ring. Note that a 199 Hz input frequency excites the third wavenumber and that an input of the second harmonic at 398 Hz will excite the fourth wavenumber. For an affine input, the ring was positioned at 38.7 degrees, and for the orthogonal input, the ring was 30 degrees from that at 8.7 degrees (see Figs. E.2.4a and E.2.4b in Appendix E).

Table 3.3.2
Natural and Response Frequencies of the 0.073 Inch Ring

Wavenumber	Natural Frequency	Response Frequency
2	78.1 Hz	
3	219 Hz	199 Hz
4	414 Hz	398 Hz
5	664 Hz	597 Hz
6	1011 Hz	
7	1328 Hz	
8	1914 Hz	

Figures 3.3.12 and 3.3.13 are the affine amplitude responses at the fundamental and second harmonic frequencies, respectively. Figures 3.3.14 and 3.3.15 are the similar plots except for the orthogonal case. Note that the input frequency response shows the dominant third wavenumber, while the second harmonic frequencies show no apparent dominant wavenumber response as was the case with the 0.034 inch thick ring.

The overlaid amplitude responses for the affine and orthogonal cases at the input frequency, f_1, appear very similar (see Fig. 3.3.16) as do the wavenumber spectrum for the two input cases (Fig. 3.3.17). The second harmonic response, f_2, for the affine and orthogonal cases are very dissimilar in the amplitude response as shown in the overlaid plots in Fig. 3.3.18. This is confirmed in the wavenumber spectrum of the two inputs as shown in Fig. 3.3.19.

Examining the wavenumber response at the double frequency, it is again apparent that the affine input increases the double frequency response at the input wavenumber, in this case the n=3 wavenumber. The wavenumber response of the input n=3 wavenumber is increased by almost a factor of 2 by the affine input location. This increase is less than that seen for the 0.034 inch ring case, which was more than 4.5 times with the affine input. This decrease in geometric imperfection effect can be attributed to the smaller imperfection to thickness ratio (δ_m) and the smaller thickness to ring radius ratio $\left(\frac{h}{R}\right)$ since the imperfection wavenumber response is proportional to both of these (see Eq. 3.3.3).

In contrast to the 0.034 inch ring wavenumber response results, it is not clear in this case that there are nonlinear wavenumber interactions at the f_2 frequency. However, the rigid body motion of the first wavenumber is again excited with the affine input. As with the 0.034 inch ring, the breathing mode response at the double frequency is not readily apparent.

Thus, from the data for the 0.034 inch ring and the 0.073 inch ring, it is shown that the geometric imperfections create the double frequency flexural mode response at the wavenumber linearly excited by the input frequency. This was confirmed by comparison of the affine and orthogonal input locations to the circular ring. The predicted double frequency breathing mode, however, is not apparent and, thus, the inextensional response of the circular ring is brought into question. There is some evidence that the rigid body mode is excited and amplified with the affine input.

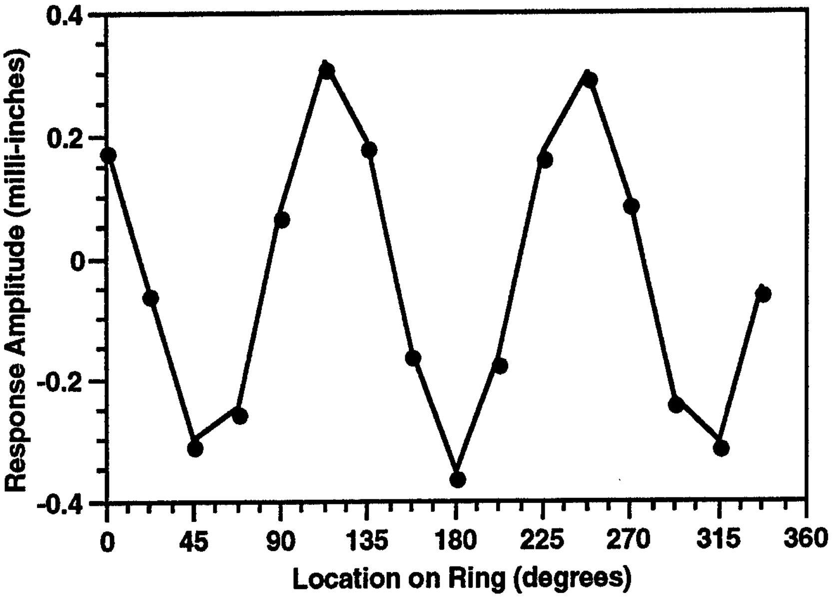

Figure 3.3.12
F1 Frequency Affine Amplitude Response

0.073 inch ring I F_1 = 199 Hz I θ_{input} = 38.7°

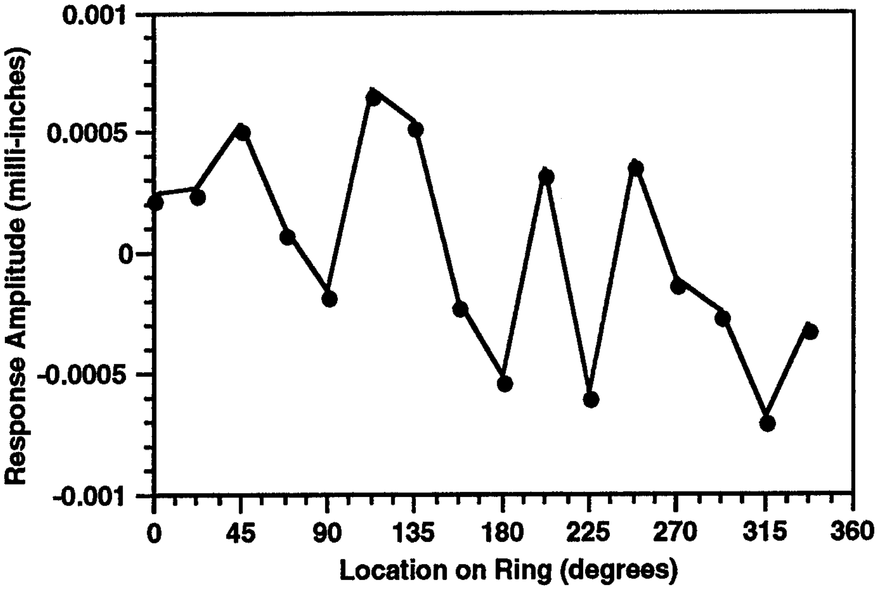

Figure 3.3.13
F2 Frequency Affine Amplitude Response

0.073 inch ring I F_1 = 199 Hz I F_2 = 398 Hz I θ_{input} = 38.7°

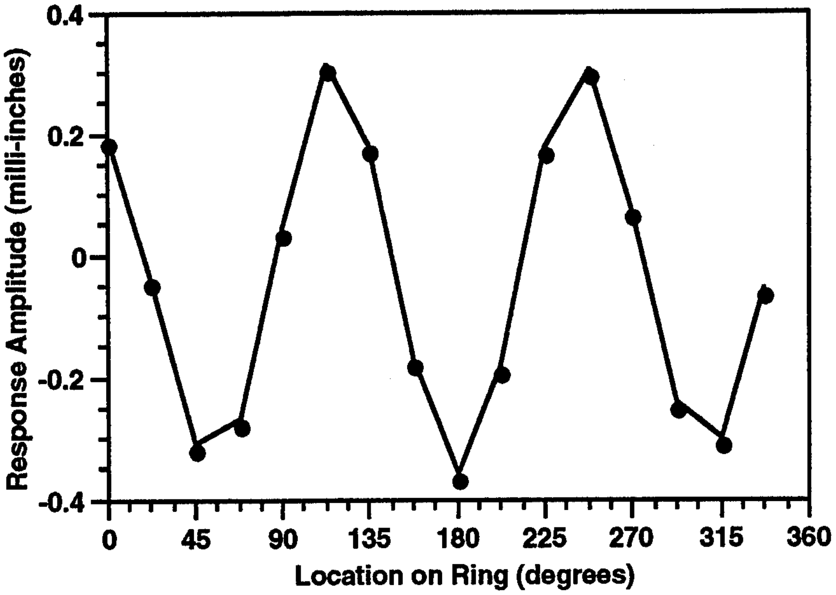

Figure 3.3.14
F_1 Frequency Orthogonal Amplitude Response

0.073 inch ring I F_1 = 198 Hz I θ_{input} = 8.7°

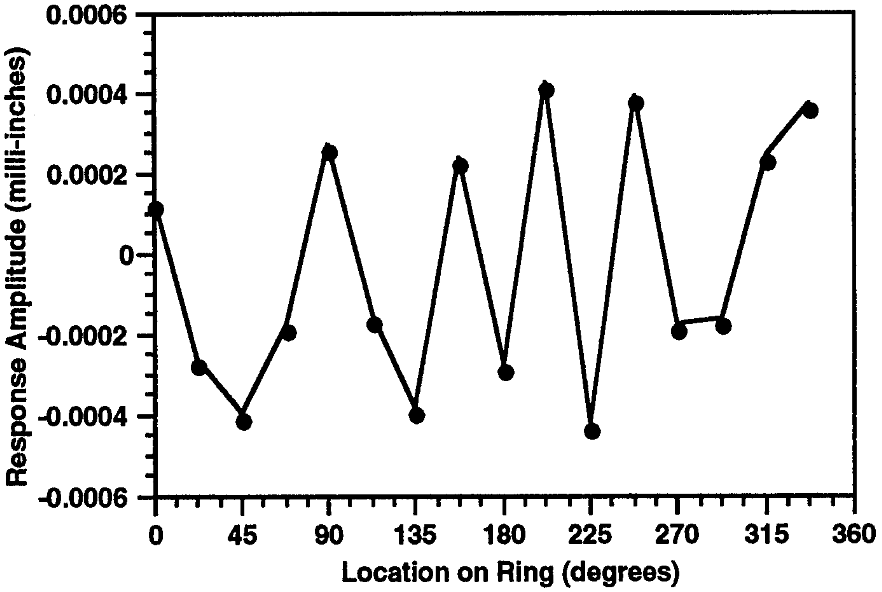

Figure 3.3.15
F_2 Frequency Orthogonal Amplitude Response

0.073 inch ring I F_1 = 199 Hz I F_2 = 398 Hz I θ_{input} = 8.7°

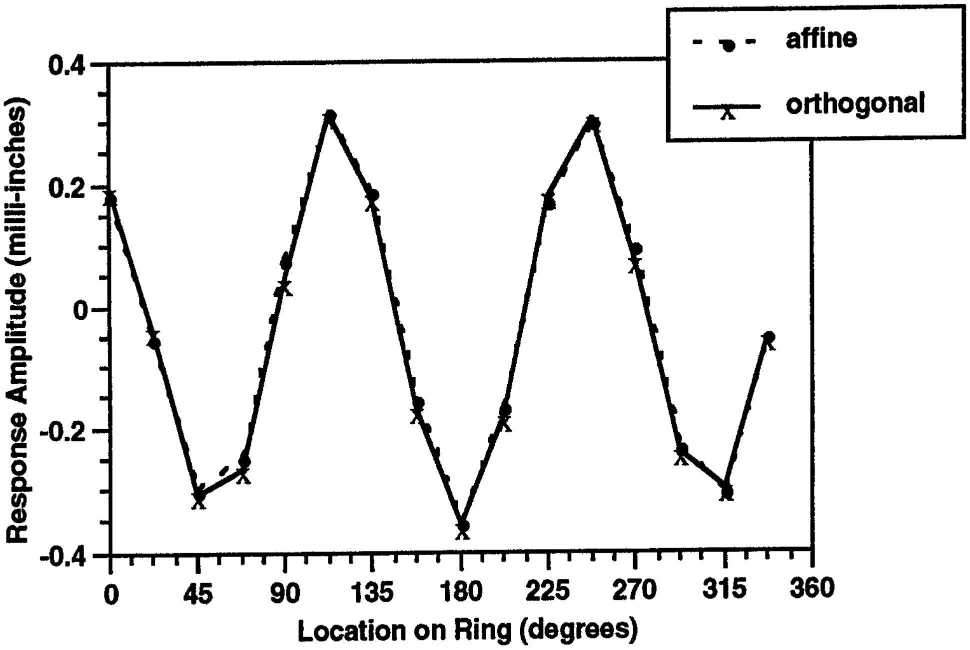

Figure 3.3.16
F1 Frequency Affine and Orthogonal Amplitude Response

0.073 inch ring | F_1 = 199 Hz | $\theta_{ortho} = 8.7°$ | $\theta_{affine} = 38.7°$

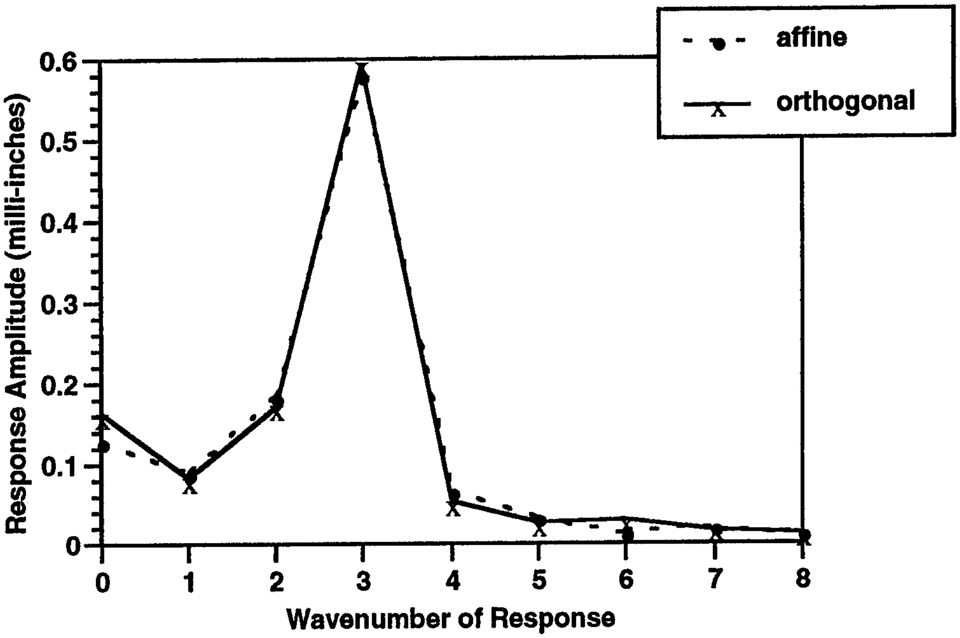

Figure 3.3.17
F1 Frequency Affine and Orthogonal Wavenumber Spectrum

0.073 inch ring | F_1 = 199 Hz | $\theta_{ortho} = 8.7°$ | $\theta_{affine} = 38.7°$

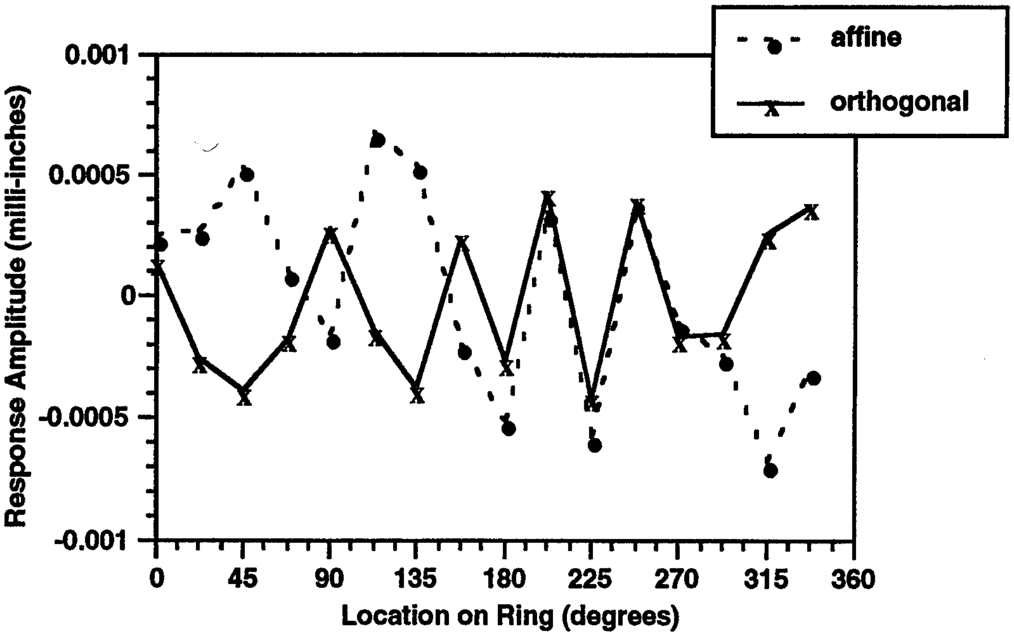

Figure 3.3.18
F2 Frequency Affine and Orthogonal Amplitude Response

0.073 inch ring | F_2 = 398 Hz | $\theta_{ortho} = 8.7°$ | $\theta_{affine} = 38.7°$

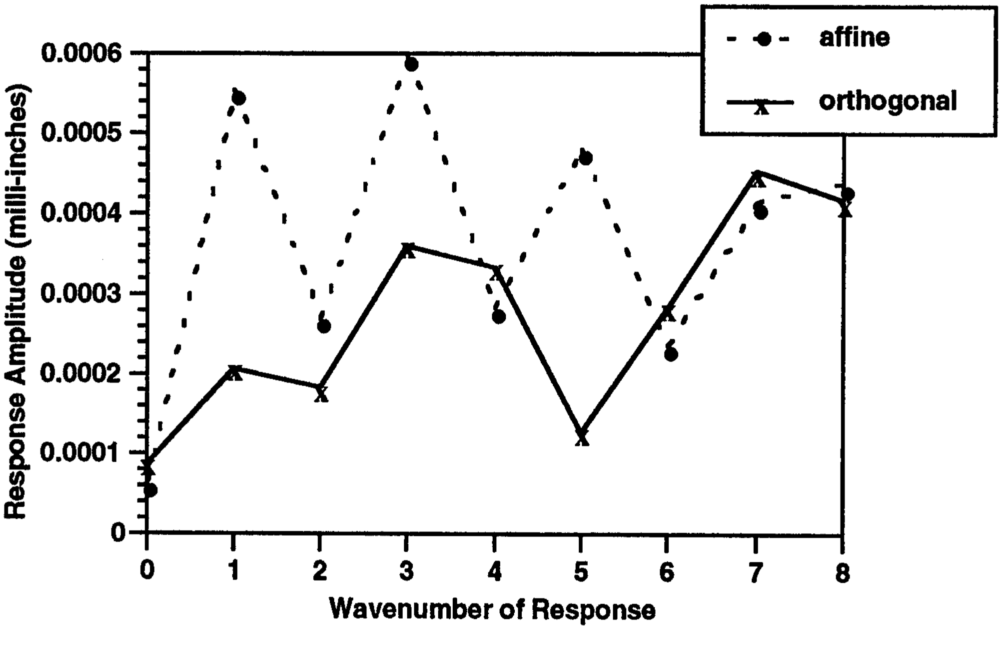

Figure 3.3.19
F2 Frequency Affine and Orthogonal Wavenumber Spectrum

0.073 inch ring | F_2 = 398 Hz | $\theta_{ortho} = 8.7°$ | $\theta_{affine} = 38.7°$

This page intentionally left blank.

SECTION 4
CONCLUSIONS AND FINAL DISCUSSIONS

4.1 CONCLUSIONS

From the investigation of circular rings presented here, a number of interesting conclusions can be made as drawn from three major sections of this thesis, the analytical investigation, the experimental higher order investigation, and the geometric imperfection study. These will be addressed in turn.

First, the analytical work of Section 2 revealed that the inextensional assumption of the ring vibration produced a nonlinearly generated double frequency breathing mode response. In addition, geometric imperfections can also produce a double frequency response. However, this is dependent on the relative position between the input force and geometric imperfection waveform, as well as the frequency of the excitation. Also, some evidence for the possibility of nonlinear wavenumber interactions was present in the analytical forms of the response equations.

Second, the higher order spectral investigation has shown some of the utility of this signal processing tool. The bicoherence, in particular, is capable of revealing quadratic interactions in the response that are not readily apparent in the power spectrum of the response. The occurrence of a significant bicoherence response between the spectral line frequencies of the ring response confirms the existence of a quadratic nonlinear response in the structure.

Third, the circular ring has proven to be an excellent structure for the investigation of the effect of geometric imperfections on the wave response of structures. As shown in Section 3, the geometric imperfections can produce a double frequency flexural response as predicted by the analysis. This double frequency response does not occur with the orthogonal forcing function input where the geometric imperfection is oriented orthogonally to the input spatial location. However, when the input is spatially affine or in phase with the geometric imperfection, the wavenumber of the fundamental response is significantly increased in the double frequency response.

The other predicted double frequency response, the breathing mode, did not occur at higher magnitude levels with respect to the geometric imperfection response. Some question then presents itself as to the validity of the inextensional assumption that gave rise to the breathing mode response in the analysis. Finally, some experimental evidence was obtained for the presence of nonlinear wavenumber interactions.

4.2 UNANSWERED QUESTIONS AND FUTURE WORK

The effects of nonlinearities on system response and the identification of those nonlinearities is an important structural dynamics problem. The circular ring has proven to be a useful structure, which is simple enough in its geometry to be investigated analytically and experimentally yet provides an avenue to allow the study of system nonlinearities. Many interesting features of the nonlinear ring problem have been investigated here, but many more questions remain. Fortunately, higher order signal processing provides an additional tool with which to study circular ring and other structures exhibiting nonlinearities.

The affine input to the geometrically imperfect ring seems to amplify the rigid body mode. The acoustic radiation from this rigid body mode would be in the form of a dipole. The dipole is an efficient radiator, though not as efficient as the monopole of the breathing mode, and would be significant in the acoustic response of the circular ring.

Some areas that remain to be investigated include

- the influence of radial preloading on the nonlinear response of a structure
- the nonlinear response of combination shell and ring structures common in aerospace and naval structures
- the acoustic radiation of nonlinearly excited structures, both in terms of near field and far field effects
- the transient response of nonlinear structures and the usefulness of higher order signal processing for the non-steady state problem
- a final survey of the existence of the breathing mode phenomenon.

The question of the inextensional versus extensional vibration for structural bodies of revolution that have a closure compatibility condition is still not completely settled. The generation of breathing modes in bodies of revolution is an important phenomenon and a phenomenon that has not been entirely established as existing. The acoustic radiation of a body vibrating in a breathing mode can be quite significant since the structure is acting as an efficient monopole source.

Some of these questions may be resolved with a more complete analytical analysis of the structural input to the ring. With a singular point input (a delta function), the continuity condition in shear force is not necessarily accurate. If the ring could be excited in a truly spatial fashion, the breathing mode phenomenon may be more present since the boundary conditions would be more precise, that is, there would be no discontinuity in shear. This type of loading may be most conveniently applied and most applicable to the acoustic radiation question if a ring or cylindrical shell were excited by (underwater) acoustic waves.

In conclusion, the most important finding of this report is the experimental evidence for the geometric imperfection effect at the double frequency. Since geometric imperfections are ubiquitous, their effects in terms of nonlinear responses is significant. The rings used in this study were manufactured without the intention of creating geometric imperfections. The imperfections were indeed small and yet the results were still noticeable. In addition, the input amplitudes were small in nature and the input frequencies were not near natural resonances of the circular rings. Thus, the results are general in nature.

This page intentionally left blank.

APPENDIX A
NONLINEAR STRAIN DISPLACEMENT RELATIONS

This appendix will be devoted to the nonlinear strain-displacement relation for the longitudinal circumferential strain term ε_{yy} since this is the most important (and indeed the only) strain term in the development of the transverse vibrations of circular rings. The strain-displacement in cylindrical coordinates accurate to second-order has been developed by Novozhilov (Ref. 40, p. 192) and will be simply repeated here but in the notation of this paper:

$$\varepsilon_{yy} = \left(\frac{1}{1+z/R}\right)\left(\frac{\partial v'}{\partial y} + \frac{w'}{R}\right) + \frac{1}{2(1+z/R)^2}\left[\left(\frac{\partial v'}{\partial y} + \frac{w'}{R}\right)^2 + \left(\frac{\partial w'}{\partial y} - \frac{v'}{R}\right)^2\right] \quad . \tag{A.1}$$

The primes of v and w indicate that these displacements are general and not necessarily those of the mid-plane surface of the ring.

Geometric imperfections can now be included in the strain-displacement expressions. The geometric imperfections will be assumed to exist in a residual strain-free condition, which can be expressed as

$$\varepsilon_{yy} = \varepsilon_{yy}(v', w' + \bar{w}) - \varepsilon_{yy}(0, \bar{w}) \quad , \tag{A.2}$$

where $\bar{w}$ is the geometric imperfection static displacement. The geometric imperfections will be assumed to be on the order of, or less than, the radial displacement, $O[\bar{w}] \leq O[w]$. Expanded, using Eq. A.1, the nonlinear strain-displacement relation with geometric imperfections becomes

$$\varepsilon_{yy} = \left(\frac{1}{1+z/R}\right)\left(\frac{\partial v'}{\partial y} + \frac{w'}{R}\right) + \frac{1}{2(1+z/R)^2}\left[\left(\frac{\partial v'}{\partial y} + \frac{w'}{R}\right)^2 + \left(\frac{\partial w'}{\partial y} - \frac{v'}{R}\right)^2 + 2\left(\frac{\partial v'}{\partial y} + \frac{w'}{R}\right)\frac{\overline{w}}{R} + 2\left(\frac{\partial w'}{\partial y} - \frac{v'}{R}\right)\frac{\partial \overline{w}}{\partial y}\right] \quad . \tag{A.3}$$

This expression (Eq. A.3) is accurate to second order.

It is now necessary to relate the displacements v'(y,z,t) and w'(y,z,t) to displacements of the mid-surface of the ring. As required by Kirchoff's hypothesis that normals to the undeformed middle surface remain straight and normal to the deformed middle surface and undergo no extension, the tangential and radial displacements are approximated by the following linear relationships (Ref. 39, p. 6-7):

$$v'(y,z,t) = v(y,t) + z\,\theta(y,t) \tag{A. 4a}$$

$$w'(y,z,t) = w(y,t) \quad , \tag{A.4b}$$

where θ is the rotation of the normal to the middle surface during deformation as shown in Fig. A.1.

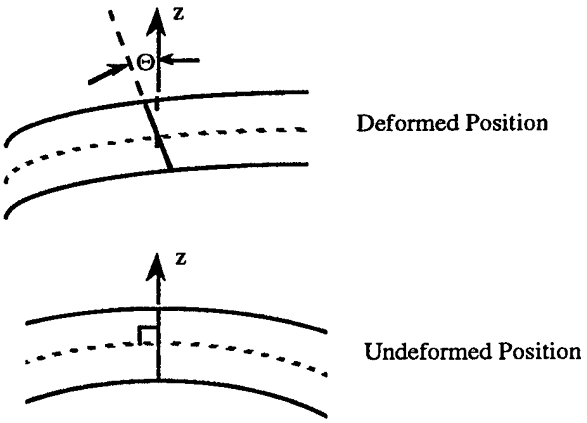

Figure A.1
Definition of Angle Θ for Deformation of Ring

AS-94-1165

The angle θ can be determined by examining the shear strain:

$$\varepsilon_{yz} = \frac{\partial v'}{\partial z} + \left(\frac{1}{1+z/R}\right)\left[\left(\frac{\partial v'}{\partial y} + \frac{w'}{R}\right)\frac{\partial v'}{\partial z} + \left(\frac{\partial w'}{\partial y} - \frac{v'}{R}\right)\left(1 + \frac{\partial w'}{\partial z}\right)\right] \quad . \tag{A.5}$$

Kirchoff's hypothesis requires that $\varepsilon_{yz} = 0$. By substituting Eq. A.4 with Eq. A.5 and solving the z^0 power resulting equation, θ can be determined as

$$\theta = -\left(\frac{\partial w}{\partial y} - \frac{v}{R}\right)\left[1 - \left(\frac{\partial v}{\partial y} + \frac{w}{R}\right)\right] \approx -\left(\frac{\partial w}{\partial y} - \frac{v}{R}\right) \quad . \tag{A.6}$$

The angle θ enters into the strain-displacement relation at the second-order level; thus it is sufficient to linearize this equation as shown.

Thus, the strain-displacement relation to second order for any point on the ring becomes

$$\varepsilon_{yy} = \frac{1}{1+z/R}\left[\frac{\partial v}{\partial y} + \frac{w}{R} - \frac{z}{R}\left(R\frac{\partial^2 w}{\partial y^2} - \frac{\partial v}{\partial y}\right)\right] + \frac{1}{2(1+z/R)^2}\left[\left(\frac{\partial v}{\partial y} + \frac{w}{R}\right)^2 + \right.$$
$$\left.\left(\frac{\partial w}{\partial y} - \frac{v}{R}\right)^2 + 2\left(\frac{\partial v}{\partial y} + \frac{w}{R}\right)\frac{\bar{w}}{R} + 2\left(\frac{\partial w}{\partial y} - \frac{v}{R}\right)\frac{\partial \bar{w}}{\partial y}\right] \quad . \tag{A.7}$$

This expression for the strain-displacement relationship can be simplified through the application of some relative magnitude assumptions. First, the ring is considered thin so that $\frac{h}{R} << 1$ and thus $\frac{z}{R} << 1$ as well. Second, due to the assumption of small tangential and radial displacements, the expression can be simplified by

$$\frac{\partial v}{\partial y} >> \frac{1}{2}\left(\frac{\partial v}{\partial y}\right)^2 \quad \text{and} \quad \frac{w}{R} >> \frac{1}{2}\left(\frac{w}{R}\right)^2 \quad . \tag{A.8a,b}$$

For inextensional vibrations, the tangential displacements will be less than the radial displacements (see note A.1 below) thus similar to Eq. A.8b:

$$\frac{w}{R} >> \frac{1}{2}\left(\frac{v}{R}\right)^2 \quad . \tag{A.8c}$$

Since the geometric imperfections will be small, it is necessary to retain only the largest term containing $\bar{w}$. The criteria used are that $w > v$ and $\frac{\partial \bar{w}}{\partial y} > \frac{\bar{w}}{R}$ (see note A.2 below). Expanding Eq. A.7 with the application of these assumptions yields

$$\varepsilon_{yy} = \frac{\partial v}{\partial y} + \frac{w}{R} - \frac{z}{R}\left(R\frac{\partial^2 w}{\partial y^2} - \frac{\partial v}{\partial y}\right) + \frac{\partial v}{\partial y}\frac{w}{R} + \frac{\partial w}{\partial y}\frac{v}{R} + \frac{1}{2}\left(\frac{\partial w}{\partial y}\right)^2 + \frac{\partial w}{\partial y}\frac{\partial \bar{w}}{\partial y} \quad . \tag{A.9}$$

The arguments of small radial displacements and tangential displacements smaller than radial displacements indicate that $\frac{1}{2}\left(\frac{\partial w}{\partial y}\right)^2 > \frac{\partial v}{\partial y}\frac{w}{R}$ and similarly $\frac{1}{2}\left(\frac{\partial w}{\partial y}\right)^2 > \frac{\partial w}{\partial y}\frac{v}{R}$. Thus, the simplest first-order nonlinear strain-displacement relation with geometric imperfections is

$$\varepsilon_{yy} = \frac{\partial v}{\partial y} + \frac{w}{R} - \frac{z}{R}\left(R\frac{\partial^2 w}{\partial y^2} - \frac{\partial v}{\partial y}\right) + \frac{1}{2}\left(\frac{\partial w}{\partial y}\right)^2 + \frac{\partial w}{\partial y}\frac{\partial \bar{w}}{\partial y} \quad . \tag{A.10}$$

This form of the strain-displacement relation exhibits the basic properties of the breathing mode for inextensional vibrations and the quadratic effects of geometric imperfections, as shown in Section 2.

Note A.1: Relative magnitudes of v and w (Ref. 15, p. 459).

Examine the linear strain-displacement relation for ε_{yy}. If the vibrations are inextensional, this relation is set to zero:

$$\varepsilon_{yy} = \frac{\partial v}{\partial y} + \frac{w}{R} = 0 \quad .$$

If a single mode of flexural vibration for w is assumed to be

$$w = A_n(t)\cos\left(\frac{ny}{R}\right)$$

then

$$\frac{\partial v}{\partial y} = -\frac{w}{R} = -\frac{A_n(t)}{R}\cos\left(\frac{ny}{R}\right) \quad .$$

Solving for v by integration yields

$$v = -\frac{A_n(t)}{n}\sin\left(\frac{ny}{R}\right) \quad .$$

Thus, in the linear limit, w is larger in magnitude than v by a factor of the circumferential wavenumber n. It is the assumption that all tangential displacements and their derivatives may be neglected in the presence of radial displacements that impose the requirement that the circumferential wavenumber must be large.

Note A.2: Relative magnitudes of $\frac{\bar{w}}{R}$ and $\frac{\partial \bar{w}}{\partial y}$.

Examine a single component of a spatial Fourier series expansion of the geometric imperfections, which can be written as

$$\bar{w} = B_n \cos\left(\frac{ny}{R}\right) \quad .$$

The derivative of this with respect to y is

$$\frac{\partial \bar{w}}{\partial y} = -\frac{nB_n}{R}\sin\left(\frac{ny}{R}\right) \quad .$$

Thus, it can be seen that $\frac{\partial \bar{w}}{\partial y}$ is larger than $\frac{\bar{w}}{R}$ by a factor of the circumferential wavenumber n.

This page intentionally left blank.

APPENDIX B

CIRCULAR RING VIBRATION MODE DESCRIPTIONS

This appendix is devoted to the description of the various mode shapes of the transverse vibrations of circular rings. The radial displacement is approximated by a Fourier series expansion as

$$w(y,t) = \sum_{n=0}^{\infty} \left[A_n(t) \cos\left(\frac{ny}{R}\right) + B_n(t) \sin\left(\frac{ny}{R}\right) \right] \quad , \tag{B.1}$$

where $A_n(t)$ and $B_n(t)$ are dynamic amplitude terms and n corresponds to the circumferential wavenumber. This expression can be divided into three parts representing three types of displacement:

$$w(y,t) = [A_0(t)] + \left[A_1(t) \cos\left(\frac{y}{R}\right) + B_1(t) \sin\left(\frac{y}{R}\right) \right] + \sum_{n=2}^{\infty} \left[A_n(t) \cos\left(\frac{ny}{R}\right) + B_n(t) \sin\left(\frac{ny}{R}\right) \right] \quad . \tag{B.2}$$

The first square bracket term is for n=0 and corresponds to a breathing mode with amplitude $A_0(t)$. This type of vibration is shown in Fig. B.1. The second square bracket term is for n=1 and corresponds to a rigid body motion. This is shown in Fig. B.2. The third square bracket represents the flexural modes.

The first flexural mode (see Figs. 3a–d) is for n=2, and thus this mode is considered the fundamental mode of vibration (not the n=0 breathing mode). The modes for n>2 are spatial harmonics of the fundamental mode. The convention used here is that n=3 will be labeled the second harmonic (the fundamental n=2 mode considered the first harmonic), n=4 the third harmonic, etc. Two notes are important:

- The harmonic name, as indicated, does <u>not</u> correspond to the circumferential wavenumber directly but to the (n+1) wavenumber. Table B.1 must be kept in mind when analyzing and discussing circular ring vibrations.

Table B.1
Description of Circular Ring Modes

Wavenumber (n)	Type of Mode	Name of Mode
0	Breathing	Breathing Mode
1	Rigid Body	Rigid Body Mode
2	Flexural	Fundamental
3	Flexural	Second Harmonic
4	Flexural	Third Harmonic
5	Flexural	Fourth Harmonic
$n \geq 6$	Flexural	$(n-1)^{th}$ Harmonic

- The discussion of mode harmonics refers only to spatial harmonics. There is no reference whatsoever to frequency harmonics. It is not necessary that higher circumferential modes of vibration correspond to higher frequencies of vibration. A simple example is that the natural frequency of vibration of the breathing mode (n=0) is generally higher than that of the fundamental mode (n=2). As shown in the main text, a single temporal frequency can contain components of more than one spatial wavenumber response.

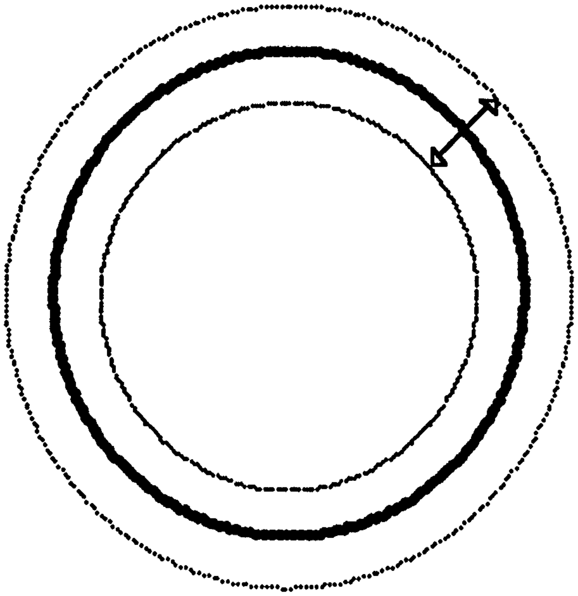

Figure B.1
Breathing Mode (n = 0)

AS-94-1166

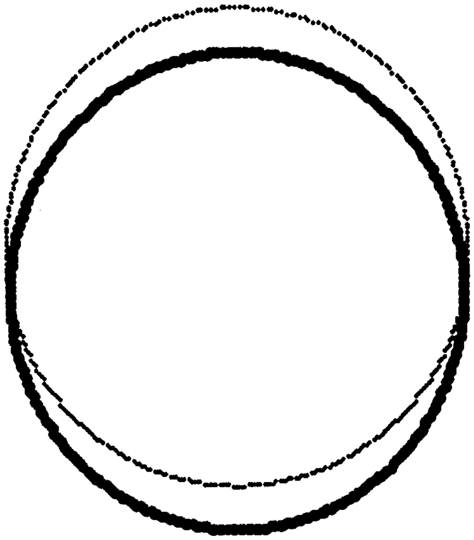

Figure B.2
Rigid Body Mode (n = 1)

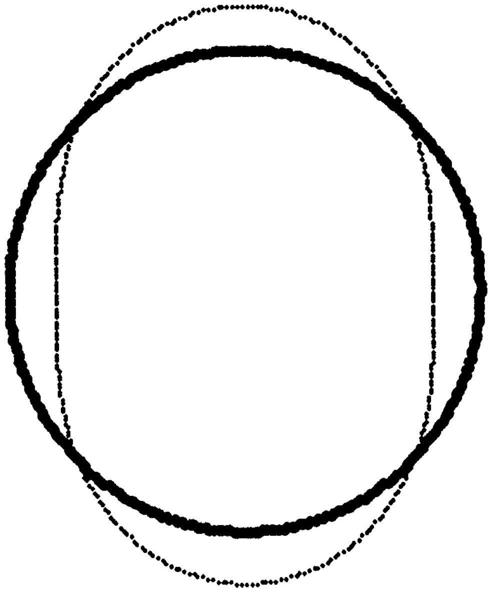

Figure B.3a
Fundamental Flexural Mode (n = 2)

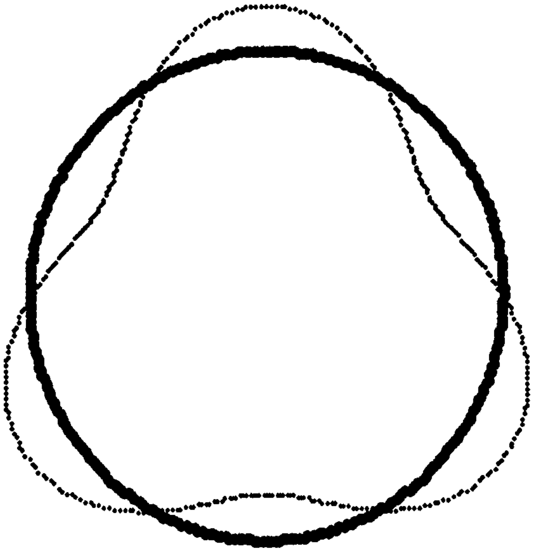

Figure B.3b
Second Harmonic Flexural Mode (n = 3)

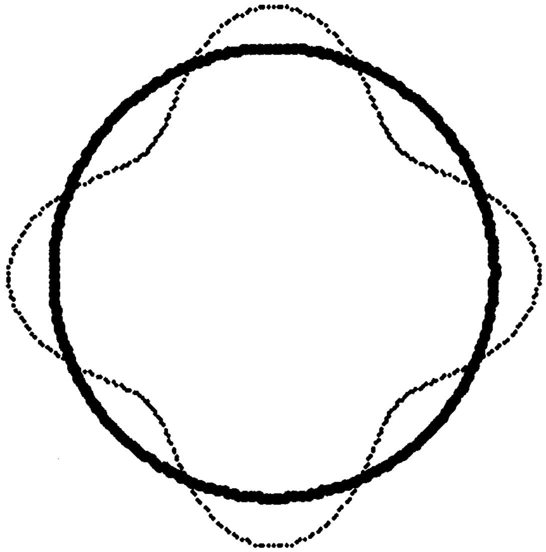

Figure B.3c
Third Harmonic Flexural Mode (n = 4)

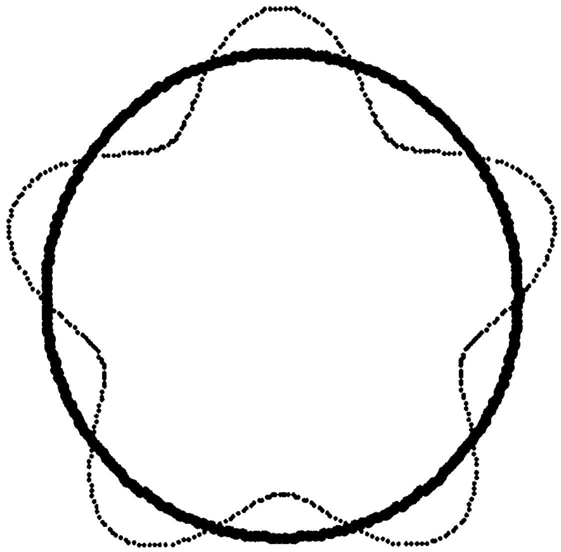

Figure B.3d
Fourth Harmonic Flexural Mode (n = 5)

AS-94-1169

This page intentionally left blank.

APPENDIX C

PROXIMETER PROBE CALIBRATION CURVES

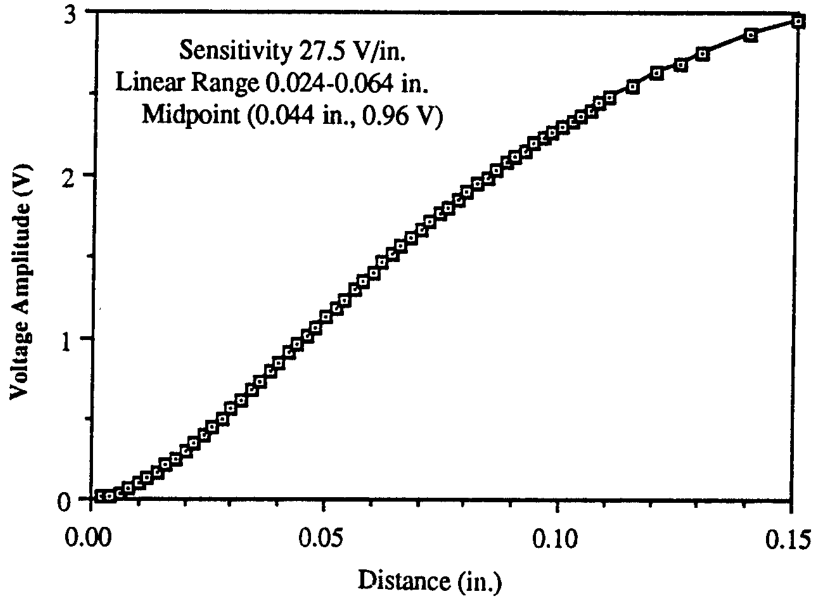

Figure C.1
External Proximeter Probe Calibration Data

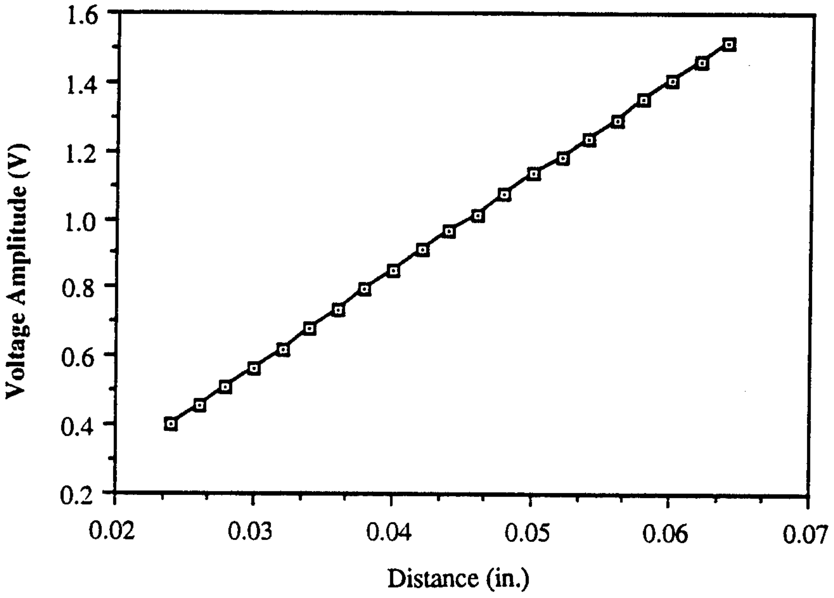

Figure C.2
Linear Range of External Proximeter Probe

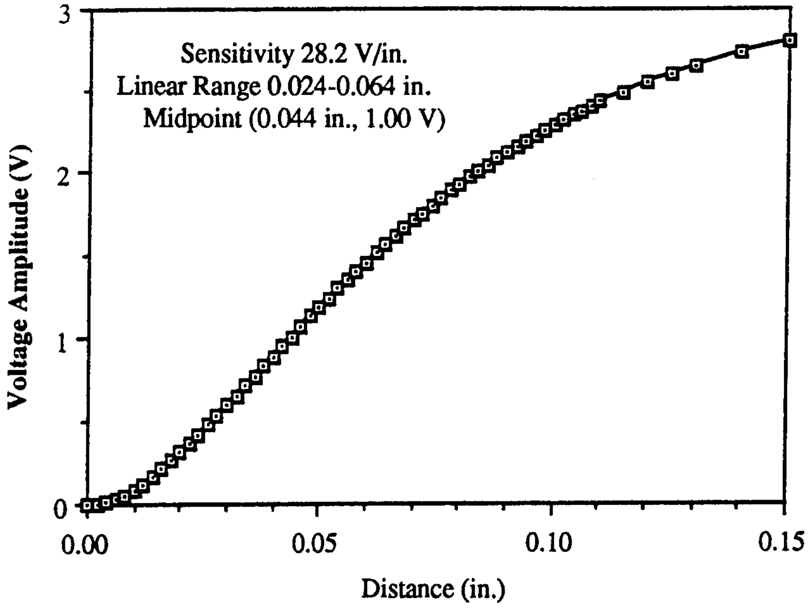

Figure C.3
Fixed Proximeter Probe Calibration Data

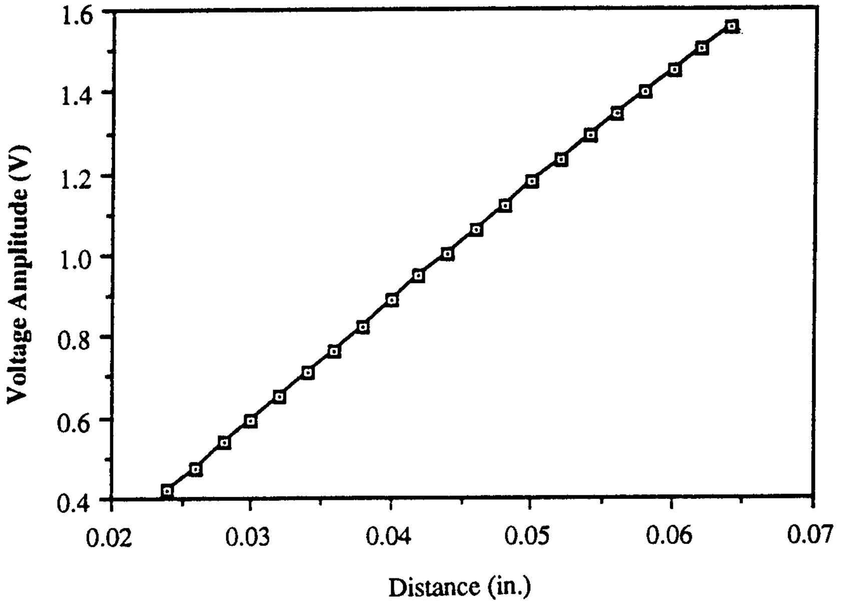

Figure C.4
Linear Range of Fixed Proximeter Probe

APPENDIX D
CIRCULAR RING NATURAL FREQUENCIES

This appendix presents the experimentally determined natural frequencies for four circular rings. The natural frequencies were measured using the described experimental setup except that the input to the rings was an impact from a metal hammer. The impact excites all of the natural frequencies which are detected from their increased power spectral response amplitudes. Accuracy is predicted to be within 2%.

Table D.1
Natural Frequencies of Rings

Wavenumber n	Frequency 0.034 Ring	Frequency 0.073 Ring	Frequency 0.102 Ring	Frequency 0.275 Ring
0				7030 Hz
2	31.3 Hz	78.1 Hz	117.2 Hz	312.5
3	93.8	218.8	312.5	898.4
4	187.5	414.1	625.0	1758
5	312.5	664.1	976.6	2812
6	468.8	1012	1445	4062
7	640.6	1328	1992	5585
8	843.8	1914	2617	7305
9	1062.5	2422	3359	9219
10	1328	2969	4101	11330
11	1609	3594	5000	13590
12	1922	4258	5977	
13	2250	5039		
14	2625	5859		
15	3016			
16	3438			
17	3875			

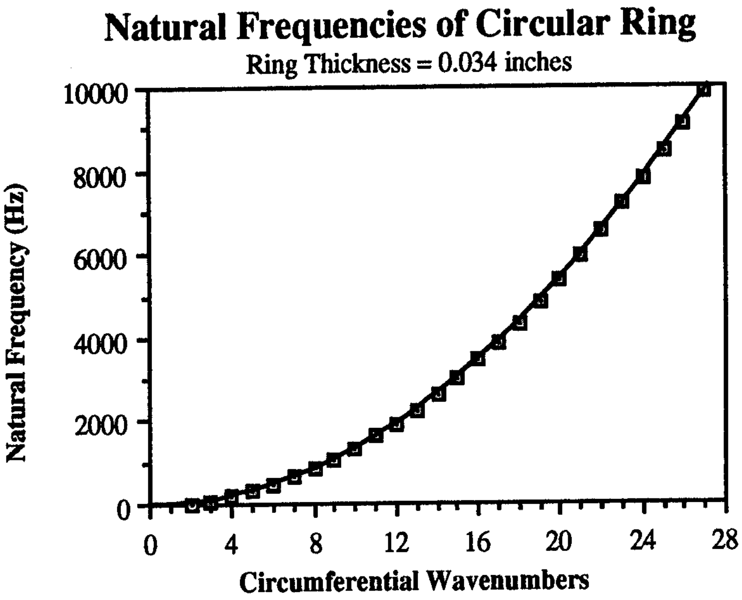

Figure D.1
0.034 Inch Thick Ring Natural Frequencies

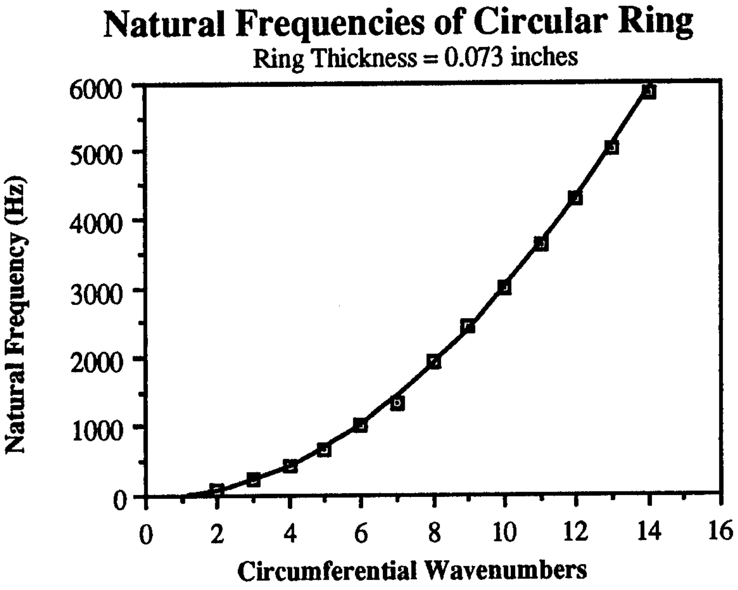

Figure D.2
0.073 Inch Thick Ring Natural Frequencies

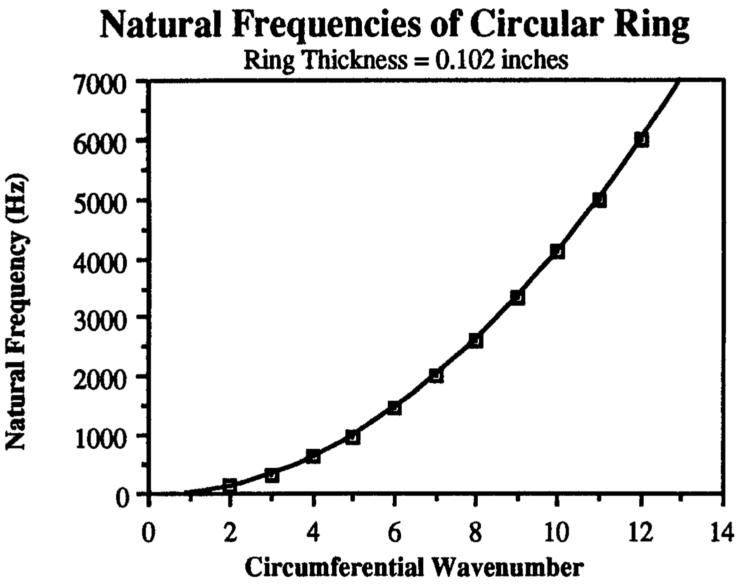

Figure D.3
0.102 Inch Thick Ring Natural Frequencies

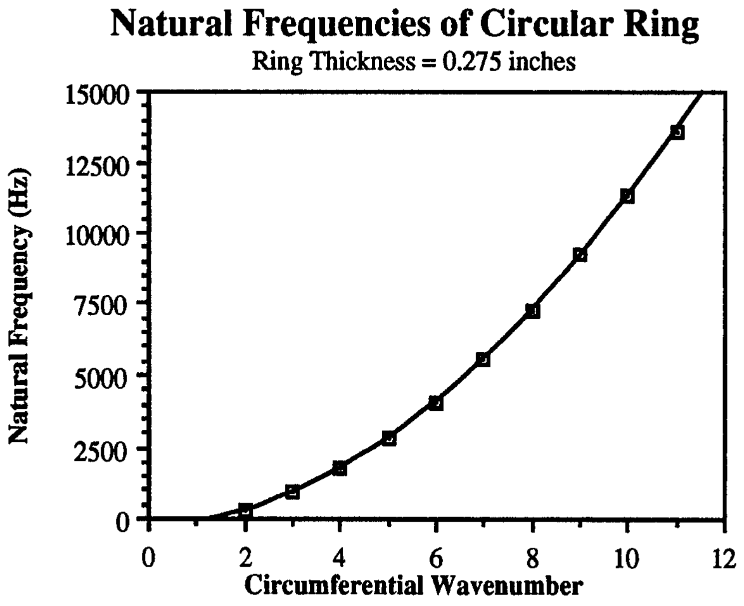

Figure D.4
0.275 Inch Thick Ring Natural Frequencies

This page intentionally left blank.

APPENDIX E

CIRCULAR RING GEOMETRIC IMPERFECTION MEASUREMENTS

This appendix presents the measured geometric imperfections of three thin circular rings. The imperfections were determined from a minimum of two averages of the static displacement of both the interior and exterior surfaces of the ring. The rigid body and mean value components of the measurements are removed since they do not contribute to the static geometric imperfections.

The interior and exterior imperfection shapes are shown in Figs. 1.1a and 1.1b, 2.1a and 2.1b, and 3.1a and 3.1b, respectively. Note that for all three ring thicknesses, the variation across the ring thickness as determined by comparing the interior and exterior measurements is not significant and thus the imperfection shapes are nearly identical for both the interior and exterior surfaces. Thus, the imperfection can be developed as a simplified function of the circumferential coordinate, y, only.

Taking the Fourier series of the imperfection waveshape of the interior and exterior surfaces yields the wavenumber component amplitudes of the geometric imperfection shapes. These component amplitudes for the three rings interior and exterior surfaces are shown in Figs. 1.2a and 1.2b, 2.2a and 2.2b, and 3.2a and 3.2b, respectively. Note again that the wavenumber amplitudes reveals the similarity between the interior and exterior imperfection shapes. Also, the majority of the imperfection waveshape for all three rings is made up of wavenumbers less than 4.

Since most of the imperfection can be described with the second through fourth wavenumbers, these three geometric imperfection wavenumber components were determined. (Again, the $n=0$ mean value and $n=1$ rigid body components are not related to the geometric imperfections so the imperfection components begin with the $n=2$ wavenumber.) These are shown in Figs. 3a, .3b, .4a, .4b, .5a, and .5b for all three ring thicknesses. With the notable exceptions of the $n=4$ component of the 0.073 inch thick ring and the $n=2$ and $n=4$ components of the 0.102 inch thick ring, the amplitude and phase of the interior and exterior wavenumber components are nearly identical, indicating little radial variation of the geometric imperfection shape as has been assumed in the analytical analysis. The $n=4$ components of the 0.073 and 0.102 inch thick rings are small in amplitude, and thus the amplitude and phase information would be expected to be less accurate due to the inherent noise effects of the measurement system. These $n=4$

components contribute little to the imperfection shape and therefore should be neglected (i.e., considered to be zero). The discrepancy in the n=2 component of the 0.102 inch thick ring would indicate some small radial variation in this component of the geometric imperfection since it represents approximately one-fourth of the imperfection amplitude. The effects of such a variation in the radial imperfection shape have not been considered in this thesis.

A survey of the variation in ring imperfections as a function of axial position was also made. This was accomplished by making three measurements in the axial direction at the one-fourth, one-half, and three-fourths height positions. The difference between the one-fourth and three-fourths height positions with respect to the one-half position for the interior and exterior surfaces are plotted in Figs. 1.6a and b, 2.6a and b, and 3.6a and b, respectively. The axial variation was determined to be less than a maximum of 3 mils for the overall imperfection shape and decreased with increasing ring thickness. The maximum axial variation occurs where there is surface rusting and scarring, which is more of a surface variation than a geometric imperfection. Thus, the axial variation is small enough that the axial coordinate can be neglected even in terms of the geometric imperfections and the reduced dimensionality of the circular ring problem seems to be justified.

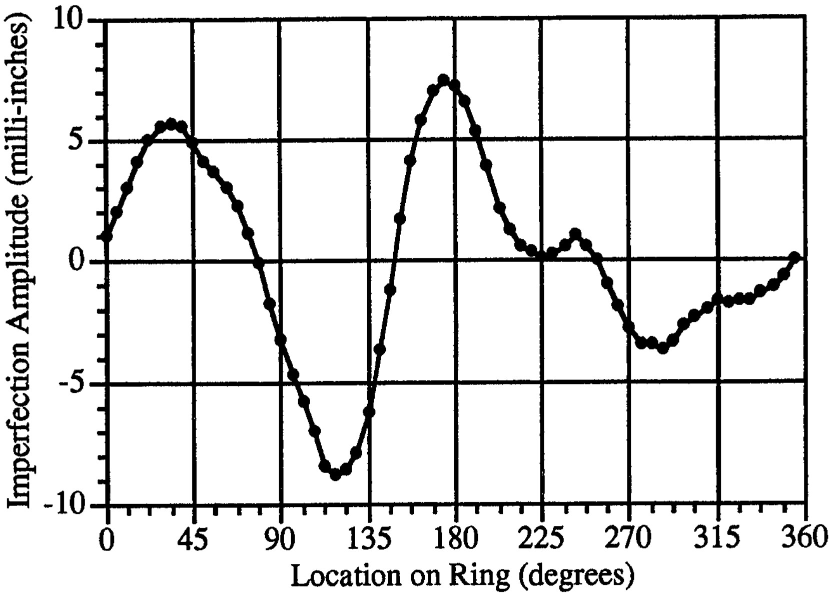

Figure E.1.1a
0.034 Inch Thick Ring Interior Imperfection Shape

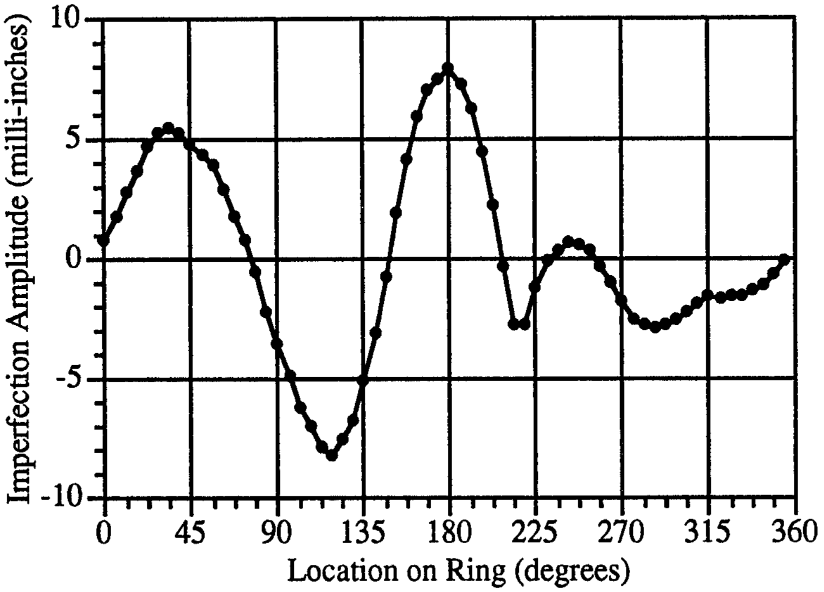

Figure E.1.1b
0.034 Inch Thick Ring Exterior Imperfection Shape

AS-94-1174

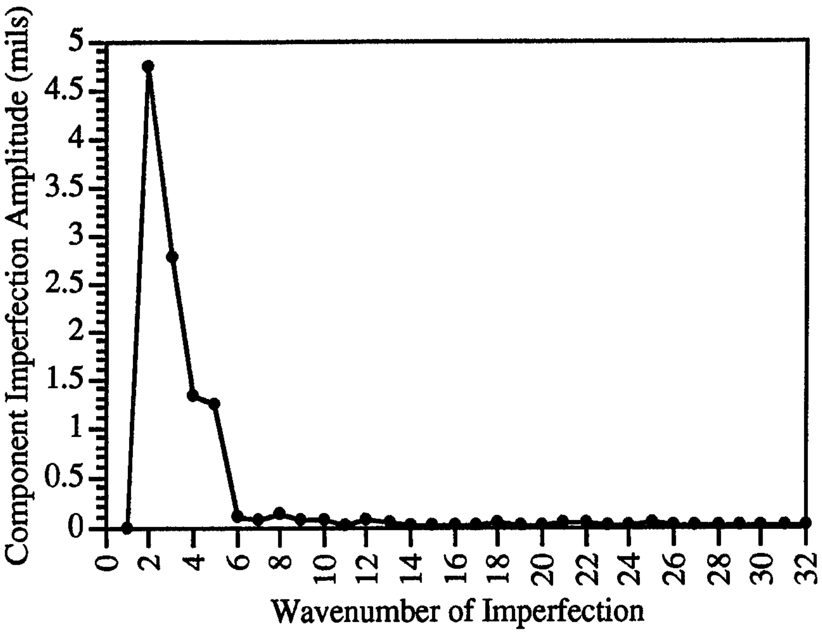

Figure E.1.2a
0.034 Inch Thick Ring Interior Imperfection Wavenumbers

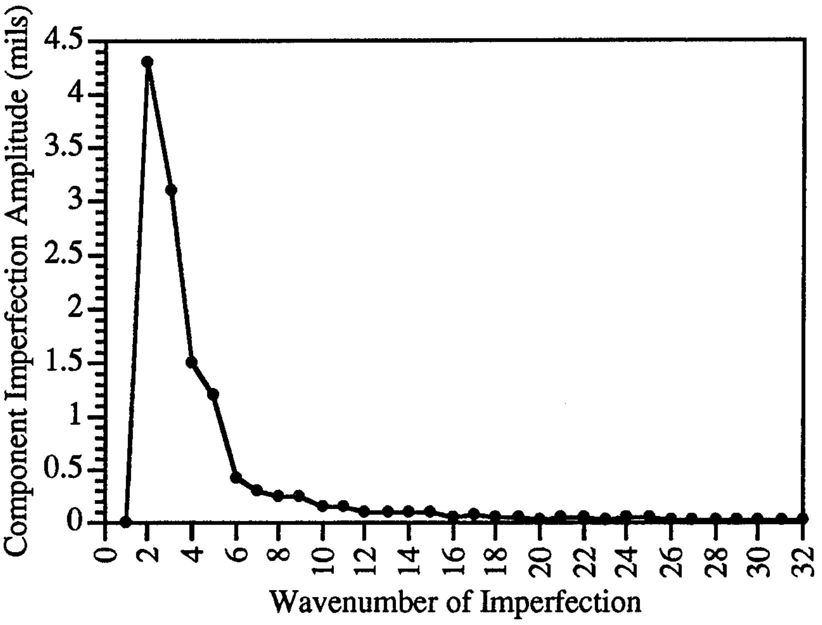

Figure E.1.2b
0.034 Inch Thick Ring Exterior Imperfection Wavenumbers

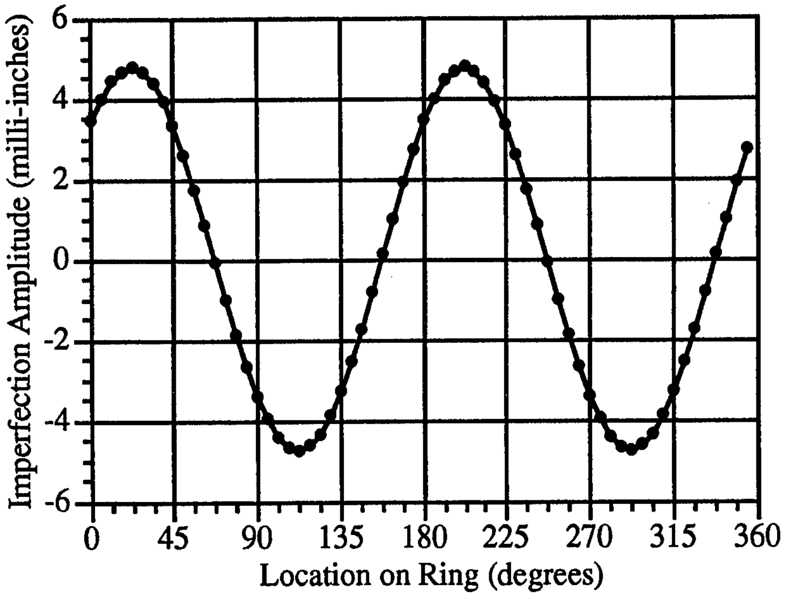

Figure E.1.3a
0.034 Inch Thick Ring Interior Wavenumber 2 Component

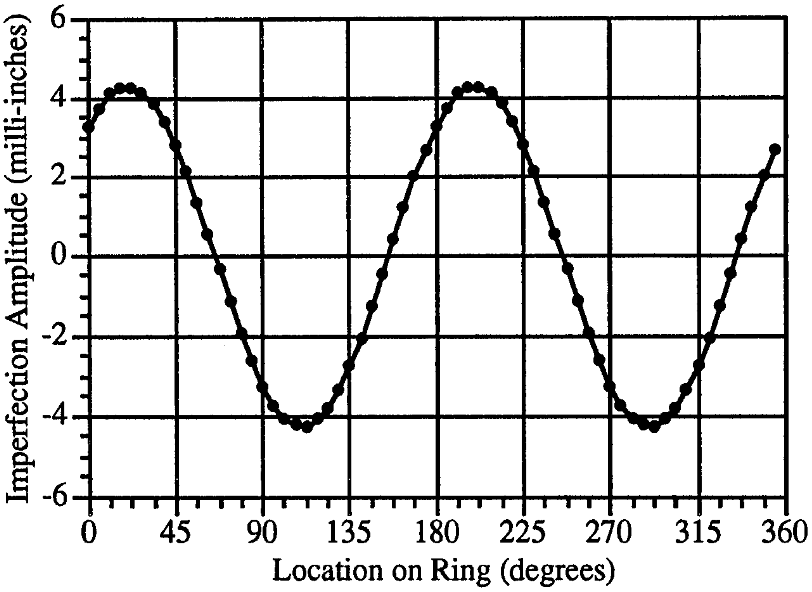

Figure E.1.3b
0.034 Inch Thick Ring Exterior Wavenumber 2 Component

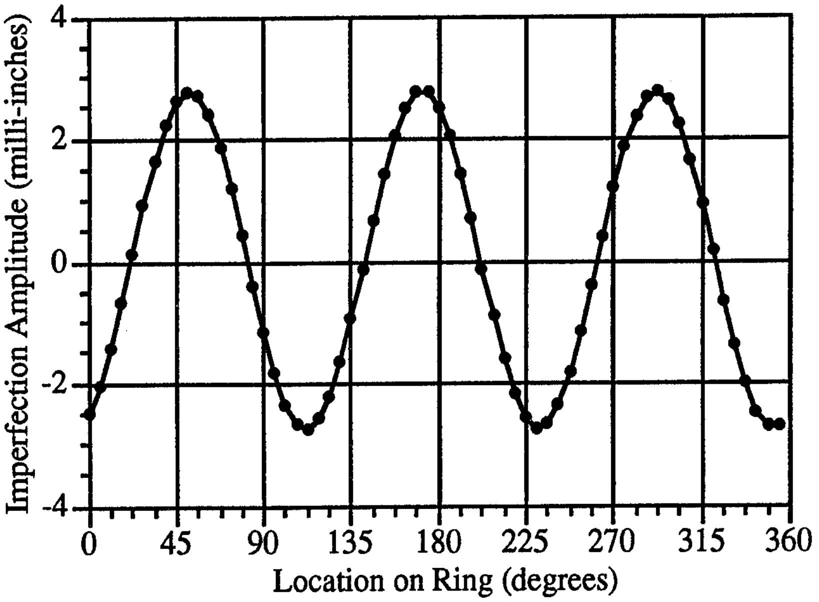

Figure E.1.4a
0.034 Inch Thick Ring Interior Wavenumber 3 Component

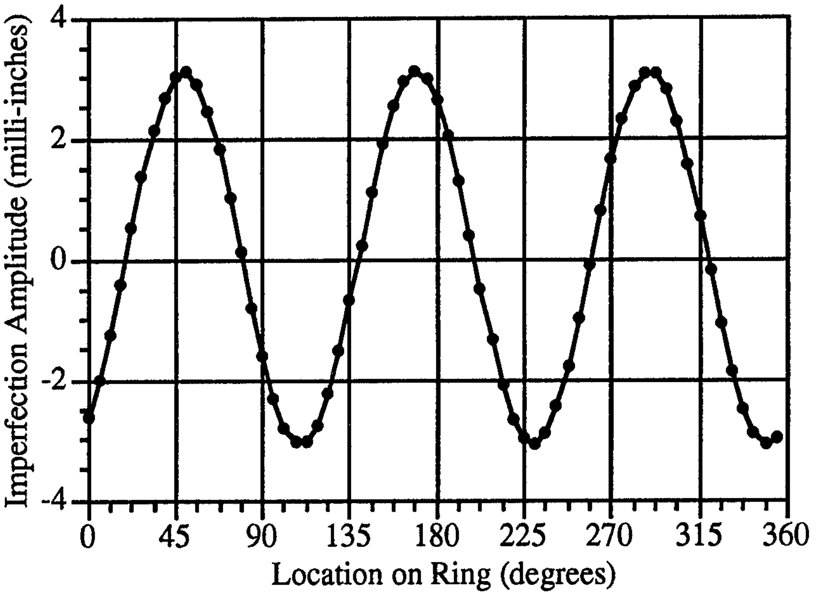

Figure E.1.4b
0.034 Inch Thick Ring Exterior Wavenumber 3 Component

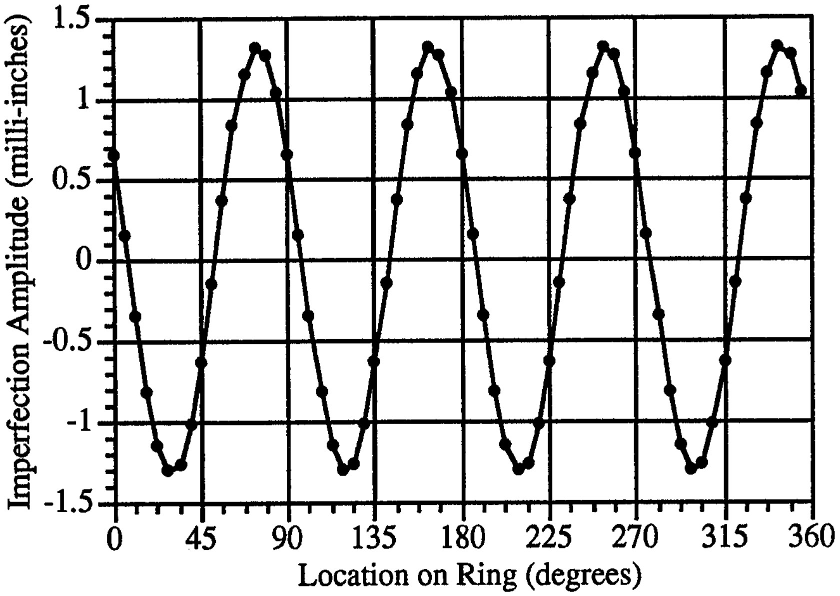

Figure E.1.5a
0.034 Inch Thick Ring Interior Wavenumber 4 Component

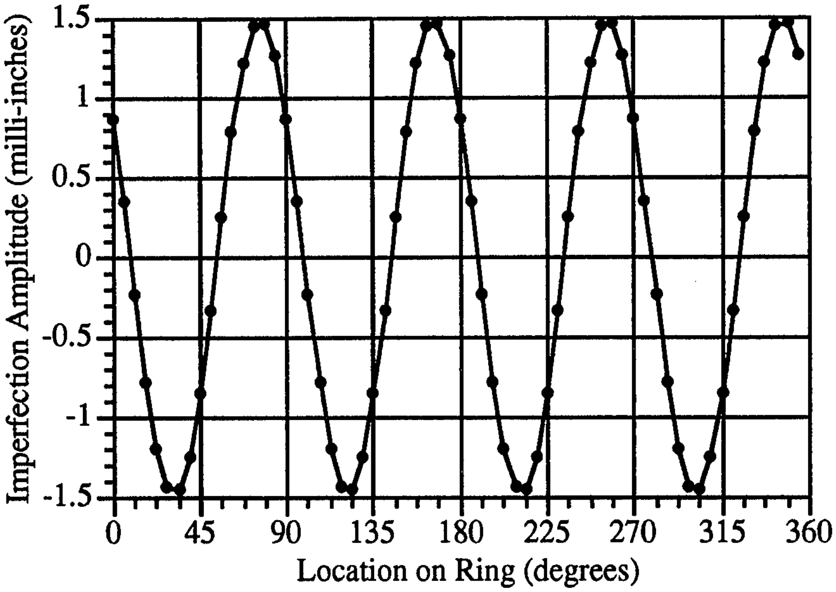

Figure E.1.5b
0.034 Inch Thick Ring Exterior Wavenumber 4 Component

AS-94-1178

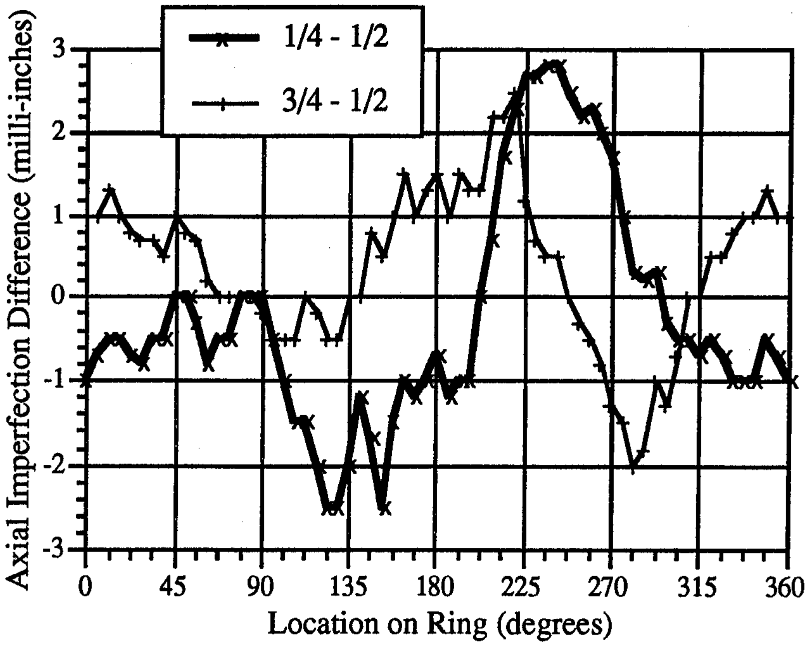

Figure E.1.6a
0.034 Inch Thick Ring Interior Axial Imperfection Variation

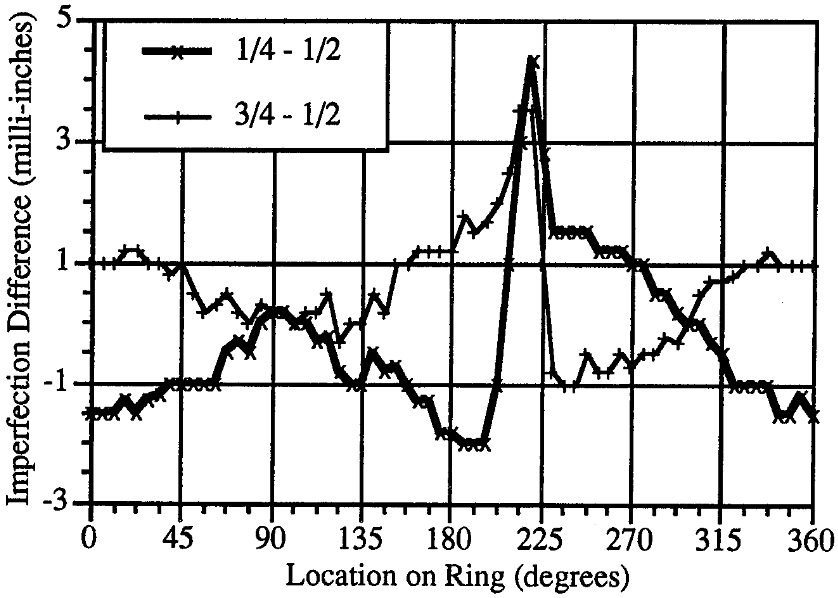

Figure E.1.6b
0.034 Inch Thick Ring Exterior Axial Imperfection Variation

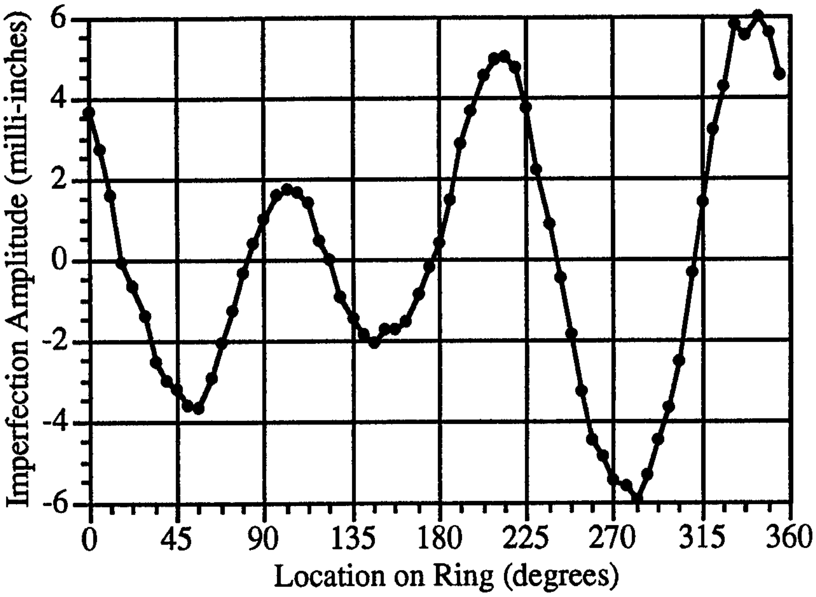

Figure E.2.1a
0.073 Inch Thick Ring Interior Imperfection Shape

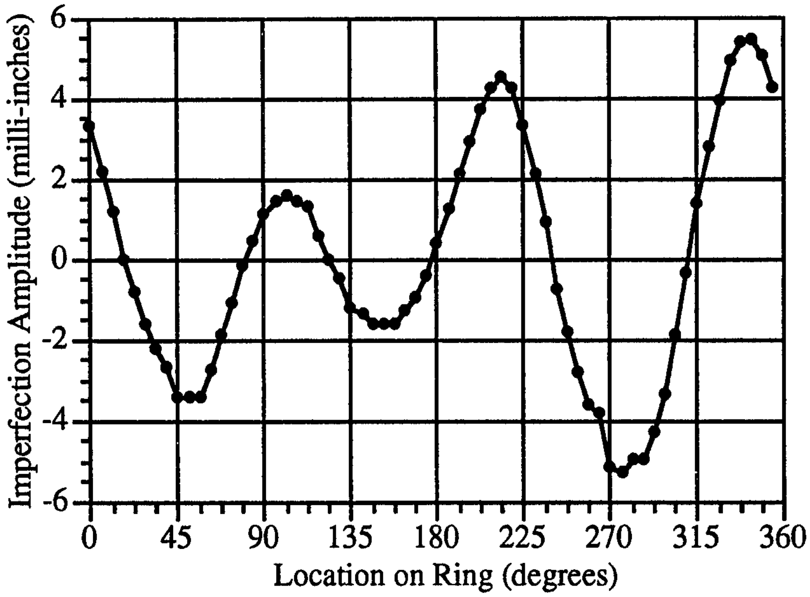

Figure E.2.1b
0.073 Inch Thick Ring Exterior Imperfection Shape

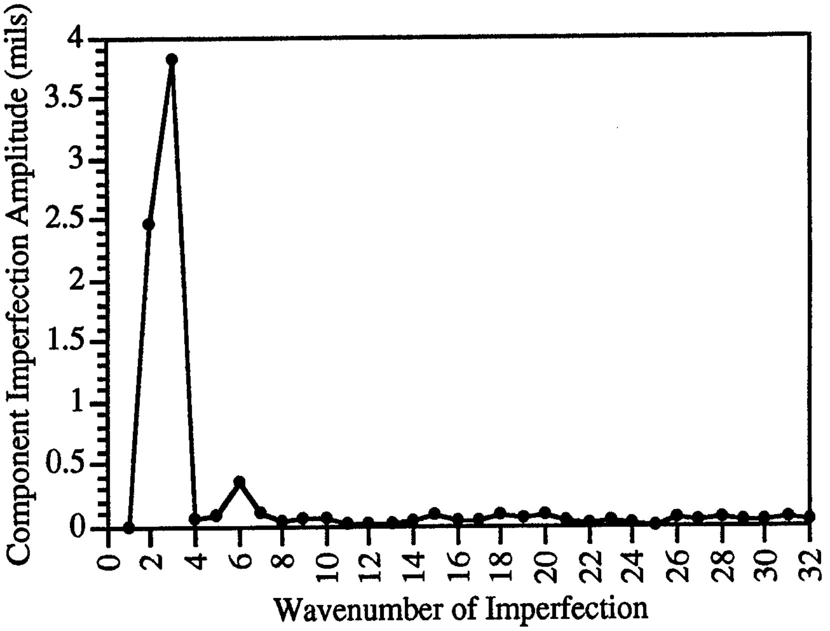

Figure E.2.2a
0.073 Inch Thick Ring Interior Imperfection Wavenumbers

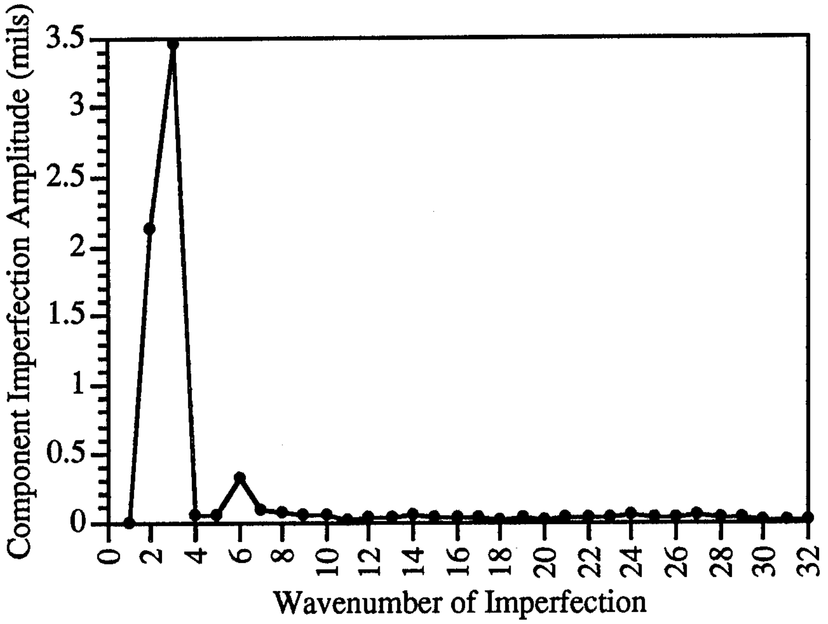

Figure E.2.2b
0.073 Inch Thick Ring Exterior Imperfection Wavenumbers

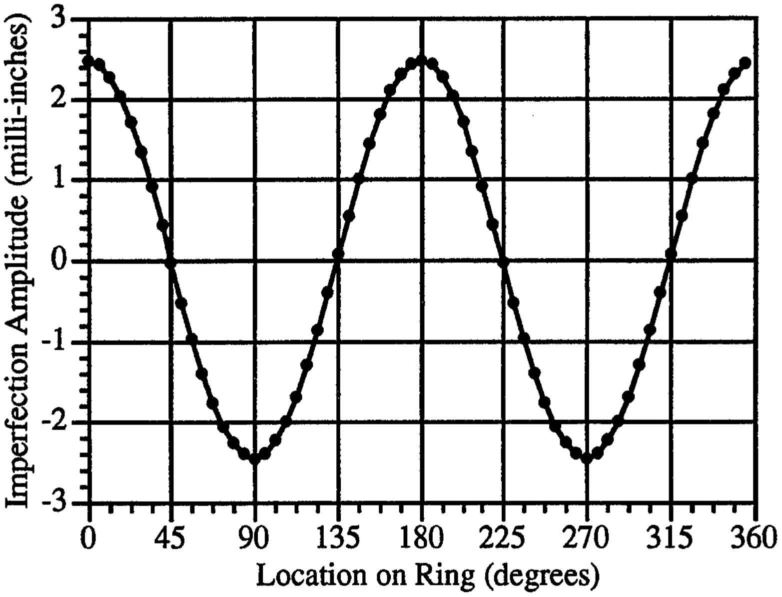

Figure E.2.3a
0.073 Inch Thick Ring Interior Wavenumber 2 Component

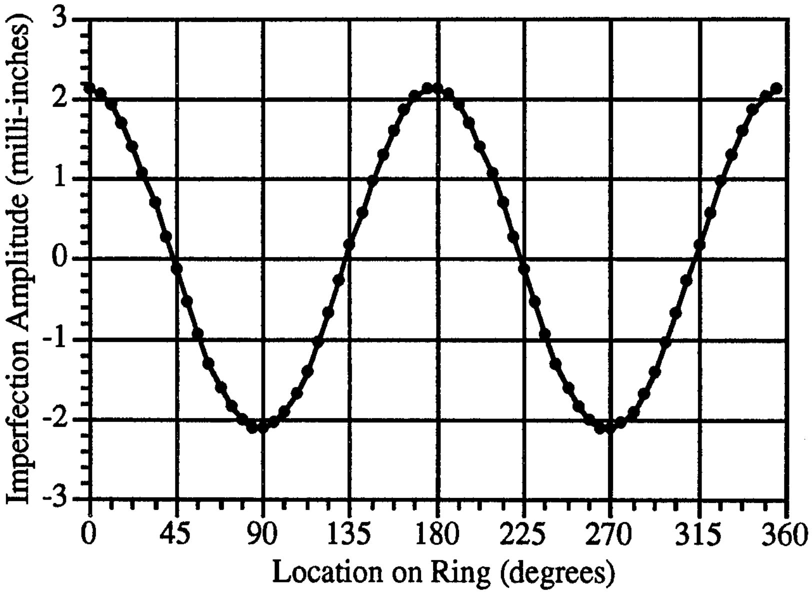

Figure E.2.3b
0.073 Inch Thick Ring Exterior Wavenumber 2 Component

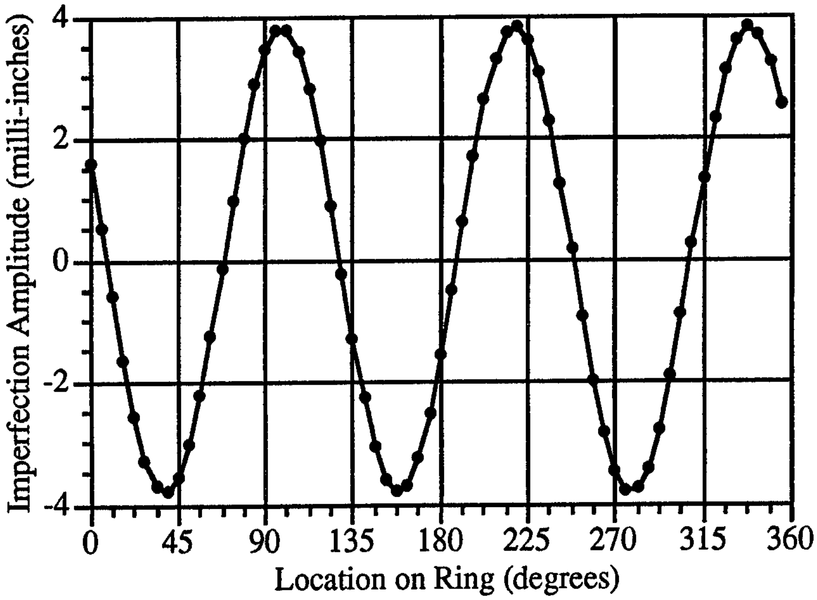

Figure E.2.4a
0.073 Inch Thick Ring Interior Wavenumber 3 Component

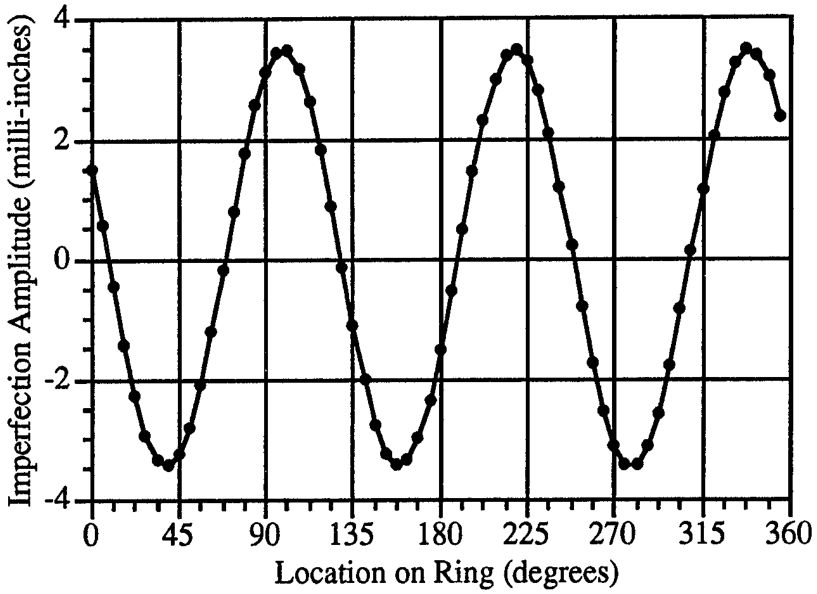

Figure E.2.4b
0.073 Inch Thick Ring Exterior Wavenumber 3 Component

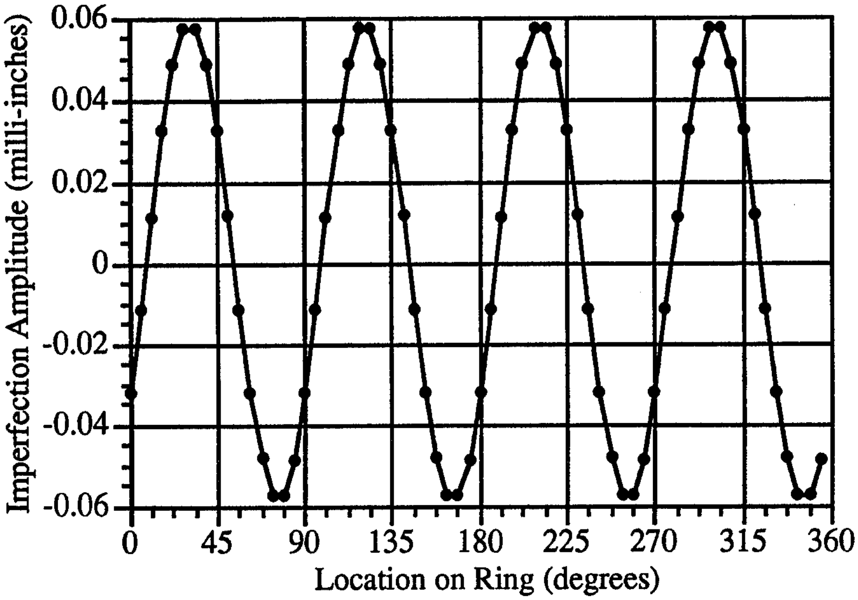

Figure E.2.5a
0.073 Inch Thick Ring Interior Wavenumber 4 Component

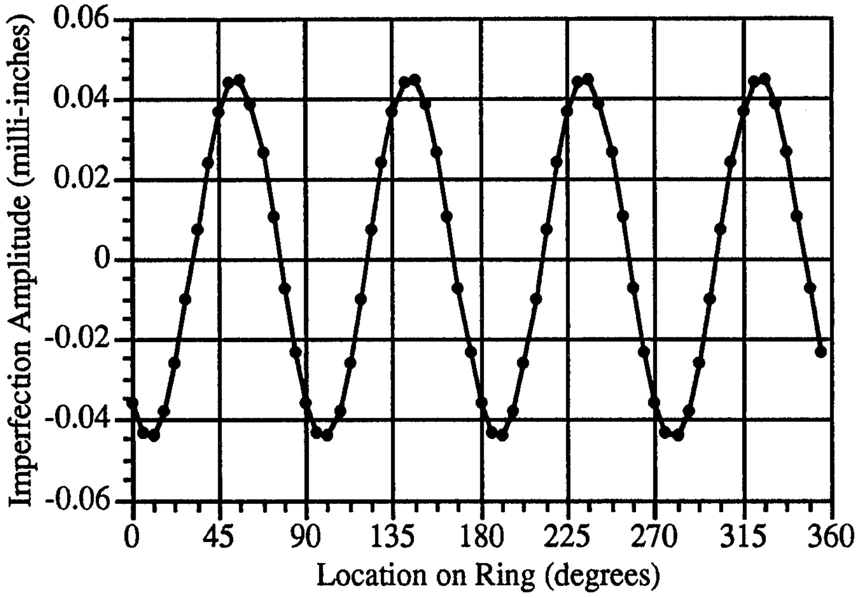

Figure E.2.5b
0.073 Inch Thick Ring Exterior Wavenumber 4 Component

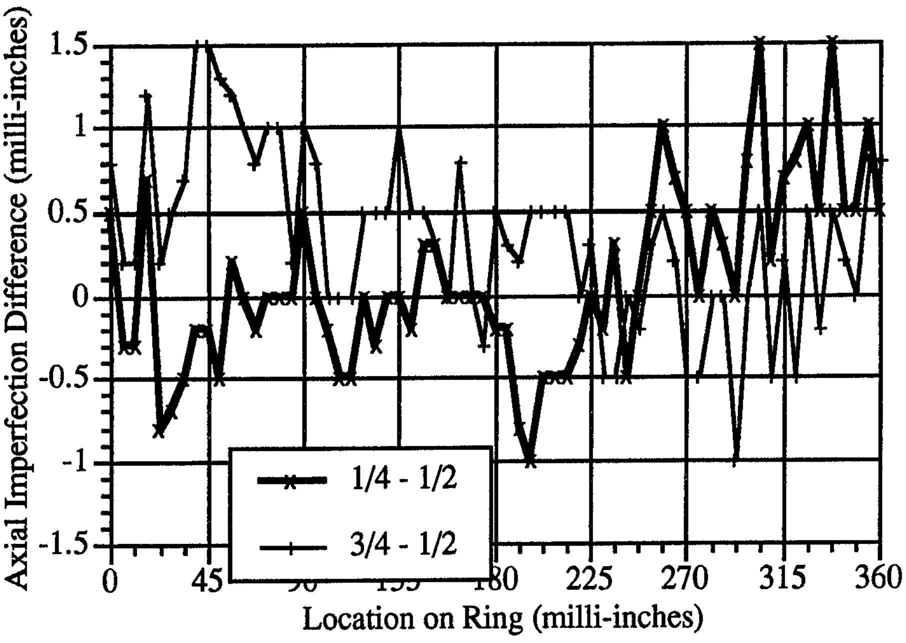

Figure E.2.6a
0.073 Inch Thick Ring Interior Axial Imperfection Variation

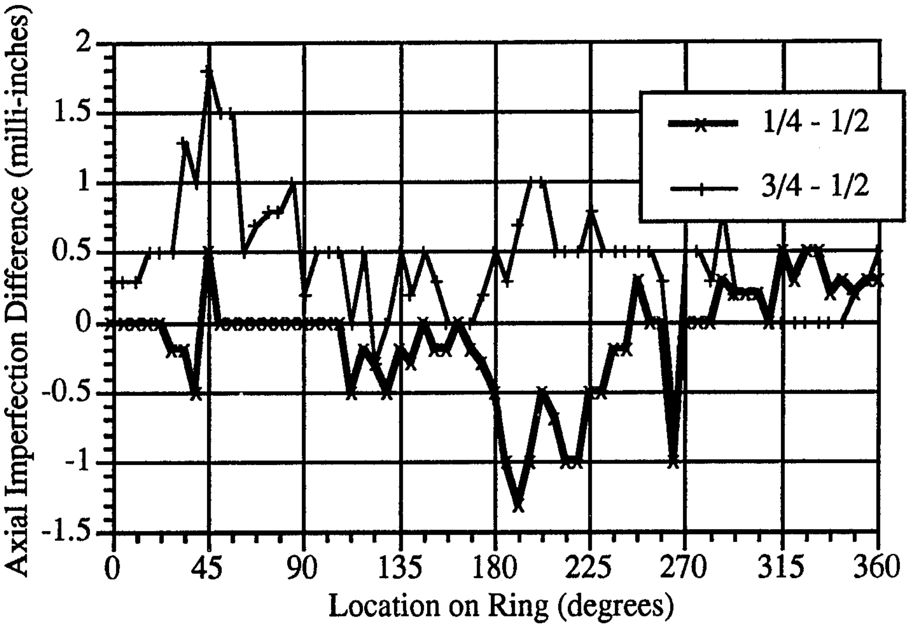

Figure E.2.6b
0.073 Inch Thick Ring Exterior Axial Imperfection Variation

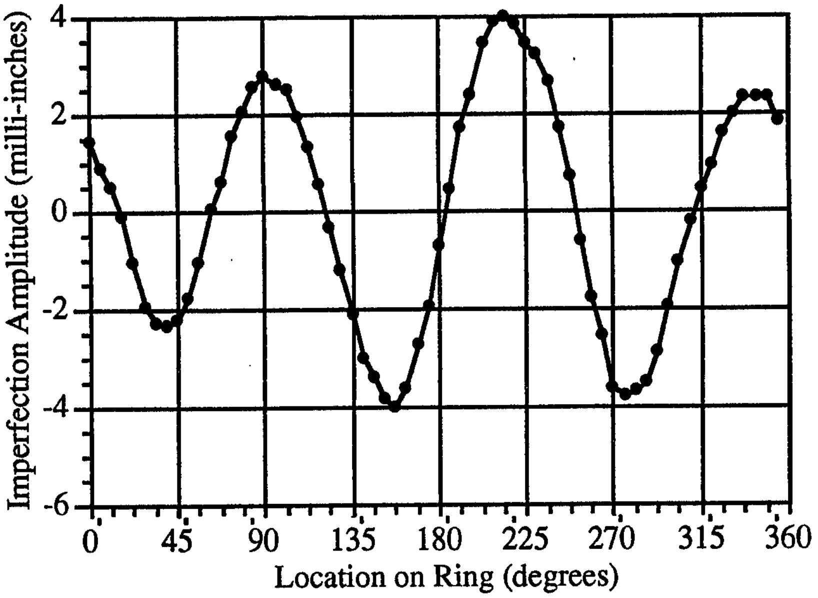

Figure E.3.1a
0.102 Inch Thick Ring Interior Imperfection Shape

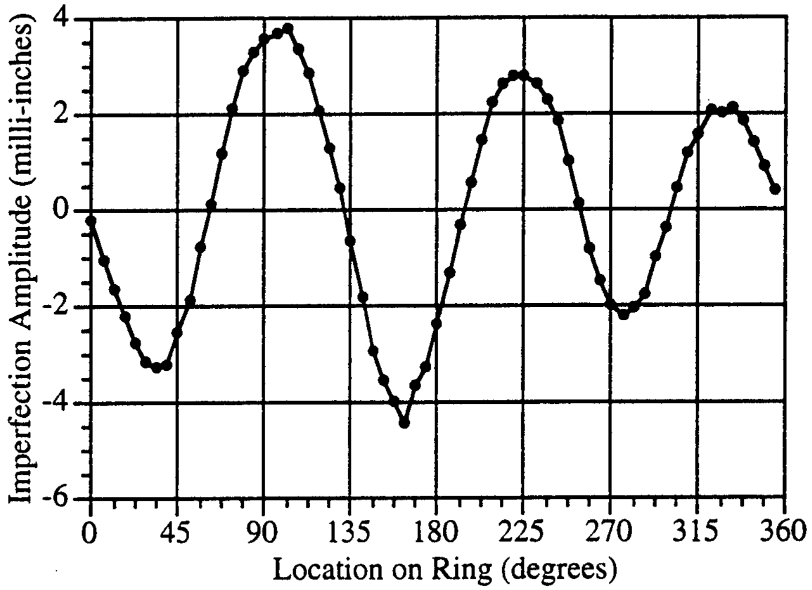

Figure E.3.1b
0.102 Inch Thick Ring Exterior Imperfection Shape

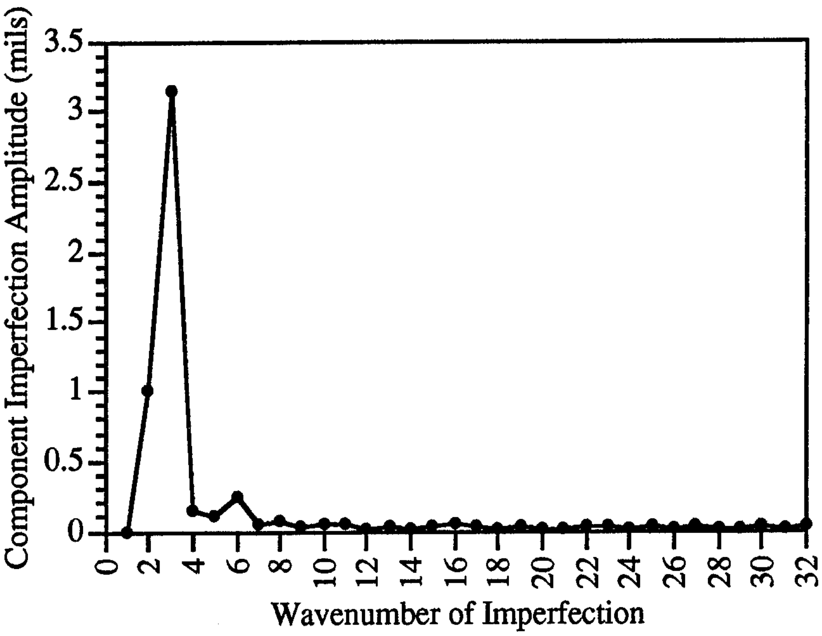

Figure E.3.2a
0.102 Inch Thick Ring Interior Imperfection Wavenumbers

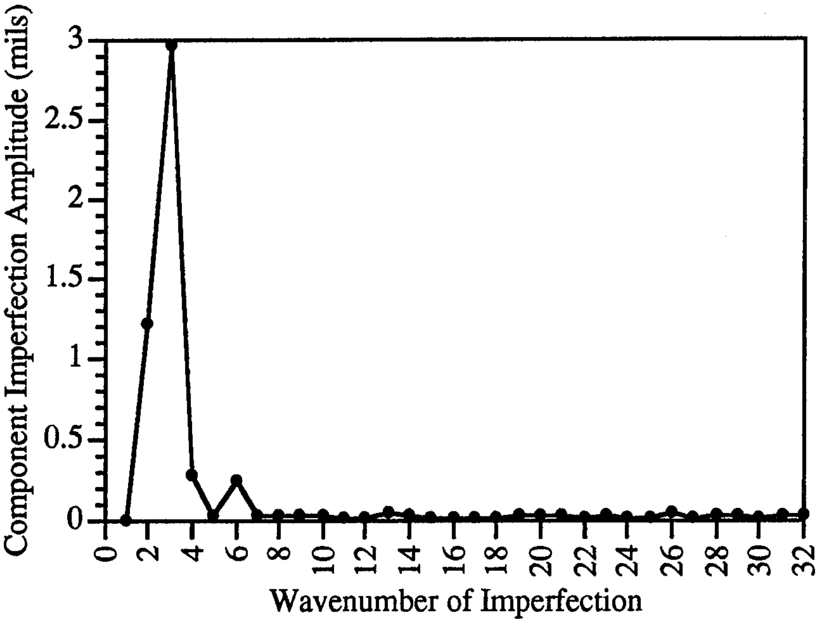

Figure E.3.2b
0.102 Inch Thick Ring Exterior Imperfection Wavenumbers

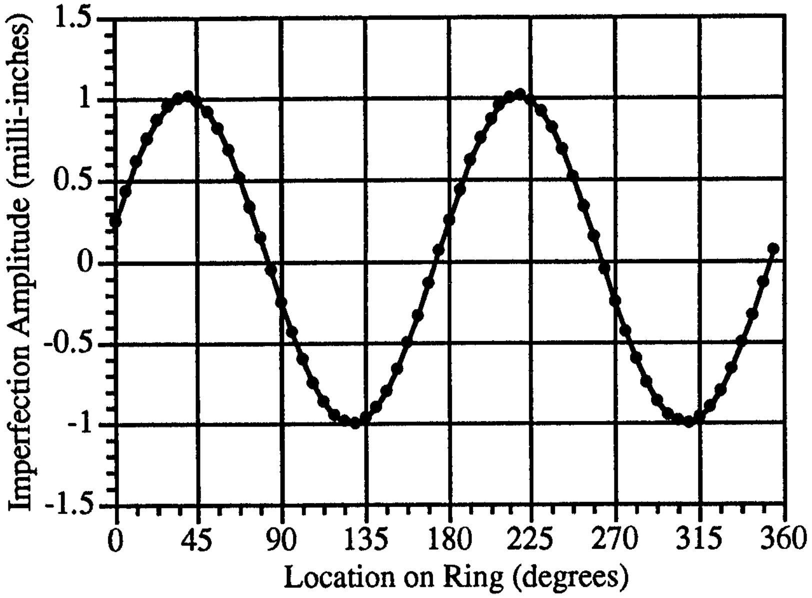

Figure E.3.3a
0.102 Inch Thick Ring Interior Wavenumber 2 Component

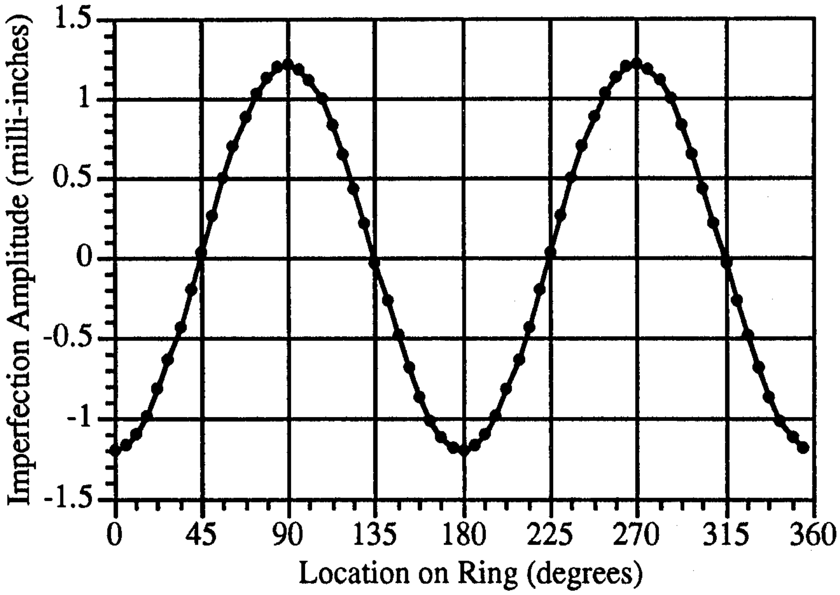

Figure E.3.3b
0.102 Inch Thick Ring Exterior Wavenumber 2 Component

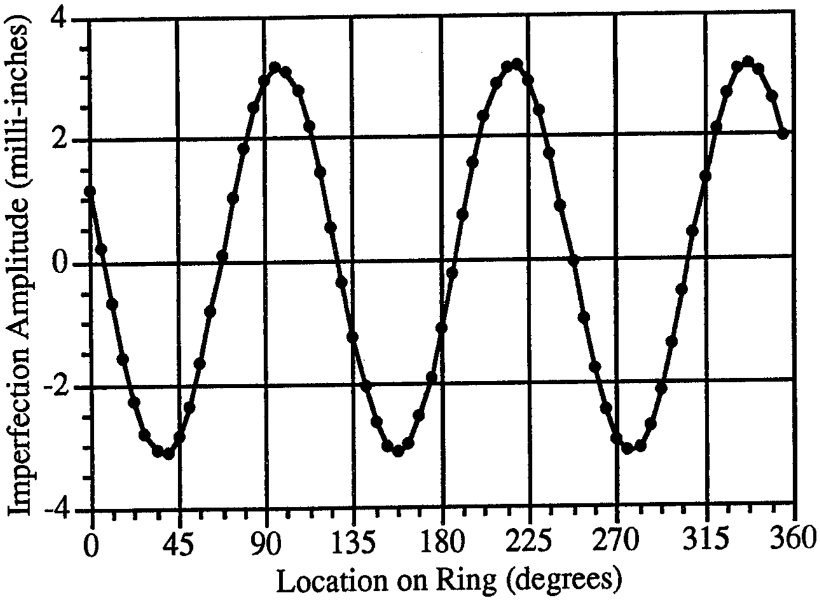

Figure E.3.4a
0.102 Inch Thick Ring Interior Wavenumber 3 Component

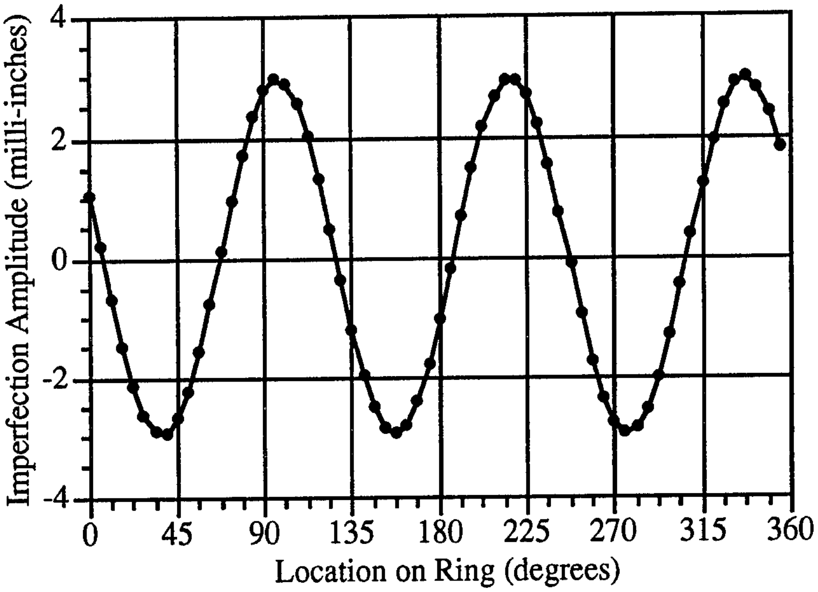

Figure E.3.4b
0.102 Inch Thick Ring Exterior Wavenumber 3 Component

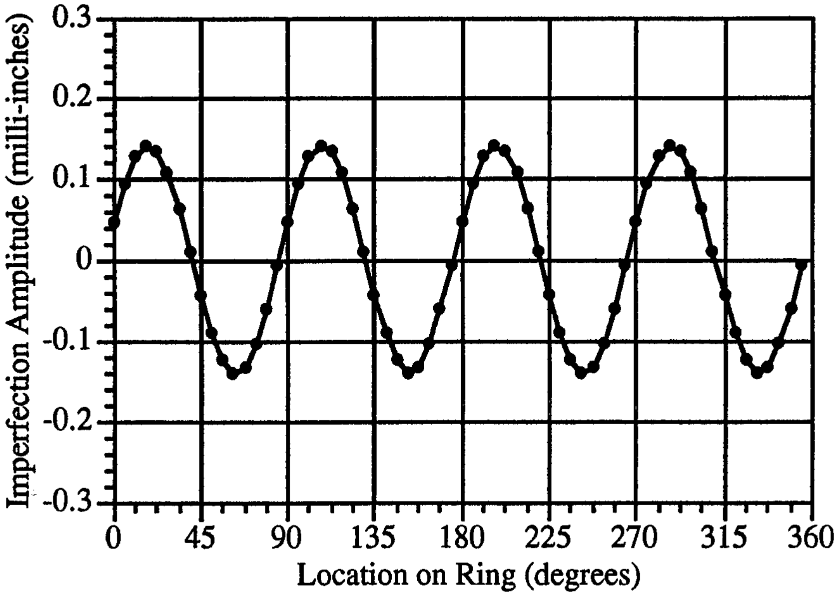

Figure E.3.5a
0.102 Inch Thick Ring Interior Wavenumber 4 Component

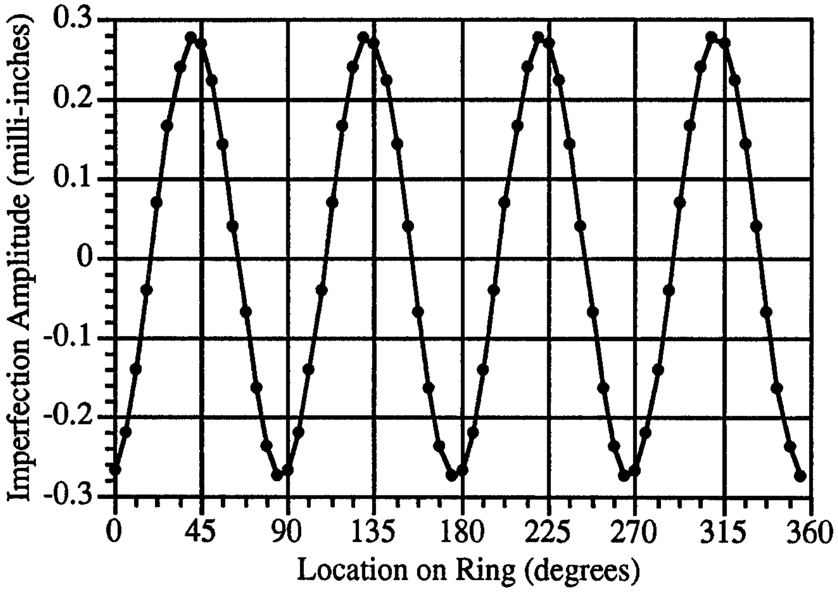

Figure E.3.5b
0.102 Inch Thick Ring Exterior Wavenumber 4 Component

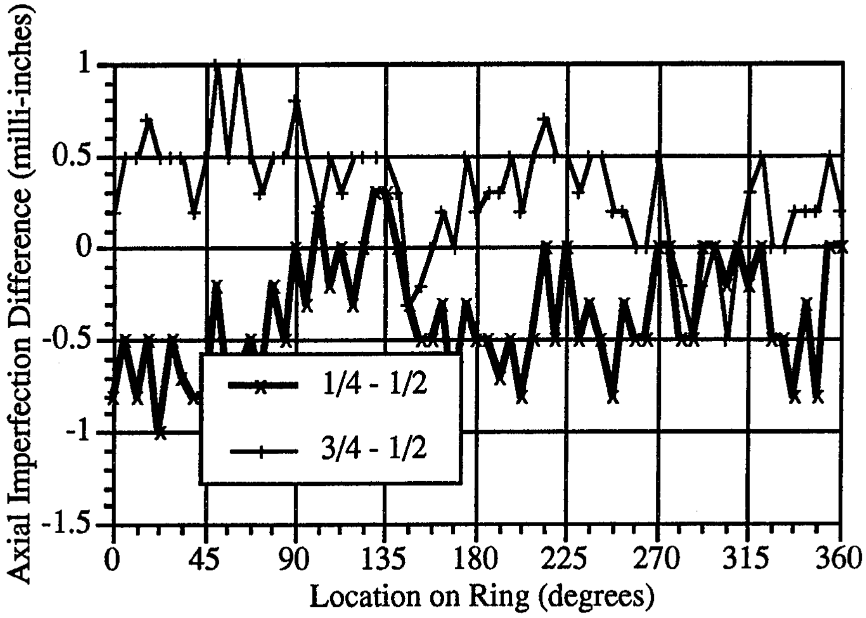

Figure E.3.6a
0.102 Inch Thick Ring Interior Axial Imperfection Variation

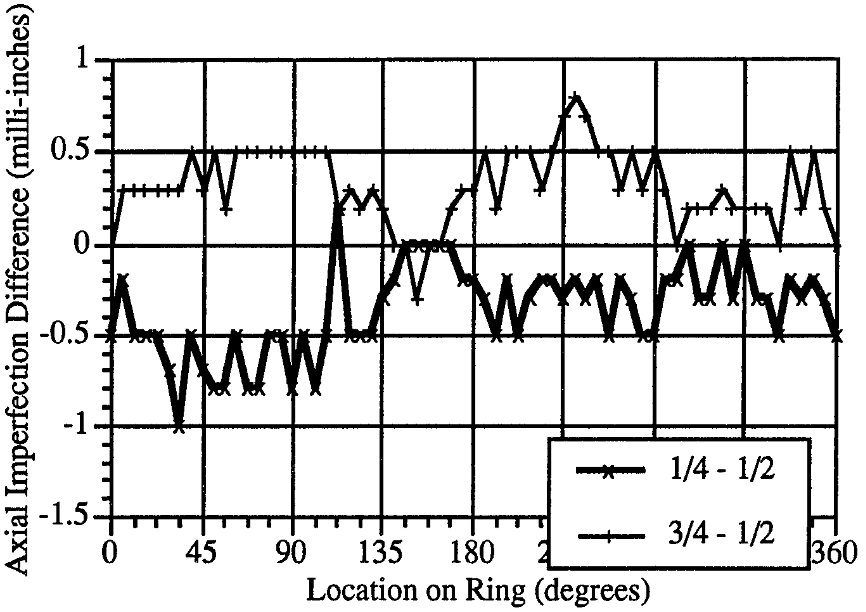

Figure E.3.6b
0.102 Inch Thick Ring Exterior Axial Imperfection Variation

ACKNOWLEDGMENTS

The acknowledgment page is given to the author to thank all who assisted in the completion of the paper. That task for me is quite impossible to fulfill, since so many have contributed to this work. However, there are a few who deserve special recognition. Especially to be mentioned are the staff and students of the Signal Physics Group at Applied Research Laboratories. Special thanks are given to Jay Lamb and Paul Till who served as consultants, confidants, and friends.

I wish to thank Stearman Aircraft Products, Inc., of Valley Center, Kansas, for providing the steel rings used for the experiment. The experimental instrumentation was graciously provided by Applied Research Laboratories, The University of Texas at Austin; and the Aeroelasticity Laboratory of the Department of Aerospace Engineering and Engineering Mechanics, The University of Texas at Austin.

Dr. Ronald Stearman and Dr. Gary Wilson deserve more than just the customary thanks for serving as advisors and readers on this thesis. Their patience in seeing this project through to the end should be commended. Dr. Stearman has shown himself to be not only a capable advisor but one of the truly outstanding individuals in his general concern and grace in dealing with all who come in contact with him. Dr. Wilson was especially supportive in assisting with the data acquisition system needed.

The research for this study was supported under an Independent Research and Development Program sponsored by Applied Research Laboratories, The University of Texas at Austin.

This page intentionally left blank.

REFERENCES

1. Cremer, L. , et al., *Structure-Borne Sound*, Springer-Verlag, New York, 1973.

2. Evensen, D.A., "Nonlinear Flexural Vibrations of Thin Circular Rings," Doctoral Dissertation, California Institute of Technology, 1964.

3. O'Donnell, R.B., "Bispectral Investigation of Active Control Processes," Master's Thesis, The University of Texas at Austin, May, 1990.

4. Evensen, D.A., "Nonlinear Vibrations of Circular Cylindrical Shells," from *Thin-Shell Structures: Theory Experiment, and Design*, Y.C. Fung and E.E. Sechler, ed., Prentice-Hall, Inc., Englewood Cliffs, N.J., 1974, pp. 133-155.

5. Reissner, E., "Non-linear Effects in the Vibrations of Cylindrical Shells," Report No. AM5-6, Ramo-Wooldridge Corp., 1955.

6. Chu, H., "Influence of Large Amplitudes on Flexural Vibrations of a Thin Circular Cylindrical Shell," *Journal of Aerospace Science*, vol. 28. no. 8, Aug. 1961, pp. 602-609.

7. Liu, D.K., and J. Arbocz, "Stability Analysis of Nonlinear Vibrations of Imperfect Thin Walled Cylinders," Report LR-461, Dept. of Aerospace Engineering, TH-Delft, The Netherlands, 1986.

8. Liu, D.K., and J. Arbocz, "Damped Nonlinear Vibrations of Imperfect Thin-Walled Cylindrical Shells," Report LR-462, Dept. of Aerospace Engineering, TH-Delft, The Netherlands, 1985.

9. Liu, D.K., and J. Arbocz, "Influence of Initial Geometric Imperfections on Nonlinear Vibrations of Thin Circular Cylindrical Shells," Report LR-467, Dept. of Aerospace Engineering, TH-Delft, The Netherlands, Feb. 1985.

10. Liu, D.K., and J. Arbocz, "Influence of Initial Geometric Imperfections on Undamped Vibrations of Thin Circular Cylindrical Shells," Report LR-457, Dept. of Aerospace Engineering, TH-Delft, The Netherlands, Oct. 1986.

11. Rayleigh, Lord, *The Theory of Sound*, Vol. 1, Dover Pub., New York, 1945, pp. 304-305.

12. Buckens, F., "Influence of the Relative Radial Thickness of a Ring on its Natural Frequencies," *Journal of the Acoustical Society of America*, vol. 22, no. 4, July 1950, pp. 437-443.

13. Kaiser, E.R., "Acoustical Vibrations of Rings," *Journal of the Acoustical Society of America*, vol. 25, no. 4, July 1953, pp. 617-623.

14. Charnley, T., and R. Perrin, "Perturbation Studies with a Thin Circular Ring," *Acustica*, vol. 28, 1973, pp. 139-146.

15. Charnley, T., et al., "Vibrations of Thin Rings of Rectangular Cross-Section," *Journal of Sound and Vibration*, vol. 134, no. 3, 1989, pp. 455-488.

16. Hawkings, D.L., "A Generalized Analysis of the Vibration of Circular Rings," *Journal of Sound and Vibration*, vol. 54, no. 1, 1977, pp. 67-74.

17. Irvine, H.M., "On the Natural Frequencies of Vibration of a Ring Surrounded by and/or Containing a Fluid," *Thin-Walled Structures*, vol. 9, 1990, pp. 151-162.

18. Wasserman, E.B., "The Effect of the Behavior of the Load on the Frequency of the Free Vibrations of a Ring," technical translation F-52, National Aeronautics and Space Administration (originally published in Russian, 1956).

19. Charnley, T., and R. Perrin, "Characteristic Frequencies of a Symmetrically Loaded Ring," *Acustica*, vol. 25, 1971, pp. 240-246.

20. Evensen, D.A., "A Theoretical and Experimental Study of the Nonlinear Flexural Vibrations of Thin Circular Rings," TR R-227, National Aeronautics and Space Administration - Langley, 1965.

21. Evensen, D.A., "Nonlinear Flexural Vibrations of Thin Circular Rings," *Journal of Applied Mechanics*, Sept. 1966, pp. 553-560.

22. Kovrigin, D.A., and A.I. Potapov, "Nonlinear Vibrations of a Thin Ring," *Soviet Applied Mechanics*, vol. 25, no. 3, Sept. 1989, pp. 76-81.

23. Maganty, S.P., and W.B. Bickford, "Large Amplitude Oscillations of Thin Circular Rings," *Journal of Applied Mechanics*, vol. 54 June 1987, pp. 315-322.

24. Mack, L.R., and C. Yew, "Nonlinear Periodic Flexural Oscillations of a Thin Elastic Ring," EMRL 1052, Engineering Mechanics Research Laboratory, The University of Texas at Austin, Jan. 1968.

25. Goodier, J.N., and I.K. McIvor, "The Elastic Cylindrical Shell Under Nearly Uniform Radial Impulse," *Journal of Applied Mechanics*, June 1964, pp. 259-266.

26. Nikias, C.L., and M.R. Raghuveer, "Bispectrum Estimation: A Digital Signal Processing Framework," *Proceedings of the IEEE*, vol. 75, no. 7, July 1987, pp. 869-891.

27. Pezeshki, C., et al., "Bispectral Analysis of Possessing Chaotic Motion," *Journal of Sound and Vibration*, vol. 137, no. 3, 1990, pp. 357-368.

28. Sasaki, O., et al., "Laser Doppler Vibration Measuring System Using Bispectral Analysis," *Applied Optics*, vol. 19, no. 1, Jan. 1980, pp. 151-153.

29. Choi, D., et al., "Bispectral Identification of Nonlinear Mode Interactions," *Proceedings of the 2nd International Modal Analysis Conference*, Feb. 1984, pp. 602-609.

30. Stearman, R.O., et al., "Identification of Aeroelastic Phenomenon Employing Bispectral Analysis Techniques," *Proceedings of the 3rd International Modal Analysis Conference*, Jan. 1985, pp. 956-964.

31. Stearman, R.O., et al., "Aeroelastic System Identification of Advanced Technology Aircraft through Higher Order Signal Processing," *Proceedings of the International Signal Processing Workshop on Higher Order Statistics*, La Bérangére-Chamrousse, France, July 1991.

32. Kim, T., et al., "Non-Classical Flow-Induced Responses of a Lifting Surface Due to Localized Disturbances," *Proceedings of the 6th International Modal Analysis Conference*, Feb. 1988.

33. Perrochaud, J.B., "Bispectral Analysis of Nonlinear Systems," Master's Thesis, Institute of Sound and Vibration Research, University of Southampton, 1982.

34. Barker, R.W., "Incipient Fault Detection Using Higher-Order Statistics," Doctoral Dissertation, The University of Texas at Austin, Aug. 1991.

35. Wolinsky, M.A., "Invitation to the Bispectrum," ARL-TR-88-7, Applied Research Laboratories: The University of Texas at Austin, Feb. 1988.

36. Wilson, G.R., "Detection and Time Delay Estimation of Non-Gaussian Signals in Noise," ARL-TR-90-25, Applied Research Laboratories: The University of Texas at Austin, July 1990.

37. Hinich, M., and M. Wolinsky, "A Test for Aliasing Using Bispectral Analysis," *Journal of the American Statistical Association*, vol. 83, no. 402, June 1988, pp. 499-502.

38. Elgar, S., and R.T. Guza, "Statistics of Bicoherence," *IEEE Transactions on Acoustics, Speech, and Signal Processing*, vol. 36, no. 10, Oct. 1988, pp. 1667-1668.

39. Leissa, A., *Vibrations of Shells*, NASA SP-288, Washington, DC, 1973.

40. Novozhilov, V. V., *Foundations of the Nonlinear Theory of Elasticity*, Graylock Press, Rochester, N.Y., 1953.

41. Markus, S., *The Mechanics of Vibrations of Cylindrical Shells*, Elsevier, Amsterdam, 1988.

42. Morley, L.S.D., "An Improvement on Donnell's Approximation for Thin-Walled Circular Cylinders," *Quarterly Journal of Mechanics and Applied Mathematics*, vol. 12, no. 1, 1959, pp. 89-99.

43. Craig, R.R., *Structural Dynamics: An Introduction to Computer Methods*, John Wiley and Sons, New York, 1981.

44. Fung, Y.C., *Foundations of Solid Mechanics*, Prentice-Hall, Inc., Englewood Cliffs, N. J., 1965.

45. Philipson, L.L., "On the Role of Extension in the Flexural Vibrations of Rings," *Journal of Applied Mechanics*, vol. 23, no. 3, Sept. 1956, pp. 364-366.

46. Singer, J., "On the Equivalence of the Galerkin and Rayleigh-Ritz Methods," *Journal of the Royal Aeronautical Society*, vol. 66, Sept. 1962, p. 592.

47. Tomlinson, G.R., "Force Distortion in Resonance Testing of Structures with Electrodynamic Vibration Exciters," *Journal of Sound and Vibration*, vol. 63, no. 3, 1979, pp. 337-350.

This page intentionally left blank.

19 December 1994

DISTRIBUTION LIST
ARL-TR-94-23
Technical Report under ARL:UT Independent Research and Development Program and Grant N00014-90-J-1366

Copy No.

Commanding Officer
Naval Research Laboratory
Washington, DC 20375-5000
1 Attn: Library

Commanding Officer
Naval Research Laboratory
Stennis Space Center, MS 39529-5004
2 Attn: Library

Commanding Officer
Naval Oceanographic Office
Stennis Space Center, MS 39522-5001
3 Attn: Library

Commander
Space and Naval Warfare Systems Command
2451 Crystal Drive
Arlington, VA 22245-5200
4 Attn: Library

Commanding Officer
Naval Command Control and Ocean Surveillance Center
RDT&E Division
San Diego, CA 92152-5000
5 Attn: Library

Commander
Dahlgren Division
Naval Surface Warfare Center
Dahlgren, VA 22448
6 Attn: Library

Commanding Officer
Coastal Systems Station, Dahlgren Division
Naval Surface Warfare Center
Panama City, FL 32407-5000
7 Attn: Library

Commander
Carderock Division
Naval Surface Warfare Center
Bethesda, MD 20084-5000
8 Attn: Library

Distribution List for ARL-TR-94-23 under ARL:UT IR&D Program
and Grant N00014-90-J-1366
(cont'd)

<u>Copy No.</u>

Officer in Charge
Naval Undersea Warfare Center
New London Detachment
New London, CT 06320-5594
9 Attn: Library

Advanced Research Projects Agency
3701 N. Fairfax Dr.
Arlington, VA 22203-1714
10 Attn: Dr. Theo Kooij
11 Library

Defense Mapping Agency
Hydrographic/Topographic Center
Washington, DC 20315-0030
12 Attn: Library

National Academy of Sciences
National Research Council
2101 Constitution Avenue
Washington, DC 20418
13 Attn: Library

National Aeronautics and Space Administration
Langley Research Center
Hampton, VA 23665
14 Attn: Library

Applied Physics Laboratory
The Johns Hopkins University
Johns Hopkins Road
Laurel, MD 20810
15 Attn: Library

Applied Physics Laboratory
The University of Washington
1013 Northeast 40th Street
Seattle, WA 98105
16 Attn: Library

Applied Research Laboratory
The Pennsylvania State University
P.O. Box 30
State College, PA 16801
17 Attn: Library

Distribution List for ARL-TR-94-23 under ARL:UT IR&D Program and Grant N00014-90-J-1366
(cont'd)

<u>Copy No.</u>

Scripps Institution of Oceanography (G&E)
The University of California, San Diego
La Jolla, CA 92093-0175
18 Attn: Library

Woods Hole Oceanographic Institution
86-95 Water Street
Woods Hole, MA 02543
19 Attn: Library

Office of the Chief of Naval Research
Department of the Navy
800 North Quincy Street
Arlington, VA 22217-5000
20 Attn: Kam Ng, Code 334
21 Douglas Lake, Code 313
22 Geoff Main, Code 334

23 DTIC-OCC
Defense Technical Information Center
8725 John J. Kingman Road, Suite 0944
Fort Belvoir, VA 22060-6218

University of Texas at Austin
Electrical and Computer Engineering Department
Austin, TX 78713
24 Attn: Prof. Ed Powers

25 Douglas J. Fox
6831 Forest Meadow
San Antonio, TX 78238

26 Jay L. Lamb
Aeronautics Dept., BBE
The Johns Hopkins University
Applied Physics Laboratory
Laurel, MD 20723-6099

27 Paul Till
777 North Silver Springs
Apt. 1816
Wichita, KS 67212

28 Martin L. Barlett, ARL:UT

Distribution List for ARL-TR-94-23 under ARL:UT IR&D Program and Grant N00014-90-J-1366
(cont'd)

Copy No.	
29	Melvin J. Hinich, ARL:UT
30	Ronald O. Stearman, ARL:UT
31	R. Joe Thornhill, ARL:UT
32	Gary R. Wilson, ARL:UT
33	Signal Physics Group, ARL:UT
34	Library, ARL:UT
35 - 45	Reserve